IONOSPHERIC PLASMA ELECTRON DENSITY MEASUREMENT AND THEORY USING IMPEDANCE PROBE TECHNIQUES

by

Justin Wellington

A thesis submitted in partial fulfillment
of the requirements for the degree

of

MASTER OF SCIENCE

in

Electrical Engineering

Approved:

Charles Swenson, Ph.D. Major Professor	Bedri Cetiner, Ph.D. Committee Member
Burak Sarsılmaz, Ph.D. Committee Member	David F. Feldon, Ph.D. Vice Provost of Graduate Studies

UTAH STATE UNIVERSITY
Logan, Utah

2026

ABSTRACT

IONOSPHERIC PLASMA ELECTRON DENSITY MEASUREMENT AND THEORY USING IMPEDANCE PROBE TECHNIQUES

by

Justin Wellington, Master of Science

Utah State University, 2026

Major Professor: Charles Swenson, Ph.D.
Department: Electrical and Computer Engineering

Impedance probes provide in-situ electron density measurements at small spatial and temporal scales in the ionosphere. These measurements are important for understanding and predicting plasma irregularities that lead to GPS and radio frequency (RF) communication disruptions, particularly during the formation of Equatorial Plasma Bubbles (EPB). Existing analytical models for impedance probes are typically limited to simple geometries.

This thesis develops a numerical method for computing the impedance of a probe immersed in a cold-magnetized plasma by combining finite-element electric field solutions from ANSYS Maxwell with a numerical integration in MATLAB. A tensor rotation is used to account for arbitrary magnetic-field orientation, and the method is validated by comparing the numerical impedance results to analytical solutions for plates, cylinders, and spheres.

Sheath effects are incorporated into analytical models by introducing a finite vacuum boundary around the probe and determining the equivalent series capacitance. The resulting impedance is written in a rational form that clearly shows the locations of the series and parallel resonances. Shifts in these resonances due to the magnetic field and sheath thickness are derived and compared directly to Scintillation Prediction Observation Research Task (SPORT) spacecraft impedance probe measurements.

A new impedance probe circuit based on an auto-balancing bridge topology is also designed and tested. The circuit aims to improve the measurement range of the probe. Guarding techniques are analyzed and compared. Calibration results verify that the re-designed system can reliably measure impedances over the 1–30 MHz range.

Overall, this work provides a general method for numerically computing the probe impedance for arbitrary geometries, a detailed analysis of sheath-induced resonance behavior, and an improved circuit architecture suitable for next-generation ionospheric impedance probes.

(121 pages)

PUBLIC ABSTRACT

IONOSPHERIC PLASMA ELECTRON DENSITY MEASUREMENT AND THEORY USING IMPEDANCE PROBE TECHNIQUES

Justin Wellington

The ionosphere plays a critical role in how radio frequency (RF) signals, like those used in Global Position System (GPS) satellite communications, travel through space. Disturbances in the ionosphere, such as equatorial plasma bubbles (EPB), scatter these signals and cause communication dropouts or navigational errors. To study these conditions, spacecraft use instruments that measure the surrounding plasma directly. One of these instruments is an impedance probe, which applies a small electrical signal to a sensor and determines electron density from the measured impedance.

This thesis improves the modeling and interpretation of impedance probe measurements. A numerical method is developed that uses electric field data from computer simulations to calculate the impedance of realistic probe and spacecraft geometries.

The influence of the sheath on the probe's resonant frequencies is analyzed, and the results are compared to measurements from the Scintillation Prediction Observation Research Task (SPORT) satellite mission. The comparison shows that sheath effects have no effect on the measurement for plasma density, but need to be understood when comparing real-world data to theory.

A new impedance probe circuit is also designed and tested to expand the measurement range and improve accuracy. These developments contribute to better electron density measurements.

CONTENTS

LIST OF TABLES

LIST OF FIGURES

ACRONYMS

ADC	Analog-to-digital converter
DDS	Direct digital synthesis
DDS	Direct digital synthesis
FPGA	Field-programmable gate array
FIFO	First-in, first-out memory buffer
IGRF	International Geomagnetic Reference Field
NCO	Numerically controlled oscillator
PCB	Printed circuit board
RF	Radio frequency
SPORT	Scintillation Prediction Observations Research Task
TIA	Trans-impedance amplifier
UART	Universal asynchronous receiver–transmitter
VNA	Vector network analyzer

CHAPTER 1

Introduction

1.1 The Ionosphere

The Earth is surrounded by an upper atmospheric region known as the ionosphere, a layer where solar ultraviolet radiation strips electrons from atoms and molecules, creating a mixture of charged and neutral particles called plasma. The ionosphere plays an essential role in everyday life such as bending, reflecting, and modifying the radio waves that support technologies like Global Positioning System (GPS) navigation, satellite communications, and high-frequency (HF) radio. One of the most important parameters of the ionosphere is its electron density which is a measure of how many free electrons exist in a given volume of space. Variations in electron density strongly influence how radio signals travel, often degrading or disrupting them.

The ionosphere does not behave in isolation. It is shaped from above by solar activity such as solar flares and the solar wind, but also from below by atmospheric waves, tides, and weather systems that propagate upward from the lower atmosphere. The interaction of these two "drivers" creates what we broadly call 'space weather', which describes the changing plasma and electromagnetic environment around the Earth. Just as terrestrial weather affects aviation or agriculture, space weather affects satellite operations, power grids, GPS positioning accuracy, as well as military and commercial communication systems. Understanding and forecasting these conditions requires accurate and frequent measurements of electron density across the globe.

One example of space-weather-driven disturbances is the formation of Equatorial Plasma Bubbles (EPBs). These phenomena begin shortly after sunset near the Earth's magnetic equator effecting a belt of latitudes approximately 60° wide around the Earth's equator. EPBs are regions of low plasma density that rise upward through the surrounding iono-

sphere. As these "bubbles" rise, they generate turbulence and small-scale irregularities in electron density. These irregularities scatter and diffract radio signals that pass through them in a process known as scintillation. Scintillation can severely degrade GPS accuracy, disrupt satellite communication links, and interfere with scientific measurements. EPBs are the primary cause of scintillation disruptions of RF signals at low latitudes.

Because EPBs and other ionospheric disturbances can evolve rapidly with features as small as tens or hundreds of meters, space weather researchers rely on in-situ satellite measurements to capture the fine-scale structure of the plasma. While ground-based tools such as ionosondes or radar can monitor the ionosphere from below on much larger scales, satellites pass directly through the ionospheric plasma and can sample electron density at very high spatial and temporal resolutions. A spacecraft traveling at roughly 7.5 km/s and sampling one-hundred times per second can spatially sample electron density with resolution of 75 meters. This capability is essential for observing this scale of irregularities which are responsible for scintillation.

Among the instruments used for these in-situ measurements, Langmuir probes and less frequently impedance probes, are employed on research satellites. Langmuir probes collect charged particles at a fixed or swept voltage, while impedance probes infer electron density by measuring the electrical impedance of a probe interacting with the surrounding plasma at radio frequencies.

This thesis focuses on improving the theory and implementation of ionospheric impedance probes. By advancing the capacitive models and refining the interpretation of impedance measurements. These improvements directly contribute to our understanding of ionospheric variability, scintillation forecasting, and support the space-based communication and navigation technologies.

1.2 Impedance Probe Concepts

To understand how an impedance probe measures electron density on a satellite, it is useful to view the instrument as a small antenna or probe whose electrical behavior is modified by the surrounding ionospheric plasma. When the probe is driven with a sinusoidal

signal, the plasma affects how easily current can flow to and from the probe, the ratio of this drive voltage and measured current is the impedance. Two distinct resonances appear in the impedance measurement. The first, known as the lower series resonance, is associated with the influence of the geomagnetic field and the circular motion of electrons around the magnetic field lines. Electrically, this resonance behaves like a series connected Resistor-Inductor-Capacitor (RLC) circuit. At higher frequencies, a second resonance occurs that arises from the collective motion of electrons oscillating relative to the more massive ions. This is referred to as the upper parallel resonance, and it behaves electrically like a parallel connected RLC circuit. The frequency at which this upper parallel resonance occurs is strongly dependent on the local electron density.

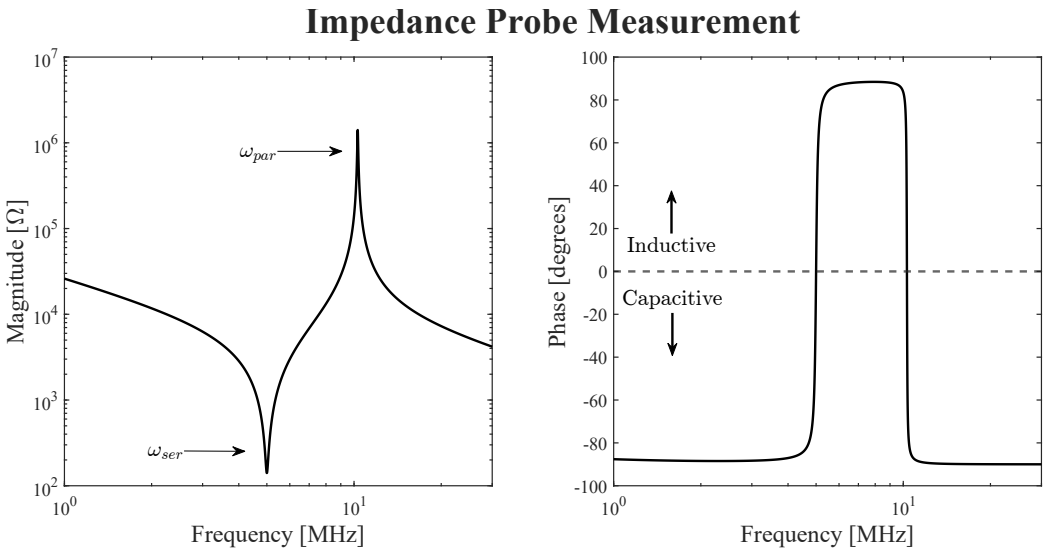

Fig. 1.1: A theoretical impedance sweep.

Figure 1.1 depicts a theoretical impedance measurement sweep for an impedance probe immersed in a cold-magnetized plasma. The left panel displays the magnitude of the probe impedance as a function of frequency and the right panel displays the corresponding phase. Both resonances appear as distinct features in these curves. The upper parallel resonance is expressed as a sharp peak in magnitude and a rapid phase transition from inductive to capacitive. This behavior allows its location to be determined with high precision. Because

the frequency of this resonance depends directly on the electron density, identifying it in the sweep provides a means of determining the local plasma density. This resonance-based approach forms the foundation of both the sweeping and tracking measurements of impedance probes.

1.3 SPORT Mission Overview

The Scintillation Prediction Observations Research Task (SPORT) is an example of a new class of scientific missions aimed at understanding space weather. Developed jointly by the United States and Brazil and deployed from the International Space Station in late 2022, SPORT was designed to investigate the ionospheric processes that lead to EPBs and the resulting scintillation disturbances that degrade communication and navigation systems.

SPORT's science mission was implemented using a suite of in-situ plasma sensors developed by Utah State University, the University of Texas at Dallas (UTD), The Aerospace Corporation, and NASA Goddard, integrated onto a 6U Brazilian spacecraft. UTD's Ion Velocity Meter measured ion drifts and temperatures along the ram direction, the Aerospace CTECS instrument retrieved total electron content from GPS occultations, and NASA Goddard's miniature magnetometer provided vector magnetic-field data. An overview of the sensor layout and boom geometry is shown in the accompanying Figure 1.2.

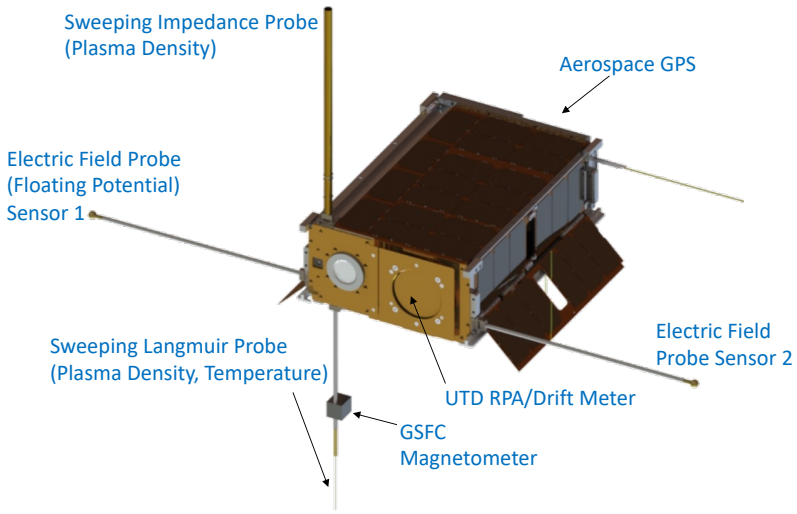

Fig. 1.2: SPORT spacecraft with labeled instruments.

Most relevant to this thesis is the Space Weather Probes (SWP) instrument suite, which included a sweeping Langmuir probe, floating potential probes, and the Impedance Probe. Mounted on deployable booms positioned on the ram-facing side of the spacecraft, these sensors were designed to measure plasma density, temperature, and potential. The electronics were integrated onto a single 9.0 × 9.6 cm printed circuit board (PCB). In addition to its scientific role, the SWP suite also served as a technology demonstration to see whether these ionospheric probes could be successfully miniaturized for future CubeSat applications.

The spacecraft's attitude determination and control system failed, leaving it in a slow tumble, but the science instruments continued to function. This loss of orientation introduced challenges for interpreting measurements from the SWP; however, the measurements made by SWP can still be analyzed and compared to theory. The impedance probe provides the primary dataset used in this thesis and is the inspiration for theoretical work and improved probe architecture presented.

1.3.1 SPORT Impedance Probe

The impedance probe on SPORT has two modes. In the Sweeping Impedance Probe

(SIP) mode, the probe stimulus is swept from 2 - 30 MHz, measuring the probe impedance at 512 logarithmically spaced points. In the tracking impedance probe (TIP) mode, the parallel resonance is tracked via a digital control loop to measure the frequency at which this resonance occurs. TIP data is produced at a sample rate of 100 Hz and provides a high-resolution measurement of the plasma density. The TIP runs continuously while the SIP sweeps every two minutes to provide a sanity check that the probe is correctly functioning.

Figure 1.3 presents a 30-minute section of data from the SPORT mission showing the electron density variation of the low latitude ionosphere [1]. The two peaks (crests) result from the well known space weather fountain effect: The interaction of an eastward electric field and the near horizontal nature of Earth's magnetic field near the equator. These fields create a drift that lifts plasma over the magnetic equator. This lifted plasma then diffuses down the magnetic field lines due to gravity and pressure gradients, accumulating at off-equatorial locations.

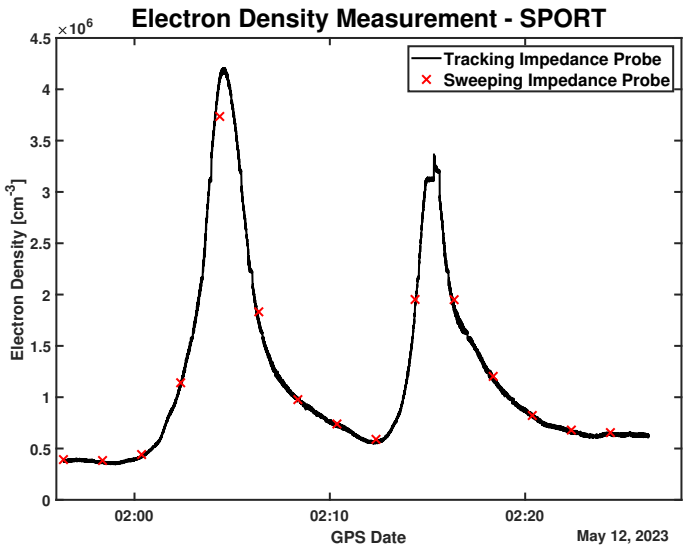

Fig. 1.3: SPORT sweeping and tracking impedance probe measurements.

1.3.2 SPORT Impedance Probe Limitations

The SPORT SWP Impedance Probe measures the impedance by an excitation voltage applied to the sensing probe, and the resulting current is measured through a current-sense

transformer. Prior to launch, the excitation voltage was tuned to a small signal level of approximately 100 mV to avoid nonlinear effects. However, the excitation voltage was not directly measured in flight. For large probe impedances, such as at the parallel resonance sensed in the TIP mode, this is not a concern. However for low impedances the output impedance of the drive amplifier introduces loading effects that cause systematic error in the measured impedance curves. These errors were most apparent at the series resonance where the probe impedance is at a minimum.

A separate challenge arose from the SPORT spacecraft's attitude determination and control system, which failed early in the mission. Without reliable attitude knowledge, it was not possible to determine the orientation of the impedance probe relative to the geomagnetic field. This uncertainty is important because the observed resonance frequencies depend on the probe's angle to the magnetic field, particularly in regions of strong magnetic field or low plasma density. This challenge motivates the modeling approaches developed in later chapters, which accommodate uncertain magnetic field orientation.

1.4 Literature Review

1.4.1 USU Impedance Probe Instrumentation

Over the past decades, Utah State University has developed a line of impedance probe instruments that extends from early rocket experiments in the 1960's to the Floating Potential Measurement Unit (FPMU) on the International Space Station and to modern CubeSat missions such as SPORT. The following review presents the development of the impedance probe hardware at USU, tracing how theses have advanced the analog front end, the signal processing methods, and the firmware architectures that now define the impedance probe as part of the Space Weather Probes instrument.

Earl F. Pound was one of the principal engineers at the Utah State University Space Dynamics Laboratory during the 1970s and 1980s and played a foundational role in the early development of radio frequency impedance and capacitance probes for ionospheric research [2]. Before digital signal processing techniques, now used in modern USU in-

struments, Pound designed and refined heterodyne and superheterodyne detection systems that enabled sensitive measurement of probe impedance. His dissertation addressed the problem of electron density measurement in the D region of the ionosphere, where the electron–neutral collision frequency is sufficiently large that the upper parallel and lower series resonances are strongly damped and no longer appear as distinct features in the impedance measurement. Pound developed techniques to measure small deviations in the effective capacitance and demonstrated that these capacitance variations could be used to infer ambient electron density. His work extended the impedance probe technique into areas where resonance-based methods failed.

Wayne Sanderson's 2007 thesis documents the entire early period of the impedance probe development [3]. As summarized in his review, earlier missions relied on a wideband current sense transformer to measure the RF current. Later instruments migrated to a trans-impedance (TIA)-based front end. Sanderson's work shows that although the TIA architecture succeeded in miniaturizing the electronics and simplifying the analog chain, the required guarding structures around the high-impedance amplifier inputs imposed practical limits on performance by increasing sensitivity to input shunt capacitances and degrading the high-frequency response.

Julio Martin Hidalgo's 2014 thesis reintroduces the transformer based current measurement topology [4]. Martin Hidalgo also replaced the stand alone phase detector circuits used in some prior designs with a quadrature sampling scheme that mixed the measured current to obtain in-phase (I) and quadrature-phase (Q) signals. The resulting I and Q signals were digitized and processed to recover both magnitude and phase. His work modernized the analog front end and produced an architecture that formed the basis of the next generation of instruments.

Caleb Young's 2020 thesis extended this architecture to the SPORT mission and established the first fully digital sweeping impedance probe design [5]. Young migrated the mixing and filtering to a SmartFusion2 FPGA. A tracking mode was added to track to the upper parallel resonance and provide continuous measurement of the electron density.

Nicholas Wallace's 2023 thesis completed the architectural transition to a model based firmware system for the Space Weather Probes Version 2 instrument suite [7]. Wallace developed the command, control, and data handling framework that integrates all of the SWP2 instruments within a PolarFire FPGA. Benjamin Lewis's 2023 thesis extends the Wallace architecture by developing the digital signal processing back-end for the SWP2 Impedance Probe [8]. Lewis implemented all frequency generation, synchronous detection, decimation, averaging, and phase extraction functions in a model based Simulink environment and validated the system against simulated plasma transfer functions before synthesizing it for the PolarFire FPGA. His work completed the digital backend for the SWP2 Impedance Probe and established a flight ready signal processing system.

Together these theses document a clear evolution of impedance probe hardware at Utah State University. Sanderson captured the historical development and identified the limitations of the trans-impedance amplifier. Martin Hidalgo returned to the transformer based current measurement approach and introduced a modern quadrature detection system. Young produced the first integrated multi instrument Space Weather Probes system and delivered a fully digital sweeping and tracking impedance probe for the SPORT mission. Wallace unified the multi instrument firmware within a model based development environment. Lewis completed the digital back-end for the impedance probe with a flight ready signal processing chain.

1.5 Research Objectives and Methodology

Versions of the impedance probe technique have been used for more than 50 years on sounding rockets and satellites, yet detailed interpretation of the data remains challenging due to the combined effects of complex spacecraft geometries, magnetic field orientation, plasma sheath formation, and practical circuit limitations. The SPORT mission in particular revealed discrepancies between simplified analytical impedance models and flight data, highlighting the need for more sophisticated modeling tools and improved instrumentation.

To address these challenges, this thesis pursues three research objectives:

1. Development of a numerical approach for computing the impedance of spacecraft-mounted probes in a cold-magnetized plasma,

2. Incorporation and analysis of plasma sheath effects in analytical models to understand their influence on measured impedance resonances, and

3. Design and demonstration of a new impedance probe circuit that improves measurement accuracy across a wide impedance range.

1.5.1 Numerical Solution for the Capacitive Probe Theory

The first objective is to establish a numerical method for determining the impedance of a probe for realistic probe and spacecraft geometries immersed in a cold-magnetized plasma. Analytical expressions for capacitive probe theory exist for simple geometries like parallel plates, concentric cylinders, concentric spheres, and a cone over a ground plane. These simple geometries are not sufficient for real-world data comparisons because the symmetries used to find the impedance do not exist, especially when introducing arbitrary magnetic field angles.

This objective will be accomplished by obtaining Electric-field solutions using the ANSYS Maxwell finite-element solver. Solutions are then exported to MATLAB, where the cold-magnetized plasma permittivity tensor is rotated into the appropriate magnetic field direction. This tensor rotation allows for any arbitrary magnetic field angle in the impedance solution. The electric displacement flux is then numerically integrated to determine the capacitance. Figure 1.4 outlines this approach.

The numerical method will first be validated by comparing its results against analytical expressions for the geometry concentric cylinders. Once validated, the method will be applied to the SPORT probe-spacecraft geometry and compared to on-orbit data. By validating the method against known analytical solutions and then applying it to the SPORT spacecraft geometry, the thesis demonstrates how real probe configurations deviate from idealized models and establishes a path toward more reliable interpretation of impedance measurements for future missions.

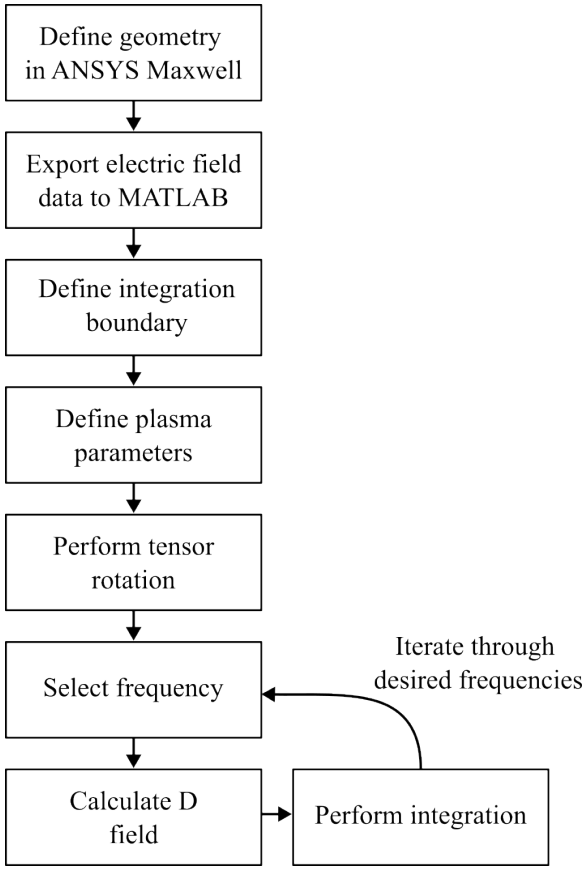

Fig. 1.4: General approach for numerically calculating the probe impedance.

1.5.2 Analysis of Sheath Effects

The second objective examines how the plasma sheath influences the impedance measured by the probe. A sheath naturally forms around spacecraft and sensor surfaces because the negatively charged spacecraft repels electrons and gathers ions. To incorporate this behavior, capacitive probe theory is modified to include a simplified sheath represented as an abrupt, electron-depleted boundary layer. From this simplified sheath model, the modified impedance is modeled as an additional capacitance in series with the plasma reactance. Writing these expressions in rational form makes it possible to identify how the series and parallel resonances vary with plasma frequency, magnetic field orientation, sheath thickness, and probe geometry. These analytical results are then compared directly with SPORT SIP data to evaluate the extent to which sheath effects alter the resonant frequencies observed

in flight. While the sheath does not affect the determination of the plasma density from the parallel resonance measurement, the analysis demonstrates that it significantly influences the series resonant frequency and must be accounted for when comparing measurements to theoretical predictions.

1.5.3 New Impedance Probe Circuit Design

The third objective focuses on designing and demonstrating a new impedance probe circuit that improves measurement accuracy across a wide impedance range. Historical USU impedance probes apply a small RF voltage and sense the resulting current through a current transformer, an approach that often exhibits limited dynamic range, susceptibility to leakage currents, and reduced accuracy at high impedances. To overcome these limitations, this thesis develops a circuit based on an auto-balancing bridge topology capable of operating from 1 to 30 MHz. A conceptual diagram of this system is shown in Figure 1.5.

This objective includes the design and fabrication of a complete test-board including the stimulus generation, reconstruction filter, hand-wound transformer for isolation and impedance scaling, sensing circuitry, and FPGA-based mixing, averaging, and data handling. The schematic capture is performed in KiCad, and the analog design, including filtering and voltage sense circuits, are simulated in LTspice before fabrication. After assembly, the board is evaluated using oscilloscope measurements and a Vector Network Analyzer to verify its functionality. The FPGA firmware, developed in the MATLAB Simulink environment, performs synchronous sampling of the sensed signals then transfers the processed data to a computer over UART for calibration and post-processing.

In addition to the circuit development, two guarding techniques are investigated to remove leakage currents from the measurement that degrade the instrument performance in plasma environments. Together, these developments establish the practical considerations necessary for implementing impedance probe electronics for future spaceflight missions.

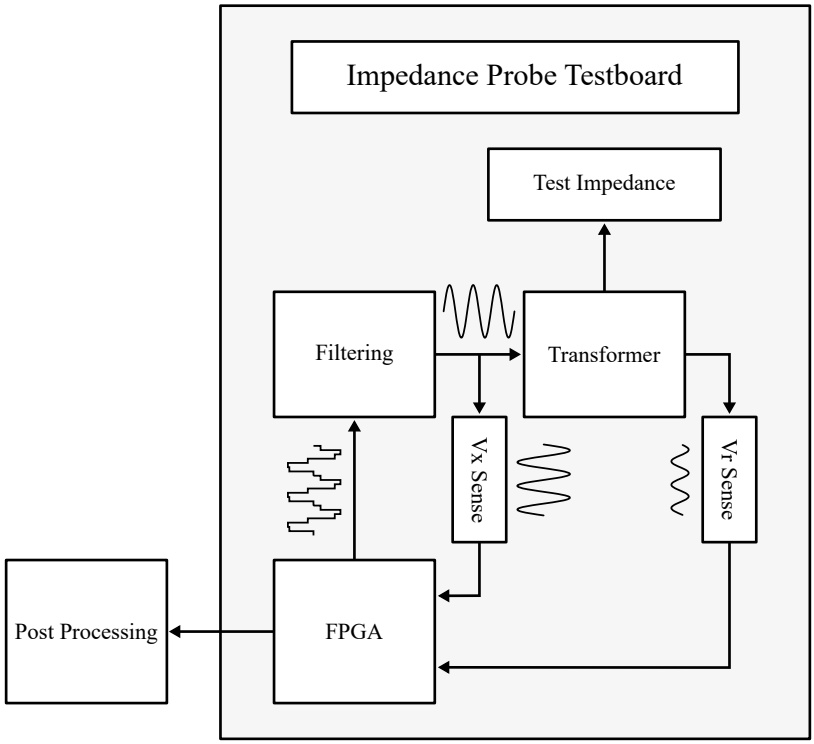

Fig. 1.5: Basic diagram for the Impedance Probe Testboard.

1.6 Description of Thesis

This thesis is organized into six chapters. A brief summary of each chapter is provided below to guide the reader through the structure and contributions of the work.

Chapter 1: Introduction Chapter 1 provides the scientific motivation and context for the thesis by describing the role of ionospheric electron density in the formation of Equatorial Plasma Bubbles (EPBs) and their impacts on communication, navigation, and space-based systems. The chapter also reviews the measurement principles behind impedance probes. It then outlines the limitations revealed through SPORT flight data, particularly the need for improved modeling of probe impedance, better understanding of plasma-sheath effects, and more accurate impedance-probe instrumentation. Lastly, the research objectives are stated.

Chapter 2: Impedance Probe Theory and Measurement Chapter 2 provides an overview for how the permittivity tensor of a cold-magnetized plasma is derived. The

plasma dynamics are used to derived a set of fluid equations, which are coupled with Maxwell's equations in order to solve for the complex permittivity tensor. This permittivity tensor is what is used for characterizing how a probe responds in a cold-magnetized plasma environment. Additionally, Chapter 2 provides an overview of various impedance measurement techniques including S-parameter, I-V, and auto-balancing bridge methods.

Chapter 3: Numerical Impedance Solution Chapter 3 develops a numerical approach for modeling the impedance of a probe immersed in a cold-magnetized plasma with realistic geometries and arbitrary magnetic field angles. The probe-to-craft impedance is computed by integrating the displacement-field flux derived from electrostatic solution from ANSYS Maxwell. This approach is compared to analytical expressions for simple geometries and to the SPORT probe geometry to validate accuracy of the numerical approach.

Chapter 4: Plasma Sheath Analysis Chapter 4 investigates how the plasma sheath that forms around the probe and spacecraft modifies the measured impedance. A finite vacuum layer is introduced to represent the sheath capacitance, which appears in series with the plasma reactance. The chapter derives rational expressions for the resulting impedance and uses them to identify the series and parallel resonances. These predictions are compared to numerical simulations and to SPORT flight data.

Chapter 5: Impedance Probe Circuitry Chapter 5 presents the design, implementation, and testing of a new impedance-probe instrument based on an auto-balancing bridge. The measurement chain includes stimulus generation, transformer isolation, sensing electronics, FPGA-based I/Q mixing and averaging, and calibration. The chapter also evaluates two guarding strategies—grounded and equipotential—to suppress leakage currents that otherwise compromise measurement accuracy in spacecraft environments.

Chapter 6: Conclusion Chapter 6 summarizes the thesis contributions: the development of a generalizable numerical method for computing probe impedance; an analytical framework incorporating sheath effects and resonance behavior; and an experimentally validated measurement circuit. The chapter concludes with recommendations for future work, including extensions to warm-plasma modeling, nonlinear-sheath, and further improvements of the auto-balancing bridge circuitry.

CHAPTER 2

Impedance Probe Theory and Measurement

This chapter provides the theoretical and measurement foundations for interpreting impedance probe data. The first section reviews the theory that leads to the anisotropic permittivity that is used in the analytic capacitance formulation of an impedance probe's interaction with the ionosphere. The second section introduces measurement techniques used to observe impedances.

2.1 Theory Review

2.1.1 Fluid Model of Ionospheric Plasma

Figure 2.1 illustrates how a cold-magnetized permittivity tensor is derived from the dynamical description of a plasma.

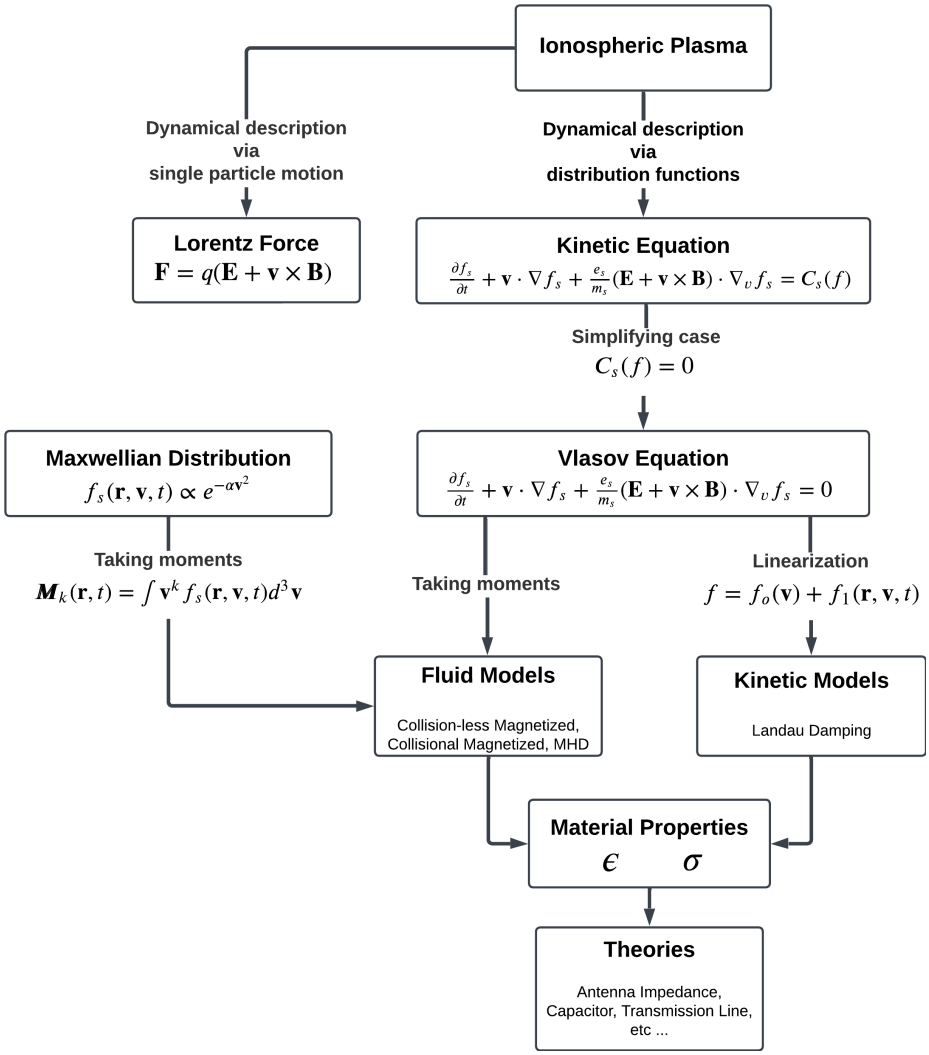

Fig. 2.1: Overview for material property derivation.

The ionospheric plasma may be viewed as a collection of charged particles were the motion of an individual particle is governed by the Lorentz force,

$$\vec{F} = q\,(\vec{E} + \vec{v} \times \vec{B}), \tag{2.1}$$

which describes how electrons and ions accelerate in response to electromagnetic fields. While this single particle description provides some physical intuition, it is not sufficient for predicting the collective behavior of the many particle system surrounding an impedance

probe.

Another description is obtained by introducing a distribution function $f_s(\vec{r}, \vec{v}, t) \in \mathbb{R}^7$, which specifies the number of particles of species s at a given location and velocity. The evolution of this distribution is governed by the Boltzmann kinetic equation. For Ionospheric plasma, where the number of collisions between neutral and charged particles is small, the equation reduces to the Vlasov equation,

$$\frac{\partial f_s}{\partial t} + \vec{v} \cdot \nabla f_s + \frac{q_s}{m_s}(\vec{E} + \vec{v} \times \vec{B}) \cdot \nabla_v f_s = 0, \tag{2.2}$$

which expresses the coupling between the particle distribution dynamics and the electromagnetic fields. Linearizing the Vlasov equation about an equilibrium Maxwellian distribution leads to the standard kinetic descriptions of wave–particle interactions. A full kinetic treatment is required to describe the detailed behavior of the probe near the series and parallel resonances, particularly for phenomena such as Landau damping that cannot be captured with the fluid expressions. However, a complete, fully magnetized kinetic description of a probe in a plasma does not currently exist due to the mathematical complexity of the problem.

To obtain macroscopic quantities, velocity moments of the distribution function are taken, as outlined in Figure 2.1. This procedure yields the fluid equations for species density, momentum, and pressure [11]:

$$\frac{\partial n_j}{\partial t} + \nabla \cdot (n_s \vec{v}_j) = 0 \tag{2.3}$$

$$m_j n_j \left(\frac{\partial \vec{v}_j}{\partial t} + (\vec{v}_j \cdot \nabla)\vec{v}_j \right) = q_j n_j (\vec{E} + \vec{v}_j \times \vec{B}) - \nabla P_j - n_j m_j \nu (\vec{v}_j - \vec{u}) \tag{2.4}$$

$$P_j = C_j n_j^{\gamma_j} \text{ but usually } P_j = n_j k_b T_j. \tag{2.5}$$

These equations describe conservation of mass and momentum for each plasma species and are coupled with Maxwell's equations:

$$\epsilon_0 \nabla \cdot \vec{E} = \sum_{k=1}^{j} q_j n_k \tag{2.6}$$

$$\mu_0^{-1} \nabla \times \vec{B} = \sum_{j=1}^{k} q_k n_k \vec{v}_k + \epsilon_0 \frac{\partial \vec{E}}{\partial t} \tag{2.7}$$

$$\nabla \times \vec{E} = -\frac{\partial \vec{B}}{\partial t} \tag{2.8}$$

$$\nabla \cdot \vec{B} = 0 \tag{2.9}$$

To determine the dielectric response of the plasma, the fluid equations are linearized and combined into a modified Poisson's equation,

$$\epsilon_0 \nabla \cdot (I + \boldsymbol{\chi}) \vec{E} = \rho_f \tag{2.10}$$

with the relative permittivity $\boldsymbol{\epsilon}_r = I + \boldsymbol{\chi}$. Neglecting temperature effects gives the cold-magnetized plasma permittivity tensor:

$$\boldsymbol{\epsilon}_r = \begin{bmatrix} \epsilon_1 & -j\epsilon_2 & 0 \\ j\epsilon_2 & \epsilon_1 & 0 \\ 0 & 0 & \epsilon_3 \end{bmatrix} \tag{2.11}$$

with

$$\epsilon_1 = 1 + \frac{\omega_p^2 \omega^\star}{\omega(\Omega^2 - \omega^{\star 2})} \qquad \epsilon_2 = \frac{\omega_p^2 \Omega}{\omega(\Omega^2 - \omega^{\star 2})} \qquad \epsilon_3 = 1 - \frac{\omega_p^2}{\omega \omega^\star} \tag{2.12}$$

and

$$\omega^\star = \omega - j\nu \qquad \Omega = \frac{eB_0}{m_e} \qquad \omega_p = \sqrt{\frac{n_0 e^2}{\epsilon_0 m_e}}. \tag{2.13}$$

where the tensor elements depend on the plasma frequency ω_p, the cyclotron frequency Ω, and the collision rate ν. The plasma frequency is directly related to the ambient electron density, n_0. The cyclotron frequency arises from the presence of a magnetic field and is the

rate at which a charged particle orbits within a static magnetic field. The collision frequency, ν is the rate of collisions of charged particles with neutral particles, which remove energy from the system resulting in damping effects.

The progression from single particle motion, to kinetic theory, to macroscopic fluid models provide a complex but limited dielectric response of the plasma surrounding a spacecraft mounted sensor. These material properties feed directly into the impedance probe models provided in Section 2.1.2, where the probe geometry, and cold-magnetized plasma dielectric combine to determine the probe impedance.

2.1.2 Impedance Probe Theory

The impedance of a probe immersed in a plasma may be determined in several ways, depending on how the system is modeled. The terminal impedance is defined through the relationships of the applied voltage, the resulting current, or the complex power transferred to the plasma. This requires solving Maxwell's equations in a cold-magnetized, anisotropic, and dispersive medium which is analytically manageable only for very simple conditions.

To make this problem manageable, early researchers developed a simplified form of the complex-power method known as the induced electromotive force method. An approach by Balmain was to assume a triangular current distribution on the probe [9]. From this assumed current, the fields produced in the plasma are computed. The impedance is then extracted in one of two equivalent ways.

First, if both the electric and magnetic fields are available, the complex power delivered to the plasma can be computed from the Poynting vector:

$$P = \frac{1}{2}\int_S (\vec{E} \times \vec{H}^*) \cdot \hat{\mathbf{n}}\, dS, \tag{2.14}$$

where the integration is carried out over a surface enclosing the probe. Relating this power to the terminal voltage and current through

$$P = \frac{1}{2} V I^* \tag{2.15}$$

yields the input impedance.

Another form of the induced–EMF method avoids the explicit computation of the magnetic field. Because the assumed current distribution is known, the electric field it produces in the plasma may be used directly to determine the voltage along the probe:

$$V = -\int_{\ell} \vec{E} \cdot d\boldsymbol{\ell}. \tag{2.16}$$

The impedance then follows simply from

$$Z = \frac{V}{I}. \tag{2.17}$$

This formulation is mathematically equivalent to the Poynting-vector approach, but is significantly easier to evaluate in magnetized plasmas where the electric field is more readily obtained.

A different approach treats the probe primarily as a capacitive object immersed in the plasma. In this approach, the applied voltage induces an electric displacement field in the plasma, from which the total charge induced on the probe surface is computed:

$$Q = \oint_{\text{probe}} \vec{D} \cdot d\vec{A}, \qquad \vec{D} = \boldsymbol{\epsilon}\vec{E}. \tag{2.18}$$

The capacitance is defined as $C(\omega) = Q/V$, and the probe impedance follows directly from

$$Z(\omega) = \frac{1}{j\omega C(\omega)}. \tag{2.19}$$

This approach naturally incorporates the permittivity tensor and is well suited for numerical implementation using electrostatic finite-element solvers. Because ionospheric impedance probes operate in the 1–30 MHz range, the corresponding free-space wavelengths (10–300 m) are much larger than the probe and spacecraft dimensions. Thus, the system behaves capacitively and the probe impedance is dominated by the reactive near-field region. This capacitance method is a self consistent approach, without assumptions of current or

charge distributions over the surface of the probe, and is used in this thesis.

Capacitor Probe Theory

The capacitance-probe technique provides an understanding for how simple geometries interact with a cold-magnetized plasma. In the USU ECE 7210 course Instrumentation for Space Science, expressions were derived for the effective relative permittivity $\epsilon_r(\omega)$ for several geometries: parallel plates, cylinders, spheres, and a cone above a ground plane. Each expression incorporates the orientation of the geomagnetic field relative to the probe's symmetry axis, allowing the dependence of the series and parallel resonances on magnetic-field angle to be evaluated analytically. The resulting formulas, presented below, form a useful reference for interpreting probe impedance behavior and for validating more detailed numerical models.

The impedance is given by:

$$Z = \frac{1}{j\omega C_0 \epsilon_r} \tag{2.20}$$

where C_0 is the free-space capacitance and ϵ_r is a geometry-dependent effective scalar permittivity. The permittivity for the simple geometries with θ being the direction of the magnetic field from the z-axis down are given by:

$$\epsilon_{r_{\text{plate}}} = \epsilon_1 \sin^2\theta + \epsilon_3 \cos^2\theta \tag{2.21}$$

$$\epsilon_{r_{\text{cylinder}}} = \epsilon_1(1 + \cos^2\theta) + \epsilon_3 \sin^2\theta \tag{2.22}$$

$$\epsilon_{r_{\text{sphere}}} = \frac{2}{3}\epsilon_1 + \frac{1}{3}\epsilon_3 \tag{2.23}$$

$$\epsilon_{r_{\text{cone}}} = \epsilon_1\left(\sin^2\theta\sin^2\alpha + \frac{1}{2}\cos^2\alpha(1+\cos^2\theta)\right) + \epsilon_3\left(\cos^2\theta\sin^2\alpha + \frac{1}{2}\cos^2\alpha\sin^2\theta\right) \tag{2.24}$$

This formulation neglects sheath and temperature effects, but sheath contributions can be incorporated by modeling a finite vacuum boundary surrounding the probe [12].

2.1.3 Plasma Sheath

A conductive body immersed in plasma does not remain electrically neutral relative to the surrounding ambient plasma. Electrons, which possess much higher thermal velocities than ions due to their lower mass, strike the conductive body far more frequently than ions do. As a result, conductive surfaces naturally acquire a negative charge relative to the surrounding plasma. This charging process continues until the surface potential becomes sufficiently negative that it repels incoming electrons and attracts enough ions to balance the net current to the surface. The equilibrium potential is typically < 1 V negative in the dense plasma of the lower ionosphere.

The presence of a biased surface in plasma leads to the formation of a boundary region known as the plasma sheath. The sheath is a non-neutral layer, typically a few Debye lengths thick, in which the plasma potential transitions smoothly from the spacecraft potential to the undisturbed ambient potential. Within this region, the electron density is depleted relative to the ambient plasma because the negatively charged surface repels low-energy electrons. Ions, on the other hand, are accelerated toward the surface. A non-linear mathematical description for a one-dimensional case of the potential structure in the sheath is:

$$\frac{\partial^2 \phi(x)}{\partial x^2} = \frac{e}{\epsilon_0}(n_e - n_i). \tag{2.25}$$

Where n_e and n_i are the electron and ion densities respectively. Assuming a Boltzmann distribution of electrons and an energy equation for ions at the edge of the sheath, the potential is given as [13]

$$\frac{\partial^2 \phi(x)}{\partial x^2} = \frac{e n_o}{\epsilon_0}\left(\exp\left(\frac{e(\phi(x)-\phi_p)}{k_b T_e}\right) - \left(1 - \frac{e(\phi(x)-\phi_p)}{\frac{1}{2}m_i v_{is}^2}\right)^{-\frac{1}{2}}\right). \tag{2.26}$$

Assuming the ions are immobile and linearizing 2.26 yields

$$\frac{\partial^2 \phi(x)}{\partial x^2} = \frac{1}{\lambda_D^2}(\phi(x) - \phi_p) \tag{2.27}$$

where

$$\lambda_D^2 \coloneqq \frac{\epsilon_0 k_b T_e}{n_o e^2} \tag{2.28}$$

is the Debye length.

In low Earth orbit (LEO), the sheath structure is influenced not only by surface charging but also by the spacecraft's high orbital velocity, which produces a ram–wake asymmetry in the local plasma environment. The ram-facing side of the spacecraft encounters a compressed, enhanced-density plasma due to the supersonic flow of the ionospheric ions, whereas the wake-facing side experiences a depleted plasma region. As a consequence, the sheath thickness, shape, and potential distribution vary across the spacecraft's surfaces. These variations become especially important for in-situ plasma sensors, because they modify the effective electrical boundary conditions experienced by probes or instruments.

For impedance probes, the sheath plays a direct role in determining the local electric field distribution and thus the measured impedance. By introducing a vacuum-like region around the sensor, the sheath behaves as an additional capacitive layer in series with the plasma's dielectric response. Understanding the formation and properties of the sheath is therefore essential for interpreting impedance measurements and for modeling how spacecraft charging affects the surrounding plasma environment.

2.2 Impedance Measurement Techniques

S-parameter Method

The S-parameter method is used primarily for high frequencies, measuring wave quantities such as reflection and transmission coefficients. With this method, the impedance is derived by measuring the scattering parameters using Vector Network Analyzer (VNA) type circuitry. There are 3 configurations for measuring the impedance using a VNA, these are the shunt measurement, shunt-thru measurement, and series measurement. Table 2.1, summarizes the impedance and sensitivities for each measurement type [14].

Table 2.1: Impedance measurement using S-parameters

Measurement Configuration	**Impedance Equation**	**Sensitivity** $\left\lvert\frac{\partial Z}{\partial S}\right\rvert$
Shunt	$Z = Z_0\frac{1+S_{11}}{1-S_{11}}$	$\left\lvert\frac{2Z_0}{(1-S_{11})^2}\right\rvert$
Shunt-Thru	$Z = Z_0\frac{S_{21}}{1-S_{21}}$	$\left\lvert\frac{Z_0}{2(1-S_{21})^2}\right\rvert$
Series	$Z = Z_0\frac{1-S_{21}}{S_{21}}$	$\left\lvert\frac{2Z_0}{S_{21}^2}\right\rvert$

Here, Z_0 is the system impedance (typically 50 Ω). The advantage of measuring impedance using S-parameters is the frequency range exceeds 10's of gigahertz, but for the application of measuring ionospheric plasma, the frequency range of interest is 100 kHz - 30 MHz, so the frequency range is not required. In addition to this, S-parameter measurements provide excellent accuracy for impedances near the system impedance (Z_0), but their reliability decreases when measuring higher impedances [15, 16].

I-V Method

The current–voltage (I–V) technique is used in both low-frequency and RF impedance measurements. The voltage is sensed across the load and the current is measured through the load, typically using a current-sense transformer. Then the impedance is calculated by Ohm's Law

$$Z = \frac{V}{I}. \tag{2.29}$$

The I–V method applies to both low and high frequencies, although its high-frequency performance is limited by the current-sense transformer bandwidth and parasitics. [17]. The I-V method for lower frequencies (100 Hz - 100 MHz) is a good candidate for ionospheric plasma impedance measurement due to its simplicity.

Auto-balancing Bridge

An auto-balancing bridge is a modification of the well known wheatstone bridge in which the null-voltage is automatically driven to 0 via control techniques or a transimpedance op-amp, meaning no manual interaction with a variable resistor is required to measure an unknown impedance. Consider the circuit shown below.

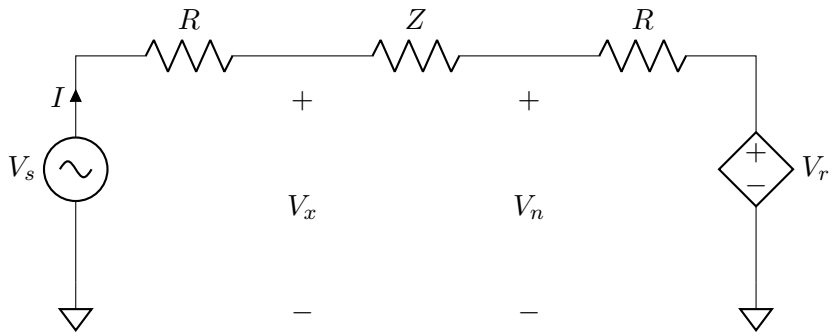

Fig. 2.2: Generic auto-balancing bridge topology.

Resistors R are known quantities and impedance Z is the unknown impedance, which is being measured. Voltage V_s is the sinusoidal stimulus voltage and voltage V_r is the output voltage from a controller. The unknown impedance, Z, can be written as

$$Z = \frac{V_x - V_n}{I}. \tag{2.30}$$

The current can be written as

$$I = \frac{V_n - V_r}{R}. \tag{2.31}$$

Combining 2.30 with 2.31, the unknown impedance is given as

$$Z = \frac{V_x - V_n}{V_n - V_r} R. \tag{2.32}$$

From 2.32, if the null voltage $V_n = 0$, then the impedance is

$$Z = -\frac{V_x}{V_r} R. \tag{2.33}$$

Rearranging equation 2.30, the ideal and error terms are given by

$$Z = \underbrace{-\frac{V_x}{V_r} R}_{\text{ideal}} \underbrace{\left(\frac{\frac{V_n}{V_x} - 1}{\frac{V_n}{V_r} - 1} \right)}_{\text{error}}. \tag{2.34}$$

A common method for generating the controller voltage V_r is with the use of a transimpedance amplifier configuration shown below.

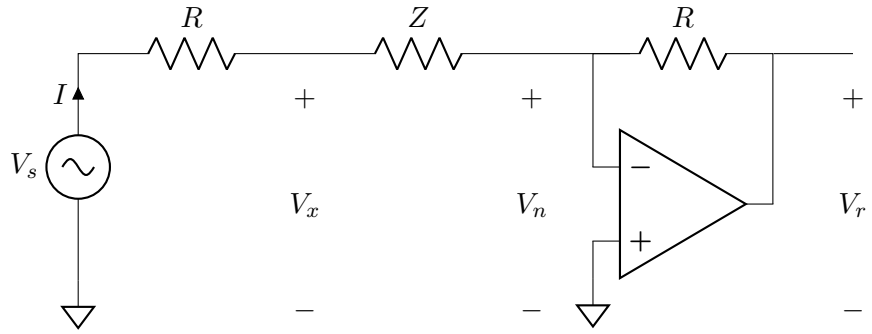

Fig. 2.3: Auto-balancing bridge implemented with a trans-impedance amplifier.

The op-amp functions to generate a voltage V_r to force the potential between the inputs to zero, forming a virtual short. Because the non-inverting input is grounded, the voltage V_r is developed to force the voltage V_n to be zero. This balances the bridge, making the unknown impedance equal to 2.33.

One issue with the op-amp topology for the auto-balancing bridge are high frequency limitations. For the analysis of an ideal op-amp, the potential between the two inputs is always zero across all frequencies; however, for a real op amp that is not the case. The ability for an op-amp to drive the potential between it's to inputs to zero is largely due to

the open loop gain of the op-amp. For most op-amps, this open loop gain begins to fall off fast after 100 kHz. Because the instrument attempts to measure impedances from 1-30 MHz, the voltage V_n will not be zero, leading to errors shown in 2.34.

A summary comparing the accuracy for these methods is shown in the Figure 2.4.

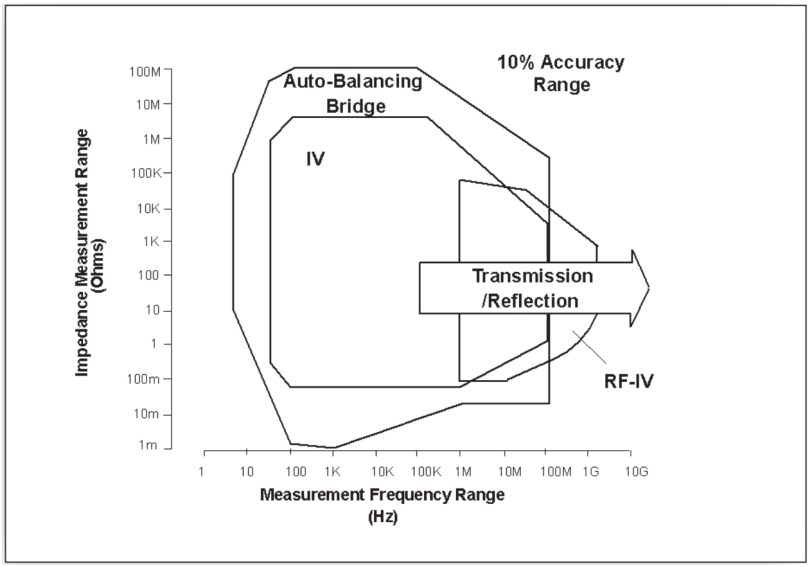

Fig. 2.4: Comparison of different impedance measurement methods.

As can be seen from Figure 2.4, the auto-balancing bridge topology has the widest impedance measurement range and exceeds the frequencies of interest [17].

CHAPTER 3

Numerical Impedance Solution

3.1 Overview

This chapter presents a numerical method for determining the impedance of an impedance probe mounted to a spacecraft immersed in a cold-magnetized ionospheric plasma. The approach combines the electric-field solution computed using ANSYS Maxwell with MATLAB post-processing, which performs tensor rotations and numerical integration. By integrating the electric displacement field over a surface that encloses the probe, the capacitance and therefore the impedance can be obtained for arbitrary geometries. This method enables accurate modeling of probe configurations for which analytical solutions do not exist.

3.2 Maxwell Capacitance Matrix

To begin the process of solving for the impedance of a probe immersed in plasma, an expression for the capacitance is obtained. The Maxwell Capacitance Matrix generalizes capacitance to systems of multiple conductors. For an n-body system, the charge on conductor i is

$$Q_i = \sum_{j=1}^{n} C_{ij} V_i - \sum_{j=2}^{n} C_{ij} V_j. \tag{3.1}$$

Written in matrix form, we obtain the Maxwell Capacitance Matrix

$$Q = \begin{bmatrix} \sum_{i=1}^{n} C_{1i} & -C_{12} & \cdots & -C_{1n} \\ -C_{21} & \sum_{i=1}^{n} C_{2i} & \cdots & -C_{2n} \\ \vdots & \vdots & \ddots & \vdots \\ -C_{n1} & -C_{n2} & \cdots & \sum_{i=1}^{n} C_{ni} \end{bmatrix} V \tag{3.2}$$

where $Q, V \in \mathbb{R}^n$. C_{ij} is the mutual capacitance between conductors i and j, and the

diagonal elements represent self-capacitance [18]. If all conductors except the j-th are held at 0 V, the total charge is given by

$$Q = \begin{bmatrix} -C_{1j} \\ -C_{2j} \\ \vdots \\ \sum_{i=1}^{n} C_{ij} \\ \vdots \\ C_{(n-1)j} \\ C_{ni} \end{bmatrix} V_j \tag{3.3}$$

with $Q \in \mathbb{R}^n$ and $V_j \in \mathbb{R}$. The capacitance between conductors i and j is defined by the total charge on conductor i, scaled by the voltage applied to conductor j. By Gauss's Law, the total charge equals the flux of the electric displacement field $\vec{D}$ through a closed surface surrounding the conductor:

$$Q = \oint_S \vec{D} \cdot d\vec{A}. \tag{3.4}$$

Substituting into the reduced capacitance matrix and letting $V_j = 1$ V gives

$$C_{ij} = -\oint_S \vec{D} \cdot d\vec{A}_i \qquad V_j = 1 \text{ V, all other conductors at 0 V.} \tag{3.5}$$

Figure 3.1 illustrates this idea. Q_1 is set to 1 V, inducing an electric field that couples to bodies Q_2, Q_3, and Q_4. The mutual capacitances C_{12}, C_{13}, and C_{14} are obtained by integrating the electric displacement field flux around each conductor.

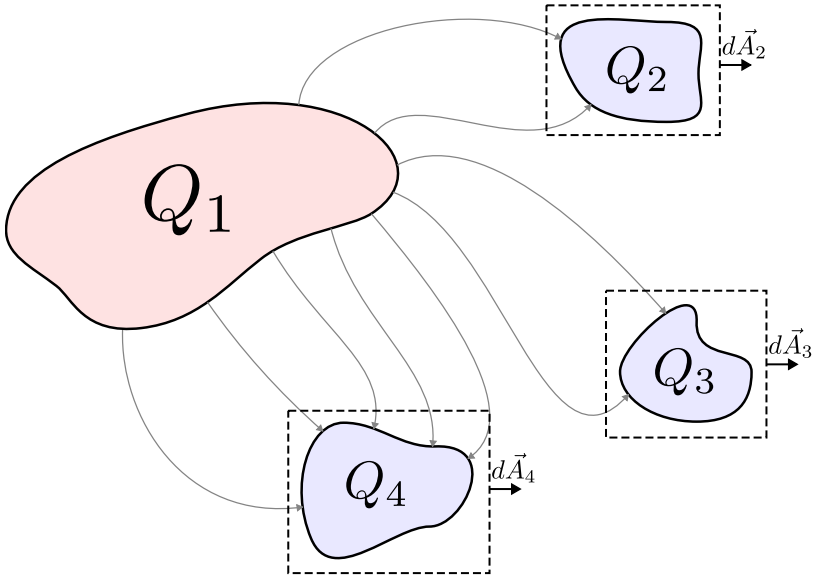

Fig. 3.1: A charged body Q_1 develops an electric field coupled to other bodies. Capacitance is solved through integrating the flux.

This formulation shows that capacitance can be obtained from a surface integral of the electric displacement field surrounding a conductor. Both the conductor and integration surfaces may be arbitrary, provided the integration surface fully encloses the conductor. This expression for the capacitance is used in the numerical solution by numerically integrating the electric displacement field.

3.2.1 Electric Field Solution

Before numerical integration can be performed, the geometry and the corresponding electric-field solution must be obtained using ANSYS Maxwell. The general workflow is as follows.

1. Construct the model

   The probe and spacecraft are built in the ANSYS Maxwell environment using simple shapes such as cubes and cylinders. Each object is assigned an appropriate potential. The solution region is defined around the model, and set to vacuum.

2. Electric Field Solution and data export

The electric field solver computes the electric field for the assigned potentials. Using the field calculator, the field is exported to a comma-separated file that contains the spatial coordinates and the electric-field components. The exported region typically corresponds to the Gaussian surface selected for integration. The exported data is in the format:

X_1	Y_1	Z_1	E_{x1}	E_{y1}	E_{z1}
X_2	Y_1	Z_1	E_{x2}	E_{y1}	E_{z1}
X_3	Y_1	Z_1	E_{x3}	E_{y1}	E_{z1}
$\vdots$	$\vdots$	$\vdots$	$\vdots$	$\vdots$	$\vdots$
X_i	Y_j	Z_k	E_{xi}	E_{yj}	E_{zk}

Here, X, Y, Z specify the position at each sample, and E_x, E_y, E_z are the Cartesian components of the electric field. There are $3 \times (ijk)$ total electric field elements in the complete solution. i is the number of samples in the x-direction, j is the number of samples in the y-direction, and k is the number of samples in the z-direction. In this work, the grid spacing is set to be uniform for all three dimensions.

3.2.2 Tensor Rotation

The cold-magnetized plasma permittivity tensor is defined with the magnetic-field vector aligned with the $\vec{e}_z$ direction. When deriving scalar permittivity expressions for simple geometries, symmetry allows the magnetic-field rotation to be described with a single angle θ. This simplification does not apply for complex geometries that lack symmetry. For an arbitrary magnetic field $\vec{B} \neq B_0\vec{e}_z$, the permittivity tensor must be rotated to a new basis.

Rodrigues' rotation formula is used to construct the rotation matrix. This first requires an axis of rotation and a rotation angle that rotates from the $\vec{e}_z$ direction to a desired $\hat{B}$ direction. The rotation axis $\vec{u}$ and angle θ are found by

$$\vec{u} = \frac{\vec{e_z} \times \vec{B}}{\|\vec{e_z} \times \vec{B}\|_2} \qquad \theta = \arccos\left(\frac{\vec{e}_z \cdot \vec{B}}{\|\vec{B}\|_2}\right). \tag{3.6}$$

The rotation matrix is then

$$R(\vec{u},\theta) = (\cos\theta)I_3 + (\sin\theta)[\vec{u}]_\times + (1-\cos\theta)(\vec{u}\otimes\vec{u}) \tag{3.7}$$

where $[\vec{u}]_\times$ is the cross product matrix defined by

$$\vec{u}\times\vec{v} = [\vec{u}]_\times\vec{v} \qquad [\vec{u}]_\times = \begin{bmatrix} 0 & -u_3 & u_2 \\ u_3 & 0 & -u_1 \\ -u_2 & u_1 & 0 \end{bmatrix}. \tag{3.8}$$

Substituting the rotated permittivity tensor into equation 3.5 gives the capacitance between conductors i and j for an arbitrary magnetic-field direction,

$$C_{ij} = -\oint_S \epsilon_0 R^T \boldsymbol{\epsilon}_r R\vec{E}\cdot d\vec{A}_i \qquad V_j = 1 \text{ V, all other conductors are 0 V.} \tag{3.9}$$

3.2.3 Numerical Solution

The numerical solution begins by reshaping the exported position and electric field data into two matrices $E \in \mathbb{R}^{3\times(ijk)}$ and $XYZ \in \mathbb{R}^{3\times(ijk)}$. They take the form

$$E = \begin{bmatrix} E_x(x_1,y_1,z_1) & E_x(x_2,y_1,z_1) & \cdots & E_x(x_i,y_j,z_k) \\ E_y(x_1,y_1,z_1) & E_y(x_2,y_1,z_1) & \cdots & E_y(x_i,y_j,z_k) \\ E_z(x_1,y_1,z_1) & E_z(x_2,y_1,z_1) & \cdots & E_z(x_i,y_j,z_k) \end{bmatrix}, \tag{3.10}$$

and

$$XYZ = \begin{bmatrix} x_1 & x_2 & \cdots & x_i \\ y_1 & y_1 & \cdots & y_j \\ z_1 & z_1 & \cdots & z_k \end{bmatrix}. \tag{3.11}$$

Only the electric-field values on the boundary of the Gaussian surface are required for calculating the capacitance. A weighting matrix $W \in \mathbb{R}^{3\times(ijk)}$ is constructed for the purpose of selecting only the elements along the boundary. W is created by logically indexing XYZ to find the position elements for integration. Each element of W is assigned a value of $+1$

for a positively oriented surface, a value of -1 for a negatively oriented surface, and a value of 0 for points not located on the Gaussian surface.

From equation 3.9, using the rotated permittivity tensor $\boldsymbol{\epsilon}'_r$, the dot product is written in summation notation

$$C = -\epsilon_0 \oint_S \sum_{i,j} \boldsymbol{\epsilon}'_{r,ij} E_j n_i dA \tag{3.12}$$

with $i, j \in \{x, y, z\}$ being the Cartesian basis, and n_i being the i^{th} component of the unit normal vector. After discretizing the surface into N elements of area Δs^2 and introducing the weighting matrix elements, the expression becomes

$$C = -\epsilon_0 \sum_{i,j} \boldsymbol{\epsilon}'_{r,ij} \underbrace{\sum_{k=1}^{N} E_{j,k} W_{i,k}}_{S_{ji}=EW^T} \Delta s^2. \tag{3.13}$$

The matrix S_{ji} is all contributions of the E_j component through faces in the i^{th} direction. Meaning S_{xx} is the flux contributions of E_x on the x-faces, S_{xy} is the flux contributions of E_x on the y-faces etc. Written in matrix notation, the capacitance for frequency ω is then given as

$$C(\omega) = -\epsilon_0 \Delta s^2 \text{tr}\Big(\boldsymbol{\epsilon}'_r(\omega) S\Big). \tag{3.14}$$

This method for computing the capacitance is computationally efficient. At each frequency step, the matrix multiplication of $\boldsymbol{\epsilon}'_r$ and S is used, instead of integrating all six surfaces individually. This also means that the numerical solution speed does not slow down if a large amount of elements are exported from ANSYS Maxwell. The solution volume XYZ and solution electric field E are reduced from matrices that are $3 \times (ijk)$ to a single matrix $S \in \mathbb{R}^{3\times 3}$. $\boldsymbol{\epsilon}'_r$ is frequency dependent and must be computed at each step, but S does not depend on frequency, thus is computed outside of the loop. The permittivity tensor is not spatially varying in the cold-magnetized model and was able to be pulled out of the summation in 3.13, making this method possible.

The impedance is finally computed using

$$Z(\omega) = \frac{1}{j\omega C(\omega)}. \tag{3.15}$$

3.3 Comparing with Simple Geometries

To validate the accuracy of the numerical solution described above, the cylindrical capacitor is built in ANSYS Maxwell and the impedance is solved for in MATLAB using the dielectric tensor described in 2.1.1. These solutions are compared to the analytical expressions described in 2.1.2. It is noted that the solution volume is restricted such that fringing field effects are not computed. Ignoring fringing field effects is a better comparison to the analytical expressions.

Below in Figure 3.2, the calculated impedance via the numerical method and analytical method are plotted on top of each other.

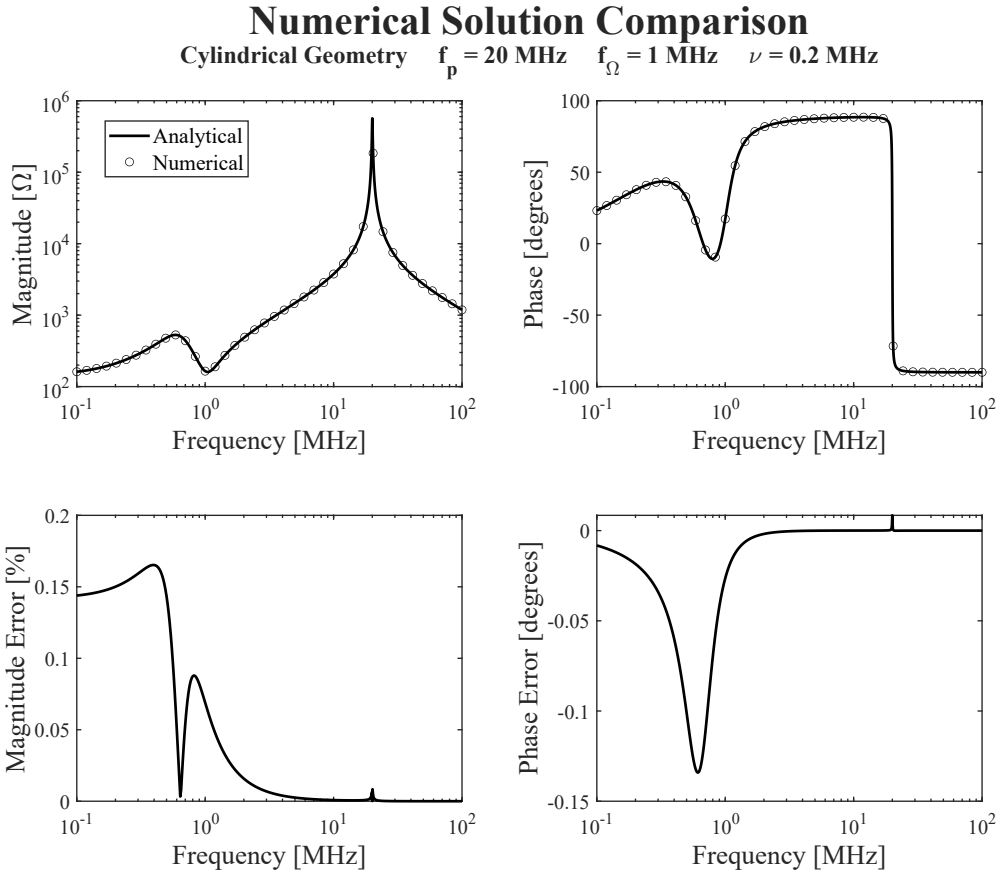

Fig. 3.2: Numerical to analytical comparison for cylindrical geometry.

As seen in Figure 3.2, the impedance magnitude is less than 0.2% over all frequencies and there are phase errors less than 0.15° overall all frequencies. The error is dependent on the plasma parameters ω_p, Ω, ν, and θ. So, an error analysis that incorporates a wide range of plasma parameters is used.

3.4 Error Analysis

To quantify how well the numerical solution matches the analytical solution over a wide range of plasma parameters, the error in the mean of the impedance is taken. To appropriately weigh the wide range of impedances, the log of the impedance is taken. The

normalized root mean squared error (NRMSE) is defined as

$$\text{NRMSE} = \frac{\sqrt{\frac{1}{n}\sum_{i=1}^{n}\left|\log|Z_{\text{numerical}}(\omega_i)| - \log|Z_{\text{analytical}}(\omega_i)|\right|^2}}{\frac{1}{n}\sum_{i=1}^{n}\log|Z_{\text{numerical}}(\omega_i)|}. \tag{3.16}$$

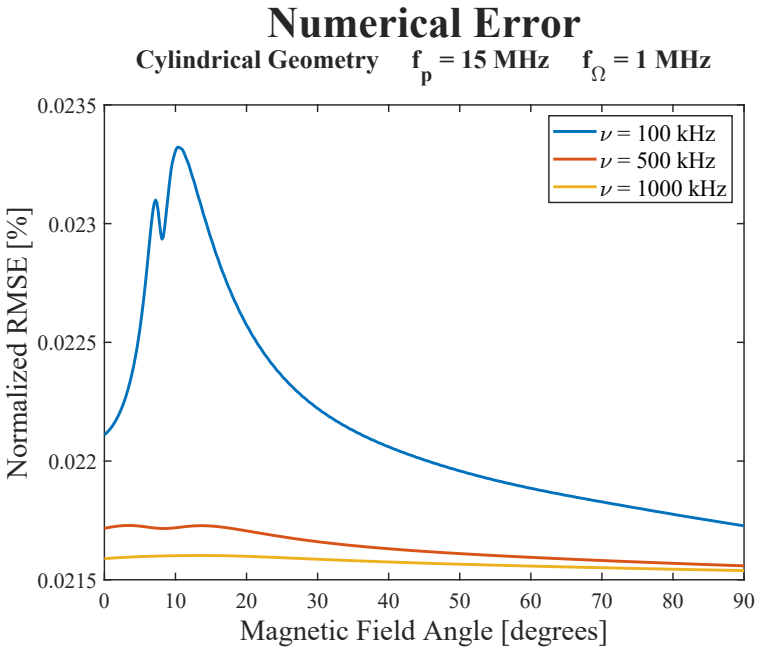

Fig. 3.3: Numerical error comparing various collision frequencies.

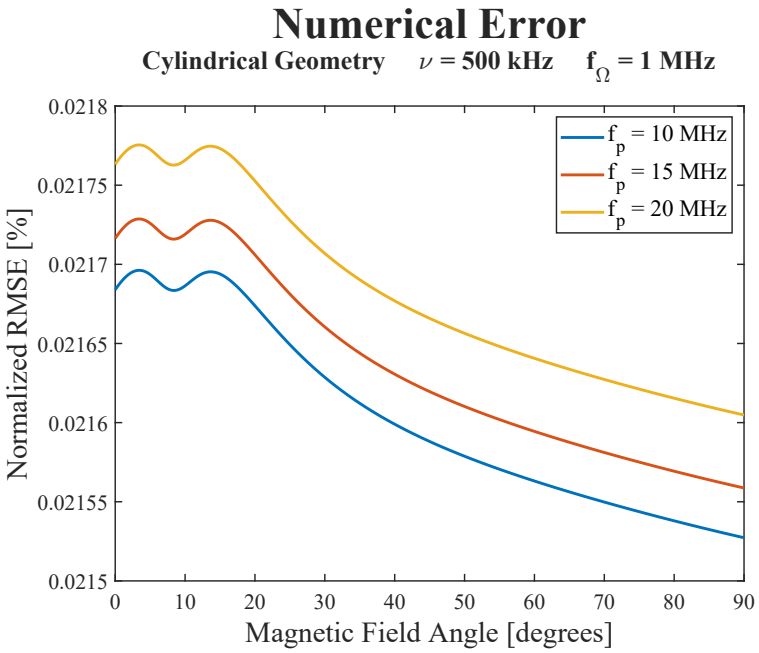

Fig. 3.4: Numerical error comparing various plasma frequencies.

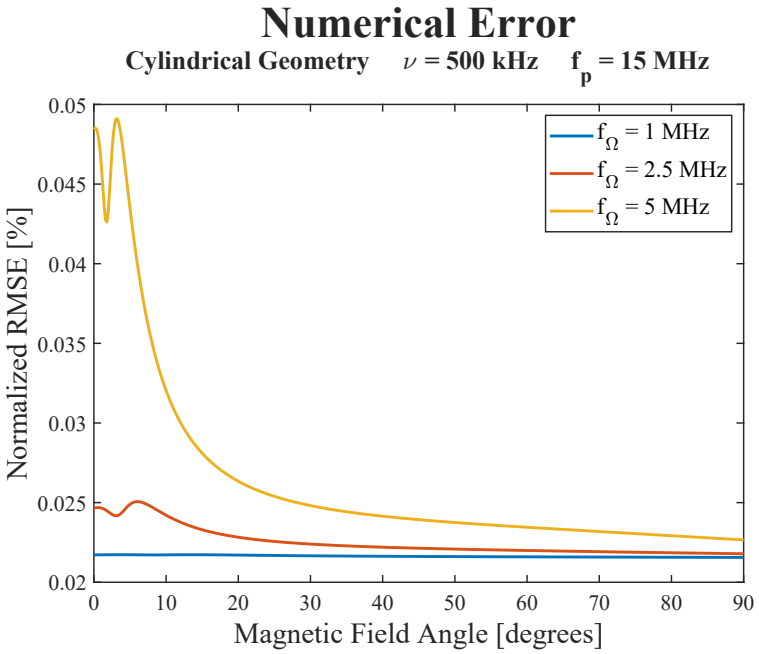

Fig. 3.5: Numerical error comparing various cyclotron frequencies.

Figures 3.3 - 3.5 show extremely minor error between the numerical solution and analytical expressions over a wide range of magnetic field angles and plasma parameters. This agreement between the two calculations provides confidence when using the numerical method to compute the impedance for more complex geometries and arbitrary magnetic field angles.

3.5 SPORT Geometry

After confirming agreement between the numerical solution and the analytical models for the simple geometries, the method is applied to the full SPORT spacecraft. A simplified SPORT spacecraft geometry is built in ANSYS Maxwell and the appropriate potentials are assigned. The numerical impedance is then computed using the simulated electric field. This result is compared to each analytical approximation using the NRMSE defined earlier. The analytical geometry that yields the smallest NRMSE is interpreted as the one that best represents the effective probe geometry on the SPORT spacecraft.

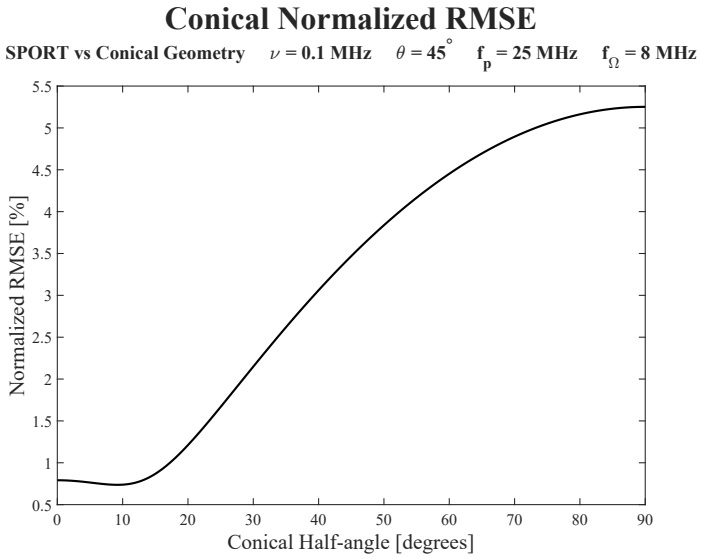

Fig. 3.6: Conical geometry mean squared error over conical half-angle.

Figure 3.6 shows the NRMSE for the conical and SPORT comparison. A conical half-angle of 9.19 degrees minimizes the error. The exact half-angle is slightly dependent

on frequencies ω_p, ω_c, and ν, but overall the geometry has a best-fit around 9 degrees. Figure 3.7 shows the SPORT and conical impedances, given the parameters under which the minimization was done.

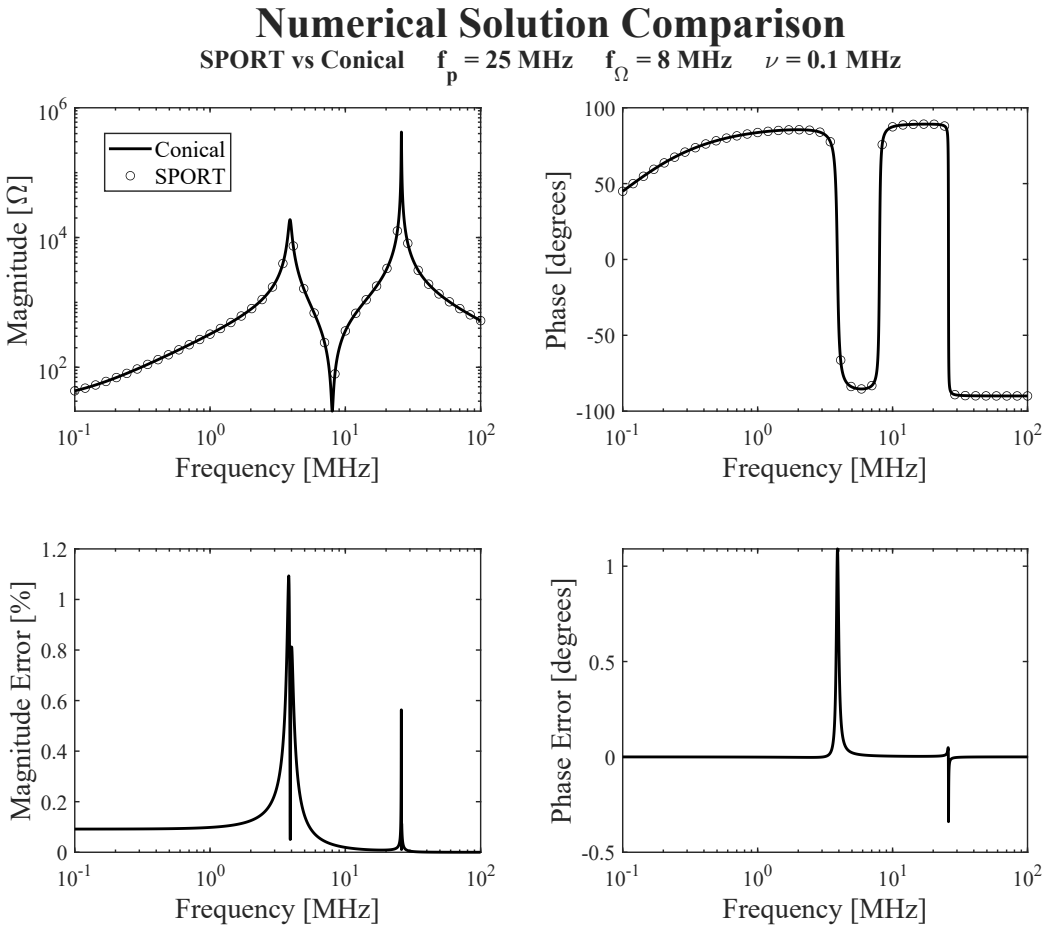

Fig. 3.7: Comparison of the analytical conical geometry to the numerically solved SPORT geometry.

Figure 3.7 shows a strong agreement between the conical and SPORT geometry. For reference, table 3.1 shows the normalized root mean squared error for the other simple geometries.

Table 3.1: SPORT geometry NRMSE for various simple geometries.

Geometry	NRMSE [%]
Plate	5.25
Sphere	2.64
Cylinder	0.79
Cone	0.74

The next best geometry choice is the cylindrical geometry. Using a cylindrical geometry is vastly easier mathematically than conical and sheath effects are more readily applied to such a geometry.

3.6 Summary

This chapter described the method used to obtain impedance from the electric-field data produced by ANSYS Maxwell. The numerical approach was first validated by comparing its results with analytical solutions for simple geometries. Once the method was validated, it was applied to the full SPORT spacecraft geometry. The resulting numerical impedance was then compared with analytical approximations to determine which simple geometry best represents the actual probe geometry.

Because of the close agreement, the method has validity and can be used for more complex geometries were an analytical solution is not possible. Using this method to solve for the plasma impedance aids to design of future probes as well as comparing real world measurement to theory because the space craft can be fully modeled in the ANSYS Maxwell environment. Doing so will include all fringing field effects that cannot be captured with simple geometric models.

CHAPTER 4

Plasma Sheath Analysis

In Section 2.1.3 the plasma sheath was approximated as a vacuum boundary surrounding the spacecraft and probe surfaces. This approximation can be represented as a layer of vacuum dielectric ϵ_0 placed in series with the plasma dielectric. In this chapter, the influence of the sheath on the impedance resonances is analyzed and compared with the SPORT measurements.

4.1 Simple Geometries with Added Sheath Layers

The effective capacitance of multiple dielectric layers in series is obtained by treating each layer as a capacitor and forming their series combination. From basic circuit theory, the capacitance of n capacitors in series is given by

$$\frac{1}{C_{\text{eq}}} = \sum_{i=1}^{n} \frac{1}{C_i}. \tag{4.1}$$

Building on the simple geometries, a vacuum sheath layer is added around the conductive bodies that form the capacitor. Figures 4.1 through 4.3 illustrate the plate, cylinder, and sphere geometries with the added vacuum sheath layer.

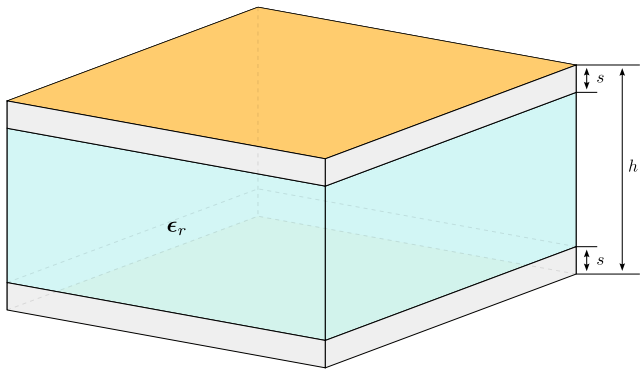

Fig. 4.1: Parallel plate geometry with added sheath layer.

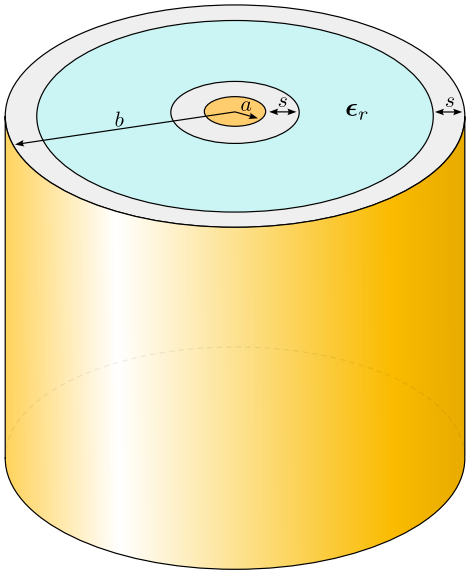

Fig. 4.2: Cylindrical geometry with added sheath layer.

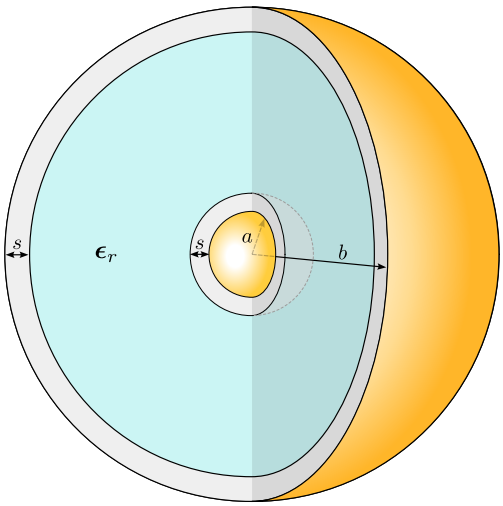

Fig. 4.3: Spherical geometry with added sheath layer.

For each geometry, the free-space capacitance is

$$C_{0,\text{plate}} = \epsilon_0 \frac{A}{d}, \qquad C_{0,\text{cylinder}} = \epsilon_0 \frac{2\pi L}{\ln\left(\frac{b}{a}\right)}, \qquad C_{0,\text{sphere}} = \epsilon_0 4\pi \left(\frac{ab}{b-a}\right). \tag{4.2}$$

The total capacitance of the system is found by adding the capacitance of each layer in series:

$$C = \frac{1}{\frac{1}{C_s} + \frac{1}{C_p} + \frac{1}{C_s}}. \tag{4.3}$$

Here, C_s is the sheath (vacuum) capacitance for the respective geometry, and C_p is the plasma capacitance given by

$$C_p = C_0 \epsilon_r \tag{4.4}$$

where ϵ_r is the scalar permittivity for each geometry from equations 2.21 – 2.23. The capacitance for the plate that includes a sheath layer is

$$C_{\text{plate}} = \epsilon_0 \frac{A}{h} \frac{\epsilon_r}{\epsilon_r - (1 - \frac{2s}{h})(\epsilon_r - 1)}. \tag{4.5}$$

The capacitance of the cylinder with a sheath layer is

$$C_{\text{cylinder}} = \epsilon_0 \frac{2\pi L}{\ln\left(\frac{b}{a}\right)} \frac{\epsilon_r}{\epsilon_r - \frac{\ln\left(\frac{b-s}{a+s}\right)}{\ln\left(\frac{b}{a}\right)}(\epsilon_r - 1)}. \tag{4.6}$$

The capacitance of the sphere with a sheath layer is

$$C_{\text{sphere}} = \epsilon_0 4\pi \left(\frac{ab}{b-a}\right) \frac{\epsilon_r}{\epsilon_r - \frac{b(b-a-2s)}{(b-a)(b-s)}(\epsilon_r - 1)}. \tag{4.7}$$

Expressions 4.5, 4.6, and 4.7 can be written as the product of three terms,

$$C = C_0 \epsilon_r K_s. \tag{4.8}$$

For a plasma capacitor without a sheath, the capacitance is simply $C_0 \epsilon_r$. Introducing a sheath adds the additional factor K_s, which is referred to as the correction factor. If $K_s = 1$, the expression reduces to the case without a sheath. If $K_s = 1/\epsilon_r$, the capacitance

reduces to the free-space value C_0. In general K_s is written as

$$K_s = \frac{1}{\epsilon_r - \alpha(\epsilon_r - 1)}, \tag{4.9}$$

where α is the geometric factor for the specific geometry of interest. The parameter α is bounded between 0 and 1, which properly scales K_s to be a value between $\frac{1}{\epsilon_r}$ and 1. The value of α depends only on the sheath thickness and the geometry.

For the three geometries considered here, the geometric factors are

$$\alpha_{\text{plate}} = 1 - \frac{2s}{h}, \qquad 0 \leq s \leq \frac{h}{2}, \tag{4.10}$$

$$\alpha_{\text{cylinder}} = \frac{\ln\left(\frac{b-s}{a+s}\right)}{\ln\left(\frac{b}{a}\right)}, \qquad 0 \leq s \leq \frac{b-a}{2}, \tag{4.11}$$

$$\alpha_{\text{sphere}} = \frac{b(b-a-2s)}{(b-a)(b-s)}, \qquad 0 \leq s \leq \frac{b-a}{2}. \tag{4.12}$$

Because $0 \leq \alpha \leq 1$ and is a dimensionless quantity, it can be interpreted as indicating the relative contribution of plasma compared to sheath within the capacitor volume. When $\alpha = 1$, the region within the capacitor is entirely filled with plasma. When $\alpha = 0$, the region is entirely filled with sheath (vacuum). Similarly, we can consider a sheath-to-plasma ratio, $\beta = 1 - \alpha$.

Below is a table, which summarizes the capacitance for the three geometries with included sheath effects.

Table 4.1: Probe capacitance with added sheath layer.

Probe Capacitance With Added Sheath			
$C = C_0 \epsilon_r K_s$		$K_s = \frac{1}{\epsilon_r - \alpha(\epsilon_r - 1)}$	
Geometry	**Vacuum Capacitance** (C_0)	**Permittivity** (ϵ_r)	**Geometric Factor** (α)
Planar	$\frac{\epsilon_0 A}{h}$	$\epsilon_1 \sin^2\theta + \epsilon_3 \cos^2\theta$	$1 - \frac{2s}{h}$
Cylindrical	$\frac{2\pi\epsilon_0 L}{\ln\left(\frac{b}{a}\right)}$	$\epsilon_1\left(1 + \cos^2\theta\right) + \epsilon_3 \sin^2\theta$	$\frac{\ln\left(\frac{b-s}{a+s}\right)}{\ln\left(\frac{b}{a}\right)}$
Spherical	$\epsilon_0 4\pi\left(\frac{ab}{b-a}\right)$	$\frac{2}{3}\epsilon_1 + \frac{1}{3}\epsilon_3$	$\frac{b(b-a-2s)}{(b-a)(b-s)}$

4.2 Effect on Plasma Resonances

In this section, the impedance from expressions in Table 4.1 is calculated and re-written into a rational form to clearly identify the poles and zeros of the function. These poles and zeros are what the impedance probe measures. The resonances are related to the dimensionless quantity α, and tested against measured data from the SPORT mission.

4.2.1 Impedance Resonance Locations

Using Table 4.1, the impedance magnitude for the plate geometry is calculated as

$$|Z| = \left|\frac{1}{j\omega C_0 \epsilon_r K_s}\right| = \frac{1}{\omega C_0}\left|\frac{\omega^4 - \omega^2(\Omega^2 + \beta\omega_p^2) + \beta\omega_p^2\Omega^2\cos^2\theta}{\omega^4 - \omega^2(\Omega^2 + \omega_p^2) + \Omega^2\omega_p^2\cos^2\theta}\right|. \tag{4.13}$$

The collision frequency ν is ignored in the following analysis given that the location of the resonances do not shift due to damping. The plasma-to-sheath ratio α is replaced with the sheath-to-plasma ratio β. Viewing the numerator and denominator as a quadratic in ω^2, the impedance magnitude is written as

$$|Z| = \frac{1}{\omega C_0}\left|\frac{(\omega^2 - z_+)(\omega^2 - z_-)}{(\omega^2 - p_+)(\omega^2 - p_-)}\right|. \tag{4.14}$$

with

$$z_{\pm} = \frac{\Omega^2 + \beta\omega_p^2 \pm \sqrt{(\Omega^2 + \beta\omega_p^2)^2 - 4\beta\Omega^2\omega_p^2\cos^2\theta}}{2} \tag{4.15}$$

and

$$p_{\pm} = \frac{\Omega^2 + \omega_p^2 \pm \sqrt{(\Omega^2 + \omega_p^2)^2 - 4\Omega^2\omega_p^2\cos^2\theta}}{2}. \tag{4.16}$$

This yields the observed resonance frequencies:

$$\omega_{\text{zero}\pm} = \sqrt{\frac{\Omega^2 + \beta\omega_p^2 \pm \sqrt{(\Omega^2 + \beta\omega_p^2)^2 - 4\beta\Omega^2\omega_p^2\cos^2\theta}}{2}} \tag{4.17}$$

and

$$\omega_{\text{pole}\pm} = \sqrt{\frac{\Omega^2 + \omega_p^2 \pm \sqrt{(\Omega^2 + \omega_p^2)^2 - 4\Omega^2\omega_p^2\cos^2\theta}}{2}}. \tag{4.18}$$

The resonances are shown below in Figure 4.4.

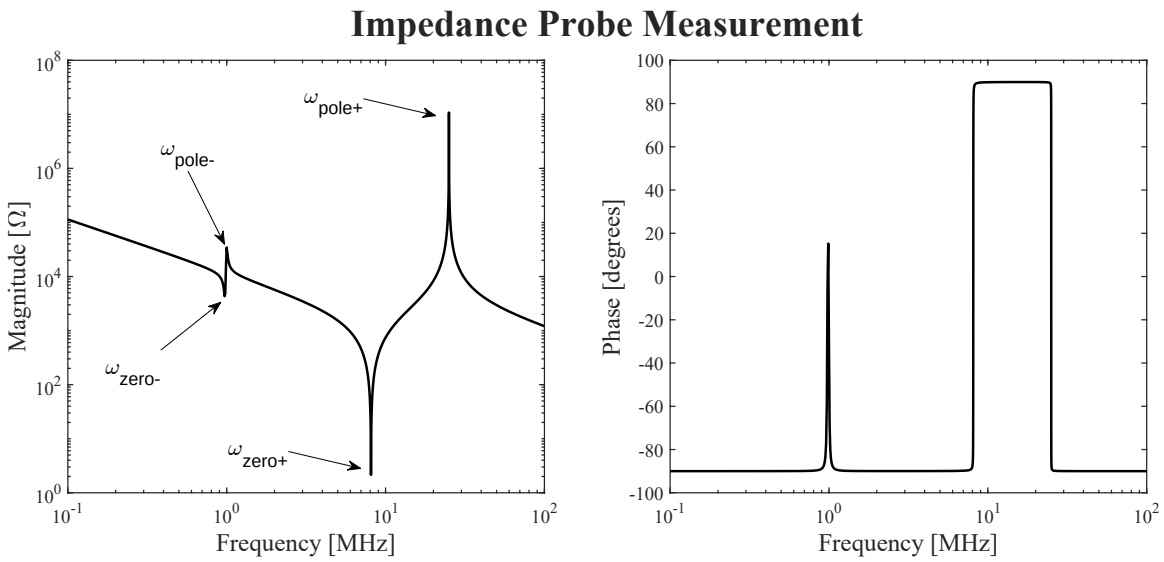

Fig. 4.4: Impedance for a parallel plate capacitor with addition of sheath layer.

In the context of an impedance probe, the resonances at $\omega_{\text{zero}+}$ and $\omega_{\text{pole}+}$ are the resonances of interest. These are relabeled as ω_{ser} and ω_{par}, respectively, for the series and parallel resonances. In a first-order sense, the plasma resonance can be thought of as a

parallel combination of an inductor and capacitor, hence the name parallel resonance. The sheath introduces an additional resonance, which can be modeled as adding an additional capacitance in series, hence the name series resonance. For a sweeping impedance probe such as the one used on SPORT, the frequency was swept from 2–30 MHz. This means the resonances located at $\omega_{\text{zero}-}$ and $\omega_{\text{pole}-}$ are typically outside of the measurement range.

The same process was repeated for the cylindrical and spherical geometries, with results shown below.

Cylindrical

$$\omega_{\text{zero}\pm} = \sqrt{\frac{\Omega^2 + \beta\omega_p^2 \pm \sqrt{(\Omega^2 + \beta\omega_p^2)^2 - 2\beta\Omega^2\omega_p^2 \sin^2\theta}}{2}} \tag{4.19}$$

$$\omega_{\text{pole}\pm} = \sqrt{\frac{\Omega^2 + \omega_p^2 \pm \sqrt{(\Omega^2 + \omega_p^2)^2 - 2\Omega^2\omega_p^2 \sin^2\theta}}{2}}. \tag{4.20}$$

Spherical

$$\omega_{\text{zero}\pm} = \sqrt{\frac{\Omega^2 + \beta\omega_p^2 \pm \sqrt{(\Omega^2 + \beta\omega_p^2)^2 - \frac{4}{3}\beta\Omega^2\omega_p^2}}{2}} \tag{4.21}$$

$$\omega_{\text{pole}\pm} = \sqrt{\frac{\Omega^2 + \omega_p^2 \pm \sqrt{(\Omega^2 + \omega_p^2)^2 - \frac{4}{3}\Omega^2\omega_p^2}}{2}} \tag{4.22}$$

4.2.2 Magnetic Field Effects

To see how the magnetic field angle θ impacts the impedance resonances at ω_{ser} and ω_{par}, the plate, cylindrical, and spherical resonances are solved for with $\theta = 0$ and $\theta = \pi/2$. This provides a bound on the shift in the impedance resonance locations.

For the plate capacitor and $\theta = 0$,

$$
\begin{aligned}
p_{\pm} &= \frac{\Omega^2 + \omega_p^2 \pm \sqrt{(\Omega^2 + \omega_p^2)^2 - 4\Omega^2\omega_p^2}}{2} \\
&= \frac{\Omega^2 + \omega_p^2 \pm |\Omega^2 - \omega_p^2|}{2} \\
&= \frac{\Omega^2 + \omega_p^2 \pm (\omega_p^2 - \Omega^2)}{2}
\end{aligned}
$$

where it is assumed that $\omega_p > \Omega$. This gives the pole roots as

$$p_+ = \Omega^2 \qquad p_- = \omega_p^2 \tag{4.23}$$

The zero roots are found to be

$$z_{\pm} = \frac{\Omega^2 + \alpha\omega_p^2 \pm \sqrt{(\Omega^2 + \beta\omega_p^2)^2 - 4\beta\Omega^2\omega_p^2}}{2} \tag{4.24}$$

$$= \frac{\Omega^2 + \beta\omega_p^2 \pm |\Omega^2 - \beta\omega_p^2|}{2} \tag{4.25}$$

where the assumption $\beta\omega_p^2 > \Omega^2$ cannot be made because $\beta \in [0, 1]$.

For $\Omega^2 > \beta\omega_p^2$,

$$z_+ = \frac{\Omega^2 + \beta\omega_p^2 + \Omega^2 - \beta\omega_p^2}{2} = \Omega^2 \tag{4.26}$$

$$z_- = \frac{\Omega^2 + \beta\omega_p^2 - \Omega^2 + \beta\omega_p^2}{2} = \beta\omega_p^2 \tag{4.27}$$

For $\beta\omega_p^2 > \Omega^2$,

$$z_+ = \frac{\Omega^2 + \beta\omega_p^2 + \beta\omega_p^2 - \Omega^2}{2} = \beta\omega_p^2 \tag{4.28}$$

$$z_- = \frac{\Omega^2 + \beta\omega_p^2 - \beta\omega_p^2 + \Omega^2}{2} = \Omega^2 \tag{4.29}$$

Thus

$$z_+ = \max(\Omega^2, \beta\omega_p^2) \qquad z_- = \min(\Omega^2, \beta\omega_p^2) \tag{4.30}$$

Note that for both cases $\Omega^2 > \beta\omega_p^2$ and $\Omega^2 < \beta\omega_p^2$ there is a pole cancellation for Ω, thus for both cases the impedance magnitude is reduced to

$$|Z|_{\theta=0} = \frac{1}{\omega C_0}\left|\frac{\omega^2 - \beta\omega_p^2}{\omega^2 - \omega_p^2}\right| \tag{4.31}$$

For $\theta = \frac{\pi}{2}$,

$$z_\pm = \frac{\Omega^2 + \beta\omega_p^2 \pm \sqrt{(\Omega^2 + \beta\omega_p^2)^2}}{2} \tag{4.32}$$

$$= \frac{\Omega^2 + \beta\omega_p^2 \pm (\Omega^2 + \beta\omega_p^2)}{2} \tag{4.33}$$

$$p_\pm = \frac{\Omega^2 + \omega_p^2 \pm \sqrt{(\Omega^2 + \omega_p^2)^2}}{2} \tag{4.34}$$

$$= \frac{\Omega^2 + \omega_p^2 \pm (\Omega^2 + \omega_p^2)}{2} \tag{4.35}$$

$$|Z|_{\theta=\frac{\pi}{2}} = \frac{1}{\omega C_0}\frac{\omega^2 - (\Omega^2 + \beta\omega_p^2)}{\omega^2 - (\Omega^2 + \omega_p^2)} \tag{4.36}$$

Thus the resonance locations are bounded by

$$\sqrt{\beta}\omega_p \leq \omega_{\text{ser}} \leq \sqrt{\Omega^2 + \beta\omega_p^2} \qquad \omega_p \leq \omega_{\text{par}} \leq \sqrt{\Omega^2 + \omega_p^2} \tag{4.37}$$

Repeating this process for the cylindrical and spherical geometry, a bound for resonances is found and summarized in the table below.

Table 4.2: Impedance series and parallel resonances bounds.

Impedance Series and Parallel Resonances		
Geometry	**Series Resonance**	**Parallel Resonance**
Planar	$\sqrt{\beta}\omega_p \leq \omega_{\text{ser}} \leq \sqrt{\Omega^2 + \beta\omega_p^2}$	$\omega_p \leq \omega_{\text{par}} \leq \sqrt{\Omega^2 + \omega_p^2}$
Cylindrical	$\sqrt{\frac{\Omega^2 + \beta\omega_p^2 + \sqrt{\Omega^4 + \beta^2\omega_p^4}}{2}} \leq \omega_{\text{ser}} \leq \sqrt{\Omega^2 + \beta\omega_p^2}$	$\sqrt{\frac{\Omega^2 + \omega_p^2 + \sqrt{\Omega^4 + \omega_p^4}}{2}} \leq \omega_{\text{par}} \leq \sqrt{\Omega^2 + \omega_p^2}$
Spherical	$\omega_{\text{ser}} = \sqrt{\frac{\Omega^2 + \beta\omega_p^2 + \sqrt{(\Omega^2 + \beta\omega_p^2)^2 - \frac{4}{3}\beta\Omega^2\omega_p^2}}{2}}$	$\omega_{\text{par}} = \sqrt{\frac{\Omega^2 + \omega_p^2 + \sqrt{(\Omega^2 + \omega_p^2)^2 - \frac{4}{3}\Omega^2\omega_p^2}}{2}}$

This analysis has revealed that the parallel resonance, which is used for electron density measurement, is not affected by the presence of a sheath in this vacuum boundary model. However, this parallel resonance is shifted due to magnetic field effects, which is geometry dependent. For the planar capacitor, the magnetic field can be perfectly orthogonal or perfectly parallel to the electric field, so the largest shift occurs. For the spherical capacitor, there is always complete symmetry, so no shift occurs. For the cylindrical capacitor, the magnetic field can be perfectly orthogonal to all electric field vectors but can never be perfectly parallel to all of them. This means the lower bound can never be exactly the plasma frequency like in the planar capacitor case.

In the context of impedance probe measurement, this implies that the magnetic field angle must be considered when inferring electron density, except in cases where perfect symmetry is present.

If we assume $\Omega < \omega_p$ and let $\gamma \in [0, 1]$, then the cyclotron resonance can be written as $\Omega = \gamma\omega_p$. In other words, the cyclotron resonance is some fraction of the plasma frequency. With this definition, the deviation in the parallel resonance due to magnetic field effects for the planar capacitor can be written as

$$\delta\omega_{\text{par}} = \sqrt{\gamma^2\omega_p^2 + \omega_p^2} - \omega_p \qquad \rightarrow \qquad \frac{\delta\omega_{\text{par}}}{\omega_p} = \sqrt{\gamma^2 + 1} - 1 \tag{4.38}$$

For the cylindrical capacitor, the normalized deviation in the parallel resonance is given by

$$\frac{\delta_{\text{par}}}{\omega_p} = \sqrt{\gamma^2 + 1} - \sqrt{\frac{\gamma^2 + 1 + \sqrt{\gamma^4 + 1}}{2}}. \tag{4.39}$$

For the spherical capacitor the deviation is always zero due to symmetry. In Figure 4.5, the deviation in the measurement due to magnetic field effects is compared between the plate and cylinder.

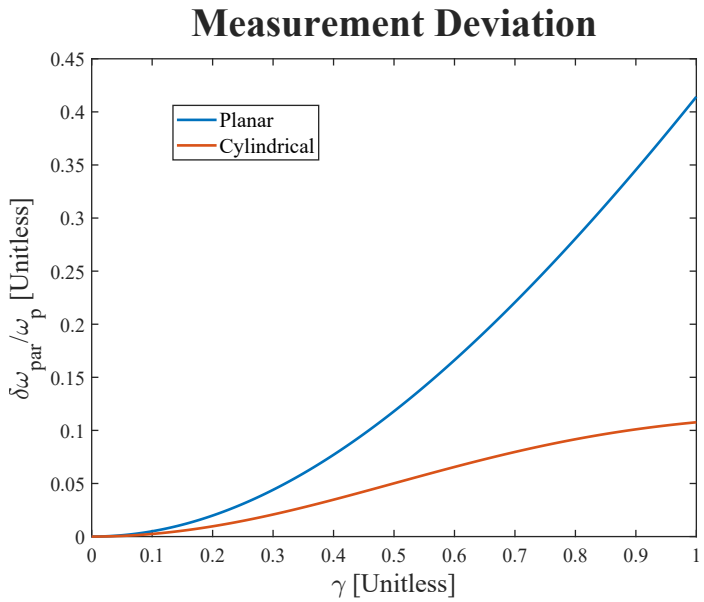

Fig. 4.5: Measurement deviation due to magnetic field effects.

As shown in Figure 4.5, the planar capacitor has the largest deviation, while the cylindrical capacitor has a smaller deviation. The purpose of comparing these geometries is to show that for plasma densities where $\Omega \ll \omega_p$, such as $0.01 \leq \gamma \leq 0.1$, the magnetic field angle has only a minor effect on the measured parallel resonance. As $\omega_p \to \Omega$, the magnetic field induces a larger deviation in the measurement, but not equally for all geometries.

4.2.3 Sheath Parameter Estimation

An estimation of the sheath-to-plasma parameter, β can be done by examining Table 4.2. For the spherical case, ω_p is readily solved

$$\omega_p^2 = \frac{3\omega_{\text{par}}^2(\omega_{\text{par}}^2 - \Omega^2)}{3\omega_{\text{par}}^2 - \Omega^2} \tag{4.40}$$

and β is solved,

$$\beta = \frac{3\omega_{\text{ser}}^2(\Omega^2 - \omega_{\text{ser}}^2)}{\omega_p^2(\Omega^2 - 3\omega_{\text{ser}}^2)}. \tag{4.41}$$

Substituting 4.40 into 4.41, β is solved for in terms of the measured quantities ω_{ser}, ω_{par}, and Ω as

$$\beta = \frac{\omega_{\text{ser}}^2(\Omega^2 - \omega_{\text{ser}}^2)(3\omega_{\text{par}}^2 - \Omega^2)}{\omega_{\text{par}}^2(\omega_{\text{par}}^2 - \Omega^2)(\Omega^2 - 3\omega_{\text{ser}}^2)} \tag{4.42}$$

For other geometries, estimating β is not as straightforward because the measurement deviates due to magnetic field effects. If we compare the maximum and minimum values for the plate, which should encompass the worse case scenario, then β can be bounded by

$$\frac{\omega_{\text{ser}}^2 - \Omega^2}{\omega_{\text{par}}^2 - \Omega^2} \leq \beta \leq \frac{\omega_{\text{ser}}^2}{\omega_{\text{par}}^2}. \tag{4.43}$$

4.3 Comparison to SPORT Data

4.3.1 Calculating the Plasma Frequency

The first step when comparing with the SPORT data is to establish a model that relates ω_{par} to the plasma frequency ω_p. Figure 4.6 shows how the measured frequency ω_{par} varies based on the geometry and magnetic field angle. The variation in ω_{par} is plotted with data obtained from the numerical method described in Chapter 3 with a magnetic field rotating in both the xz- and yz-plane. Additionally, various values for ω_{par} from Table 4.2 are plotted.

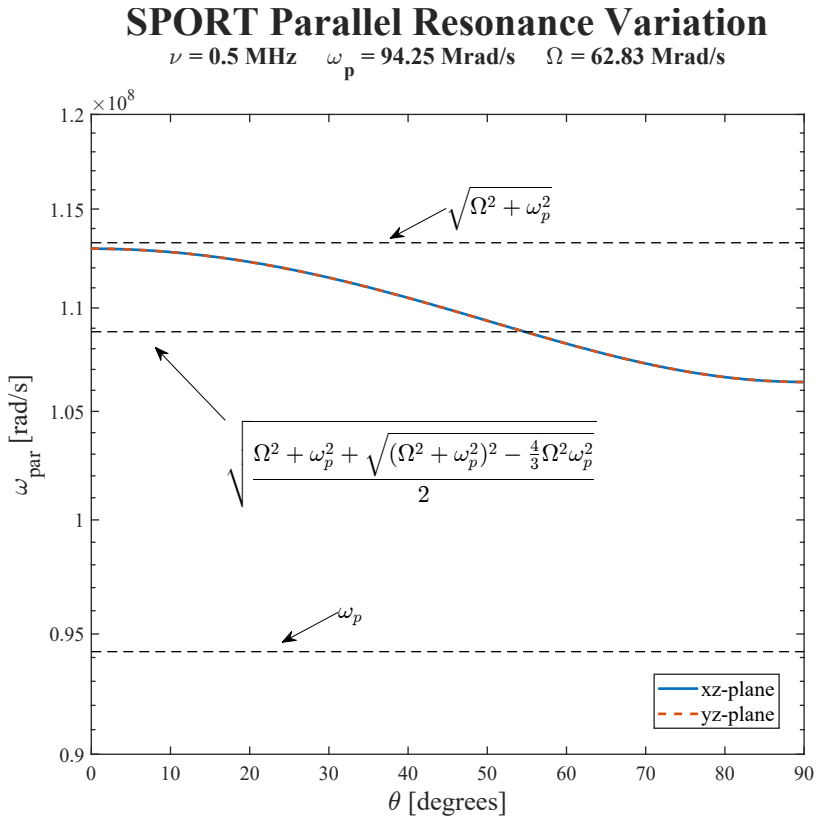

Fig. 4.6: SPORT parallel resonance variation

Figure 4.6 shows that if the cylindrical maximum for ω_{par} were used, then an overestimation of the plasma frequency occurs. If the spherical solution for ω_{par} were used, then either an overestimation or underestimation of the plasma frequency occurs, but the error is smaller for some θ. Therefore, an estimation that minimizes the error when calculating ω_p can be accomplished with the numerical model. If the magnetic field angle is known, then a best fit can be done to the blue and red-dashed curve shown in Figure 4.6, for this research it is assumed the magnetic field angle is not known, but the magnetic field amplitude is.

From equations 4.18, 4.20, and 4.22, the $\omega_{\text{pole+}}$ (or ω_{par}) frequency takes the form

$$\omega_{\text{par}} = \sqrt{\frac{\Omega^2 + \omega_p^2 + \sqrt{(\Omega^2 + \omega_p^2)^2 - k\Omega^2\omega_p^2 \sin^2\theta}}{2}} \tag{4.44}$$

where $k \in \mathbb{R}$ is a dimensionless quantity determined by the geometry. For the plate, $k = 4$,

for the cylinder, $k = 2$, and for the sphere $k = 4/3$. It is reasonable to assume that other geometries take on this structure, where the sin or cos term depends on the electric field direction and can always be exchanged under a change of variable. For the spherical case there is no dependency on θ. Equation 4.44 will be used as a general form to estimate the relationship between ω_{par} and ω_p using data obtained from the numerical method described in Chapter 3.

A value for k is found, which minimizes the squared error between the actual ω_{par} values found by simulation and the ω_{par} with an assumed k. Figure 4.7 shows the squared error in ω_{par} against k.

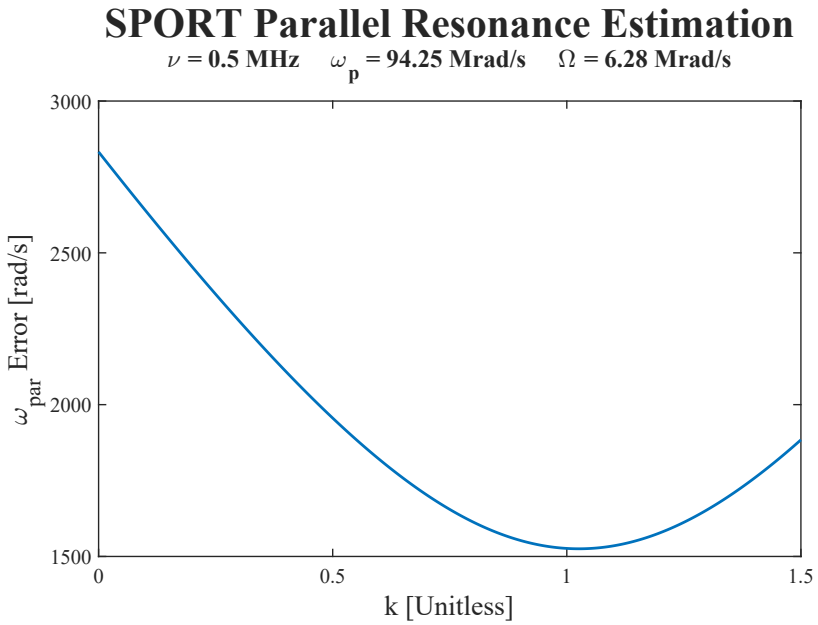

Fig. 4.7: Estimation of k for SPORT parallel resonance calculation.

As shown in Figure 4.7, the error is minimized for $k = 1.0257$. Figure 4.8 compares the numerical values of ω_{par} with the estimates obtained using this value of k, along with the corresponding error for realistic values of Ω and ω_p

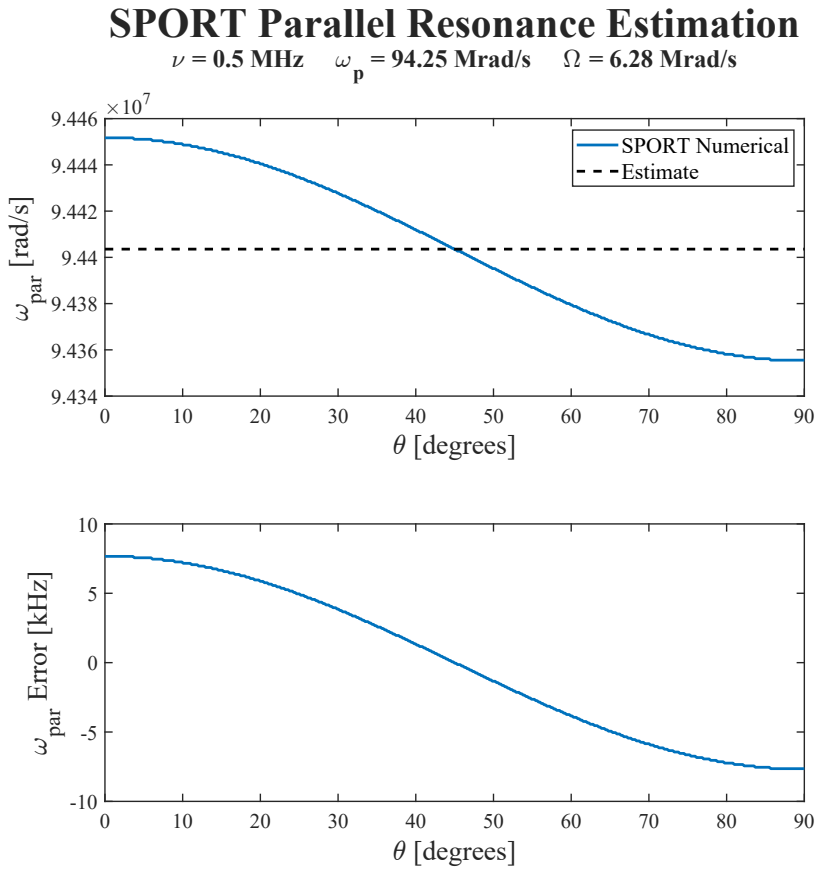

Fig. 4.8: Parallel resonance estimation error.

Figure 4.8 shows that the resulting error in the predicted ω_{par} is less than 10 kHz for $k = 1.0257$, which is several orders of magnitude smaller than the expected values of Ω and ω_p. As $\omega_p \to \Omega$, like in lower density plasma, the error will be higher. With this estimation for ω_{par}, the plasma frequency is given as

$$\omega_p = 2\omega_{\text{par}}\sqrt{\frac{\Omega^2 - \omega_{\text{par}}^2}{k\Omega^2 - 4\omega_{\text{par}}^2}}. \tag{4.45}$$

4.3.2 Processing SPORT Data

Processing the SPORT data follows the procedure outlined below.

1. Calculate impedance from the SPORT measurement.

The SPORT instrument records data as digital counts. These counts are converted to current using a set of calibration coefficients applied separately to the I and Q channels. Once the current is known, the impedance is obtained using the assumed applied voltage, which is measured during laboratory calibration.

$$I_I = \alpha_{1I} x_I + \alpha_{0I} \qquad I_Q = \alpha_{1Q} x_Q + \alpha_{0Q} \tag{4.46}$$

$$Z = \frac{V_{\text{mes}}}{I} \tag{4.47}$$

2. Calculate the cyclotron frequency Ω

   The magnetic field is required to determine the cylcotron frequency. Magnetic field values are obtained from the International Geomagnetic Reference Field (IGRF) model using the altitude, latitude, longitude, and date corresponding to each sweep. The cyclotron frequency is then computed from,

$$\Omega = \frac{e}{m_e} \vec{B_0}, \tag{4.48}$$

   where e is the elementary charge and m_e is the mass of the electron.

3. Calculate the plasma frequency ω_p

   The plasma frequency is calculated from the measured parallel resonance ω_{par} and cyclotron frequency Ω with use of 4.45.

4. Tune the collision frequency ν

   This model does not directly provide an estimate for the collision frequency. Instead, ν is adjusted manually for each sweep to obtain a good fit.

4.3.3 SPORT Data Comparison With Numerical Solution

Using the procedure outlined above, several plots are presented that compare the SPORT measurements with the numerical method described in Chapter 3. The numerical

model does not include sheath effects, which causes the lower resonance to disagree with the measurement. However, as shown earlier in this chapter, the parallel resonance is expected to be unaffected by sheath effects. Each plot includes the altitude of the spacecraft, the magnetic field strength obtained from the IGRF model, and the cyclotron, parallel, plasma, and collision frequencies (in MHz).

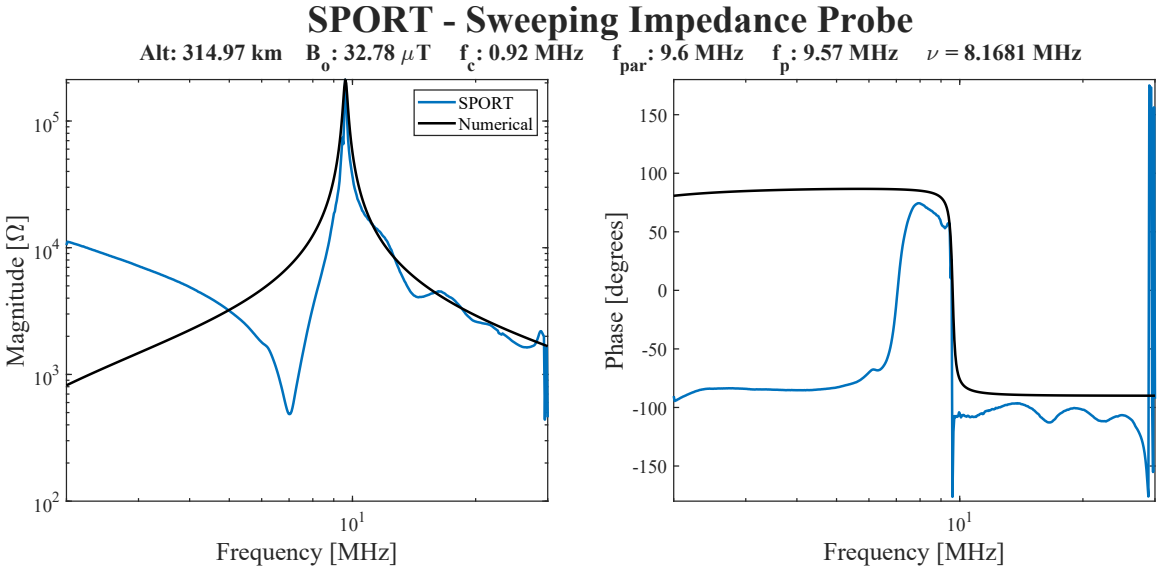

Fig. 4.9: SPORT Impedance Probe measurement with a large ω_p compared to Ω.

The first sweep of interest is shown in Figure 4.9. This sweep was selected because it satisfies the condition $\Omega \approx 0.1\omega_p$. Because $\Omega \ll \omega_p$, the parallel frequency is expected to be minimally effected by the magnetic field. As expected, the series resonance in the measurement does not match the numerical solution. However, the parallel resonance does match. The collision frequency ν required to match the peak amplitude is higher than expected. Figure 4.10 provides a zoomed-in view of the resonance, demonstrating a strong agreement in the resonant frequency.

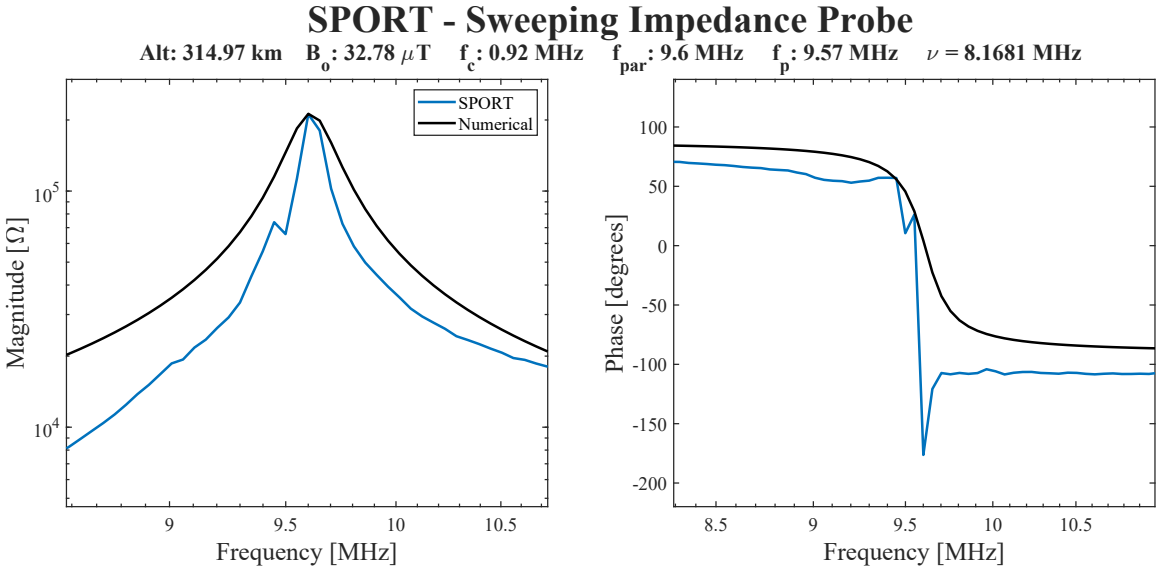

Fig. 4.10: Zoomed in view of SPORT Impedance Probe measurement with a large ω_p compared to Ω.

The second sweep of interest is shown in Figure 4.11. This sweep was chosen because the magnetic field was relatively strong and the plasma frequency was relatively low. Under these conditions, the parallel resonance in the measurement does not closely match the numerical prediction. This indicates that the magnetic field angle must be taken into account when determining the plasma frequency for cases with a strong magnetic field or low plasma densities. A zoomed-in view of the parallel resonance is shown in Figure 4.12.

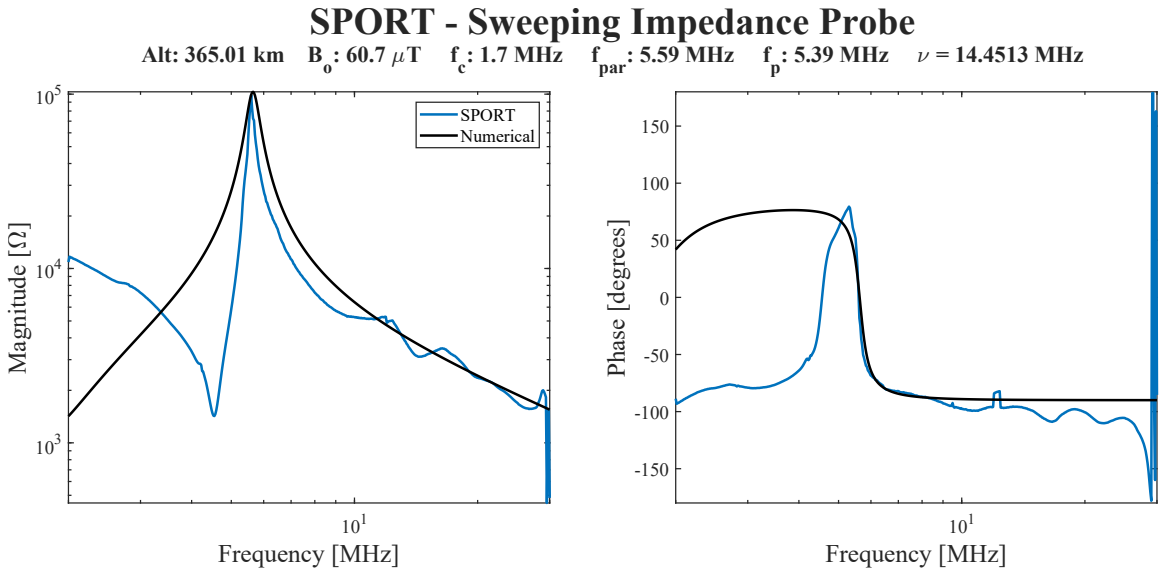

Fig. 4.11: SPORT Impedance Probe measurement with a small ω_p compared to Ω.

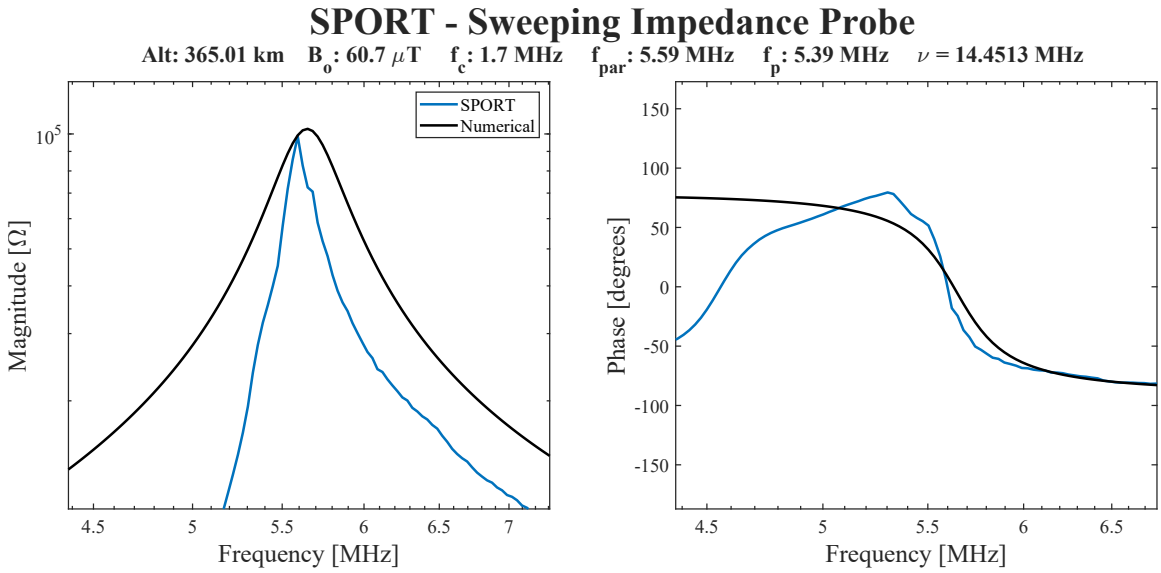

Fig. 4.12: Zoomed in view of SPORT Impedance Probe measurement with a small ω_p compared to Ω.

4.3.4 SPORT Data Comparison With Cylindrical Sheath Model

Both sweeps shown above are also compared to the cylindrical sheath model presented in 4.2. For this model, the plasma frequency is calculated using the cylindrical bounds

in Table 4.2. The plasma-to-sheath ratio β is calculated using 4.42, and the parameter α follows from $\alpha = 1 - \beta$. These values are substituted into the model presented in Table 4.1. As before, ν is tuned for each sweep separately by hand. Figure 4.13 shows the same sweep first presented in the last section.

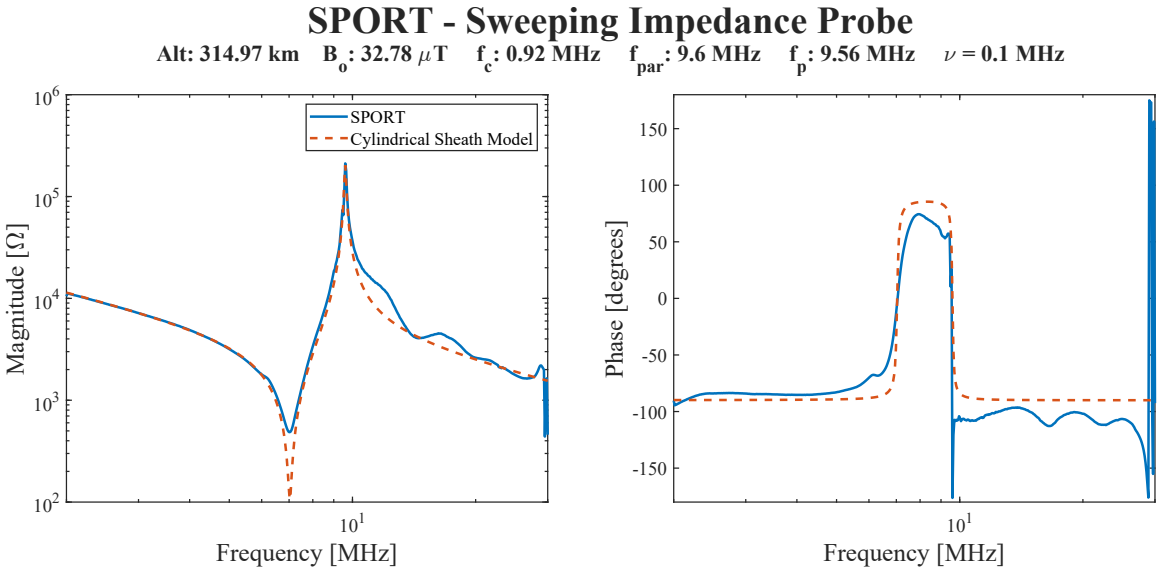

Fig. 4.13: SPORT measurement compared to cylindrical sheath model.

Figure 4.13 shows that the value of α calculated from the cylindrical sheath model presented in this chapter accurately predicts the location of the observed sheath resonance. Including sheath effects also changes the behavior of the collision frequency. Without sheath effects, the model required unrealistically large value of ν. When the sheath is included, the required collision frequency becomes more reasonable. A zoomed-in view of the parallel resonance for this sweep is shown in 4.14.

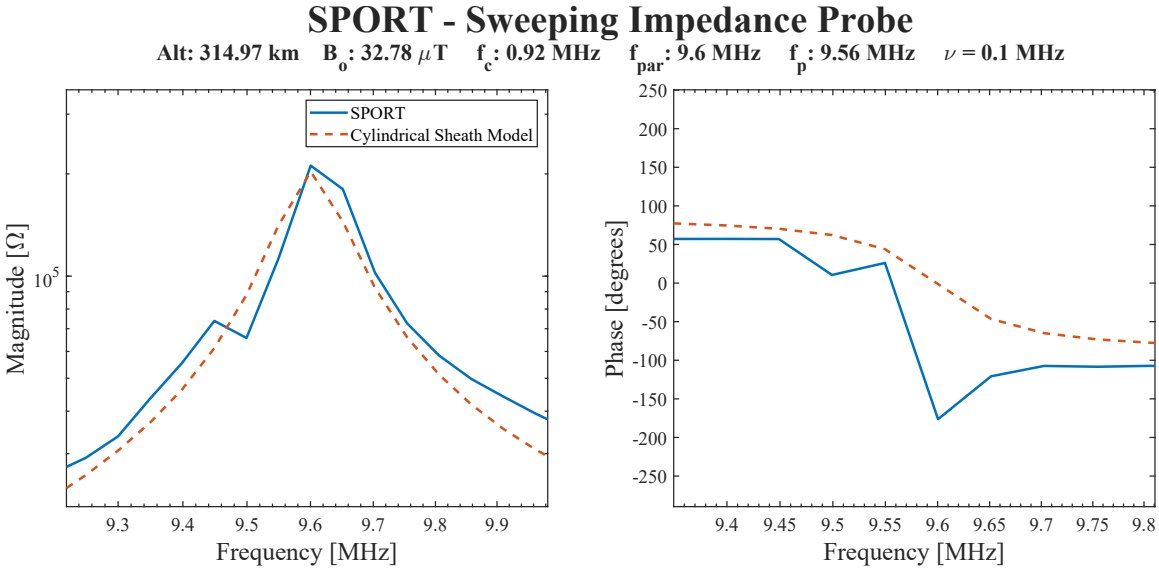

Fig. 4.14: Zoomed in SPORT measurement compared to cylindrical sheath model.

Figure 4.14 indicates that the calculated ω_p is slightly shifted relative to the measurement. This is expected because the SPORT probe geometry does not match the cylindrical geometry assumed in the model. Figure 4.15 compares the next sweep, which corresponds to the stronger magnetic field and less dense plasma.

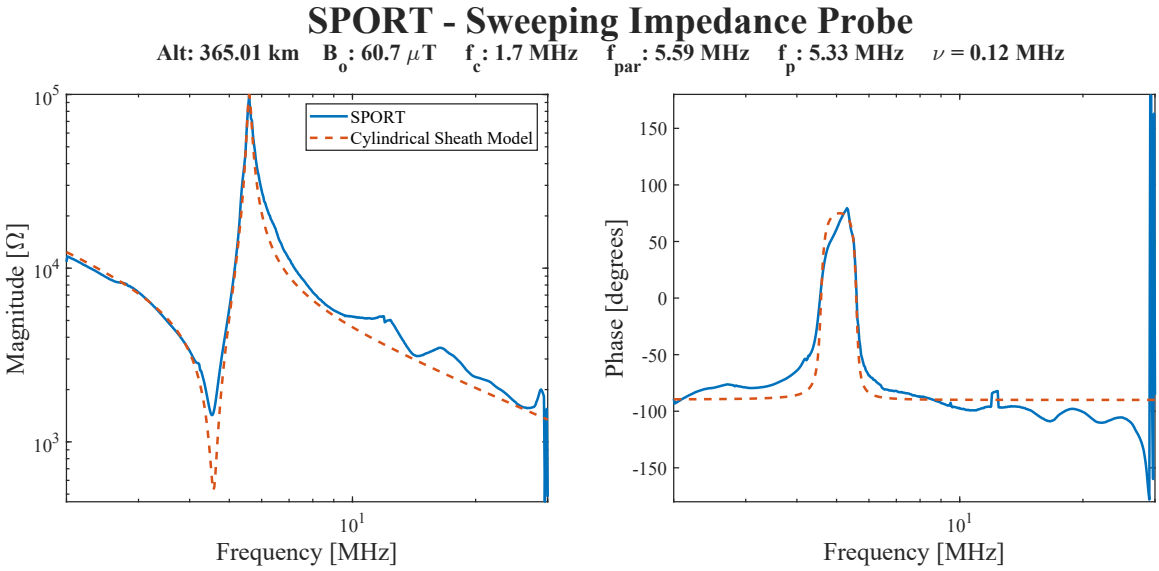

Fig. 4.15: SPORT measurement compared to cylindrical sheath model for small ω_p compared to Ω.

Figure 4.15 demonstrates that the sheath location derived from α remains consistent in the lower-density, high-magnetic-field case. The collision frequency also required less adjustment. Comparing Figures 4.9 and 4.11 shows that ν increased by 8 MHz, without sheath effects, whereas in the cylindrical sheath model the increase was only 20 kHz.

The source of the discrepancy in the amplitude of the lower resonance remains uncertain, although several possibilities exist. One explanation is that the fluid models used to derive the permittivity tensor do not include collisionless damping mechanisms such as Landau damping. Although Landau damping lies outside the scope of this thesis, including these effects could potentially reduce the amplitude mismatch.

Another source of error arises from the measurement technique. As discussed in Section 1.3.1, the SPORT impedance probe uses an I-V type topology. Unlike traditional I-V system, the voltage is not measured in flight but instead is obtained from pre-flight measurements. When the impedance drops to low values, like those around the sheath resonance, the voltage on the probe head is expected to drop due to loading effects. Because this drop in voltage is not measured in flight, the pre-flight measurements used in calibration would cause errors in the measurement, making the measured impedance appear to be larger.

4.4 Summary

In this chapter, the plasma sheath surrounding a spacecraft was modeled as a vacuum dielectric layer in series with the plasma dielectric. Analytical expressions were derived for planar, cylindrical, and spherical geometries, incorporating the sheath correction factor K_s and geometric parameter α which quantifies the relative sheath–to–plasma ratio. These formulations demonstrated how sheath thickness modifies the effective capacitance and the measured impedance.

By reformulating the impedance in rational form, the series and parallel resonances were identified. The analysis revealed that the sheath primarily introduces a lower-frequency series resonance while leaving the parallel resonance, associated with electron density, unaffected. Magnetic-field orientation was shown to shift resonance frequencies depending on geometry, with planar probes exhibiting the largest deviation and spherical probes the least.

Comparison with SPORT flight data confirmed that including sheath effects yields closer agreement with observed impedance. The model successfully captured both resonance locations and amplitude trends, indicating that a capacitive sheath approximation provides a practical and accurate first-order correction. Remaining discrepancies are likely due to unmodeled effects such as Landau damping or probe loading.

CHAPTER 5

Impedance Probe Circuitry

The impedance probe circuitry developed for the SPORT mission focused primarily on measuring the currents flowing through the plasma. Although this approach is sufficient for estimating the plasma frequency by tracking to the parallel resonance, a more accurate determination of the plasma impedance can be achieved by also measuring the voltage at the probe head. A more accurate measurement of the impedance over the entire frequency range would improve our understanding of the plasma. To provide a more accurate measurement of impedance, an auto-balancing bridge topology is utilized. In this research, a circuit board is designed to demonstrate the functionality of the auto-balancing bridge circuit for Impedance Probes.

5.1 Auto-balancing Bridge

As discussed in section 2.2, a typical controller used for the auto-balancing bridge is an op-amp in a trans-impedance amplifier configuration. A reminder of the circuit topology is shown below. The circuit board designed and built for this research follows this topology.

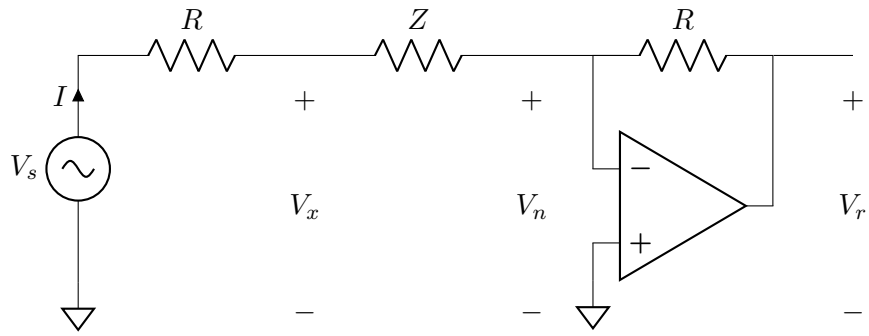

Fig. 5.1: Auto-balancing bridge implemented with a trans-impedance amplifier.

5.2 Instrument Sensitivity

An important parameter for the impedance probe is its sensitivity. Sensitivity describes how much the instrument's output changes in response to a change in the input. For this circuit, this corresponds to how the voltages V_x and V_r vary in response to a change in the impedance Z. The following sensitivity analysis assumes ideal components with the bridge balanced ($V_n = 0$). In this configuration, the sensitivity is set by the source and gain resistor R. A method for selecting an appropriate value of R is presented below.

The voltage V_x is simply a voltage divider between the drive resistor and the load:

$$V_x = V_s \frac{Z}{R+Z} \tag{5.1}$$

The voltage V_r is the voltage generated by the trans-impedance amplifier:

$$V_r = -IR = -V_s \frac{R}{R+Z} \tag{5.2}$$

Both expressions result in the same magnitude of sensitivity, given by

$$s = \left| \frac{dV_x}{dZ} \right| = \left| \frac{dV_r}{dZ} \right| = V_s \frac{R}{(R+Z)^2} \tag{5.3}$$

This expression shows that the instrument sensitivity depends on the impedance being measured, the source resistance, and the stimulus voltage. For this research, the stimulus voltage is assumed to be constant across the measurement band and is kept small enough to avoid nonlinear effects of the plasma. For this reason, a normalized sensitivity is used:

$$S = \frac{s}{V_s} = \frac{R}{(R+Z)^2}. \tag{5.4}$$

To choose a suitable value of R for a given application, the maximum average sensitivity over a specified impedance range is used:

$$R = \max\left\{\frac{1}{b-a}\int_a^b S\,dZ\right\} = \max\left\{\underbrace{\frac{R}{(a+R)(b+R)}}_{U}\right\}, \tag{5.5}$$

were it is assumed $R > 0$ and $b > a > 0$. a corresponds to the lowest expected measured impedance and b corresponds to the highest expected measured impedance. The function U is quasi-concave, thus a global maximum exists.

$$R = \max(U) \implies \frac{dU}{dR} = 0 \tag{5.6}$$

$$\frac{dU}{dR} = \frac{-R^2 + ab}{(a+R)^2(b+R)^2} = 0 \implies R = \sqrt{ab} \tag{5.7}$$

Thus, a reasonable initial choice for R is the geometric mean of the expected impedance bounds. One limitation of this approach is that if the lower bound a is zero, the result would be $R = 0$ regardless of the value of b. For spacecraft instrumentation, the expected impedance range is approximately 2 kΩ to 200 kΩ, making 20 kΩ a suitable initial value. This corresponds to an average sensitivity of $4.13\mu\text{V}/\Omega$. Figure 5.2 shows the sensitivity over a range of impedances for various source and gain resistors.

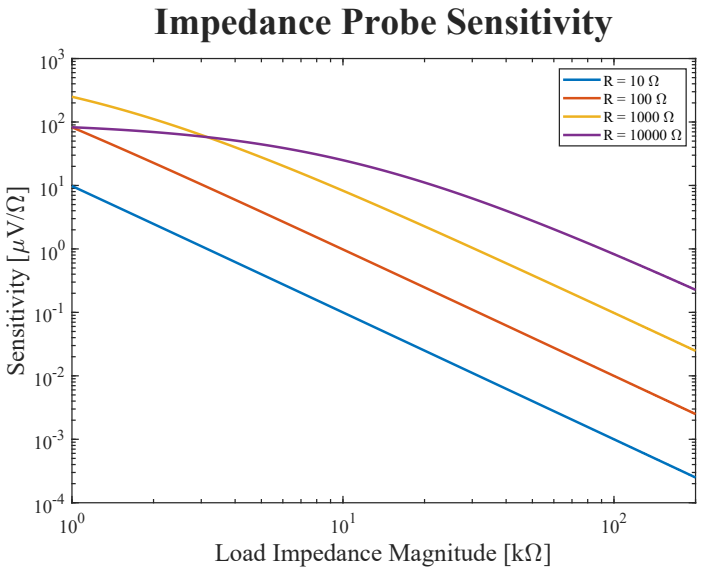

Fig. 5.2: Impedance probe sensitivity for the auto-balancing bridge.

5.3 Impedance Probe Testboard

A printed-circuit testboard was designed to demonstrate the auto-bridge operation for frequencies spanning from 1 – 30 MHz. This board includes four main functional blocks: the voltage stimulus generation, the transformer, the V_x/V_r sense circuitry, and a Field-programmable Gate Array (FPGA) for signal processing.

5.3.1 Voltage Stimulus Generation

The voltage stimulus is generated using a technique called Direct Digital Synthesis (DDS). In DDS, the bits that correspond to a sine wave are stored in a look-up table and a phase accumulator monotonically increments through this table. The phase accumulator increments by a specified value, which sets the output frequency given by

$$f_o = \frac{M f_c}{2^N} \tag{5.8}$$

where M is the accumulator value, f_c is the system clock frequency, and N is the bit width of the look-up table. In Simulink, this functionality is implemented using the built-in Numerically Controlled Oscillator (NCO) block. Frequency sweeps are produced by

updating the accumulator increment M for each desired output frequency.

The digital samples from the look-up table are sent to a digital-to-analog converter (DAC) across a parallel interface. The DAC used in this design is the AD9707, which is a 14-bit, low-power DAC. The DAC outputs a pair of complementary currents, which are converted to a single-ended voltage using an impedance-matched transformer. The schematic for the DAC is shown below in Figure 5.3.

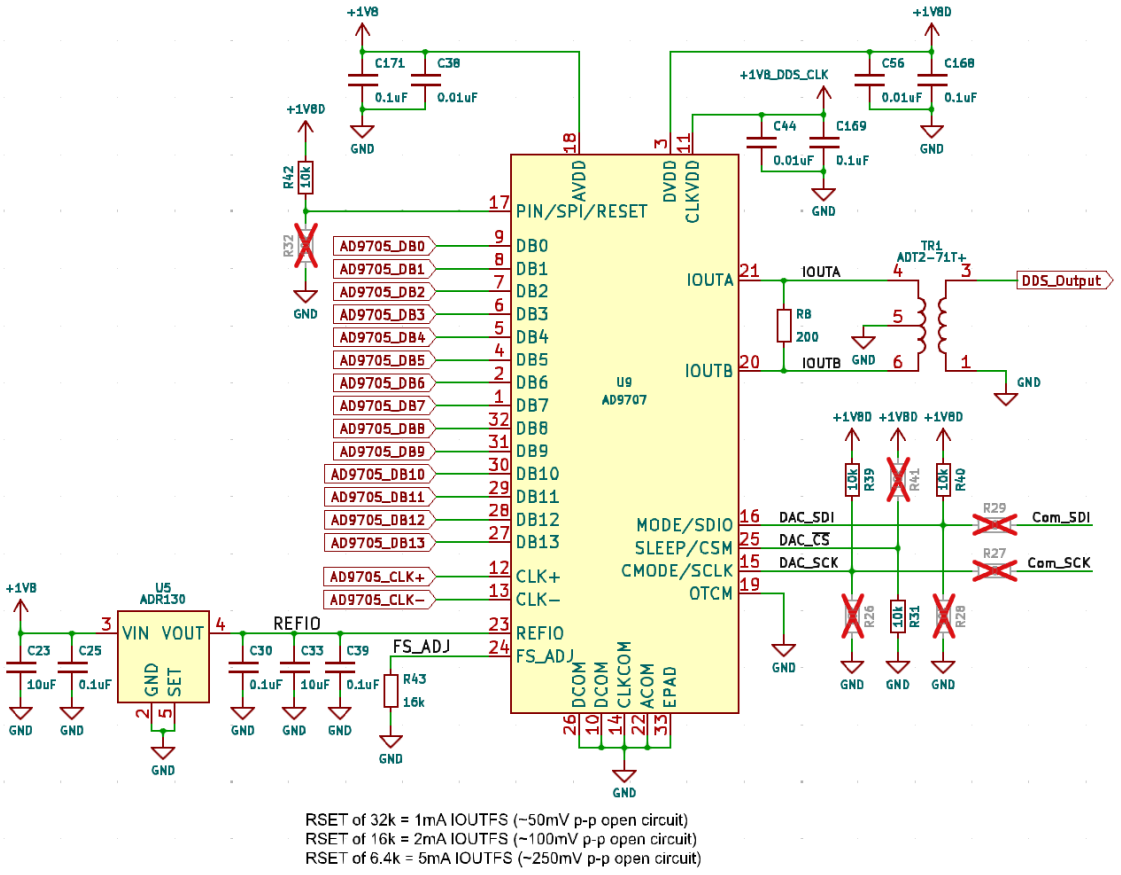

Fig. 5.3: AD9707 DAC schematics.

Because the DDS and DAC generate harmonics and aliases, the DAC output, labeled DDS_Output, is routed into a reconstruction filter. A 7^{th} order elliptic filter is chosen due to its sharp transition band. The implemented filter achieves 140 dB/decade roll-off. The topology for a 7^{th} order elliptic filter is shown below in Figure 5.4.

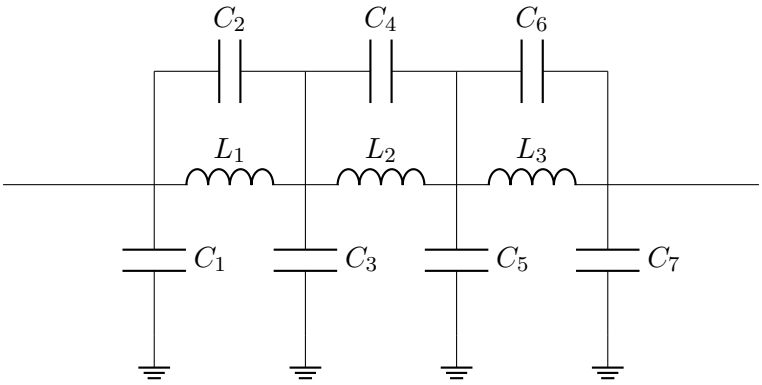

Fig. 5.4: Generic 7^{th} order elliptic filter.

To reduce unwanted series inductance and resistance in the shunt capacitors due to the components and vias, each shunt capacitor is implemented as two identical capacitors in parallel. Splitting the capacitors this way halves the individual equivalent series resistance (ESR) and equivalent series inductance (ESL), reducing their impact on the overall filter performance.

The filter was first designed and verified in LTSpice, including realistic parasitics obtained either from manufacturer-supplied models or estimated from impedance versus frequency plots. Figure 5.5 shows the LTSpice schematic used for the S_{21} simulation, and Figure 5.6 shows the measured frequency response obtained using a NanoVNA from 100 kHz to 100 MHz.

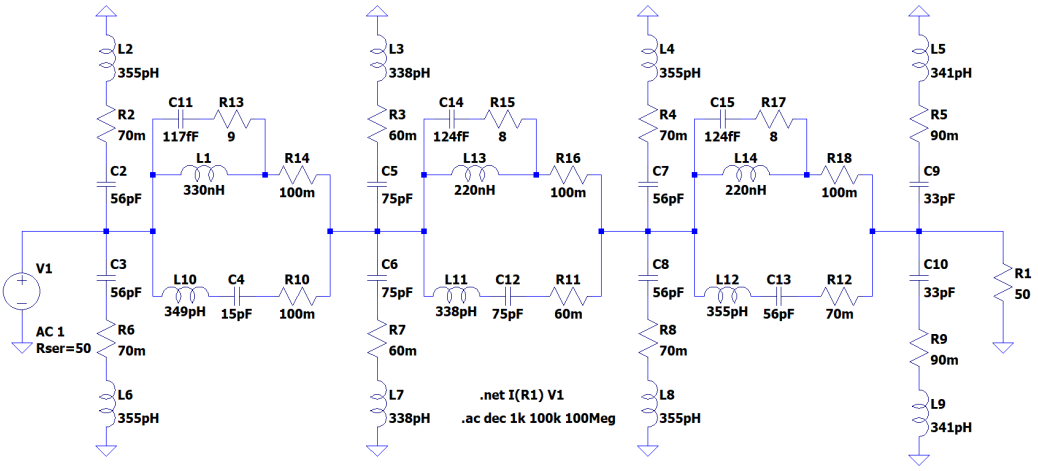

Fig. 5.5: Reconstruction filter simulation schematic

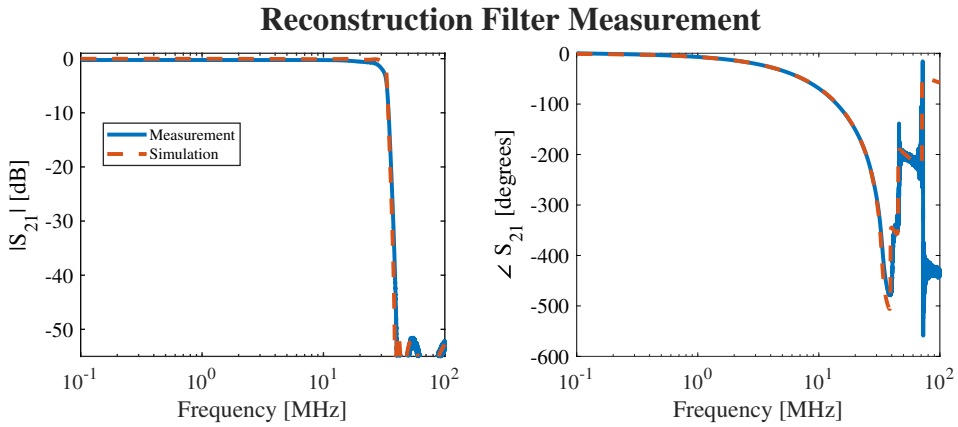

Fig. 5.6: Reconstruction filter measurement

The complete filtering and buffering stage schematics is shown in Figure 5.7. After filtering, the signal is terminated to 50 Ω and buffered to produce a signal that can drive the impedance probe head.

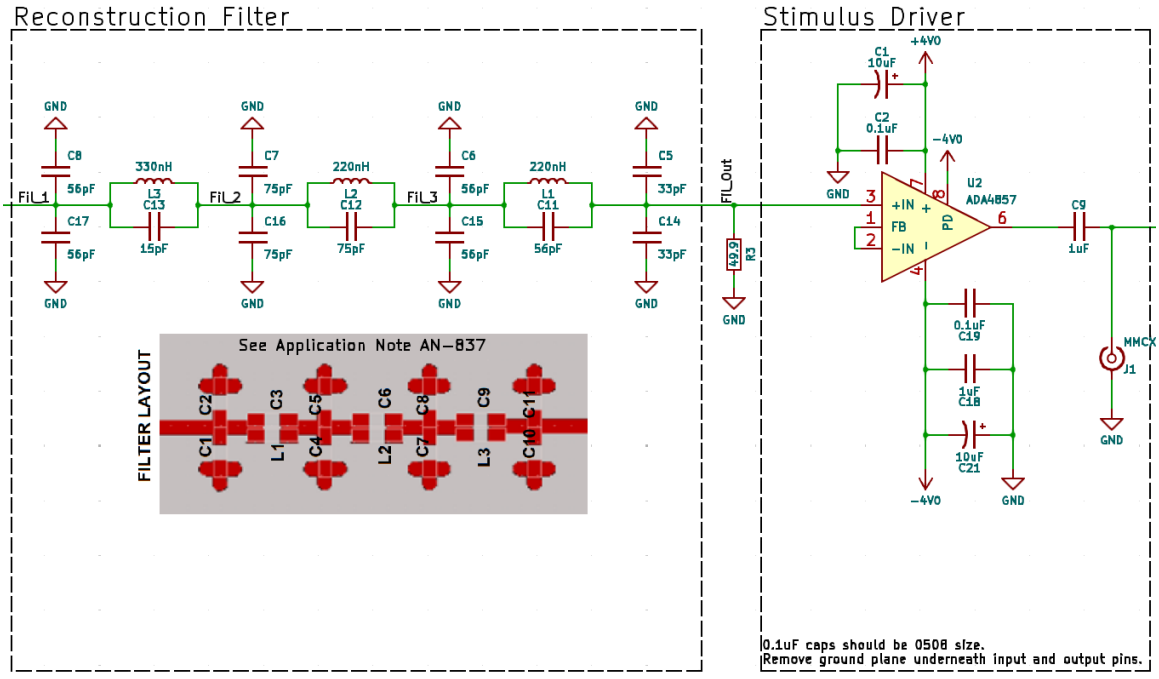

Fig. 5.7: Reconstruction filter schematic

5.3.2 Transformer

In section 2.2, the load impedance Z is shown as a series measurement directly in line with the sensing circuit. In applications such as spacecraft instrumentation, it is advantageous to insert a transformer between the sensing electronics and the load impedance. Figure 5.8 illustrates the same auto-balancing bridge topology introduced previously with the transformer included.

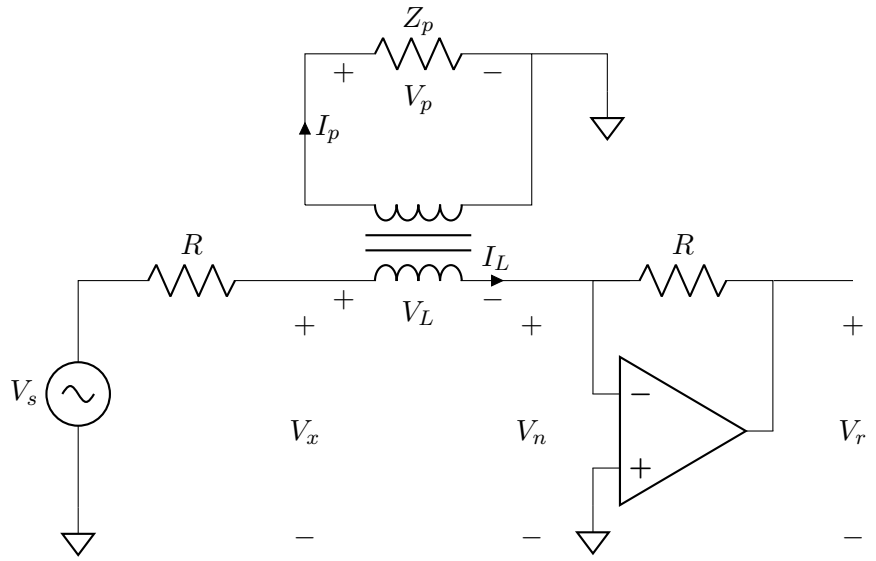

Fig. 5.8: Auto-balancing bridge topology with the added transformer.

The transformer introduced into the auto-balancing bridge circuit serves two primary purposes. First, it provides galvanic isolation, preventing plasma return currents from coupling directly into the measurement circuitry. Second, the transformer can apply a turns-ratio based scaling to the impedance. This impedance scaling can improve the bandwidth of the circuit.

Galvanic Isolation

As discussed in Section 2.2, the node V_n in the auto-balancing bridge must be actively driven to 0 V by the trans-impedance amplifier for the bridge to function properly. In spacecraft instrumentation, the circuit ground is typically tied to the spacecraft chassis. When the impedance probe is connected, the probe head is connected to V_x, while the spacecraft chassis reference is connected to V_n.

Without galvanic isolation, this configuration would place the chassis ground directly across the amplifier's input terminals, effectively short-circuiting the input stage and preventing the amplifier from operating. By inserting a transformer between the probe and the measurement circuit, the V_n node becomes electrically isolated from the spacecraft chas-

sis. This isolation allows the amplifier to maintain its virtual-ground condition at V_n and ensurers proper operation of the bridge.

Impedance Scaling

As discussed in Section 5.2, the optimized resistor R for a measurement impedance range from a to b with $b > a > 0$, is $\sqrt{ab}$. For example, if the measurement range of interest is 1 kΩ to 1 MΩ, the optimal resistor value is approximately 30 kΩ. For systems operating between 10 kHz and 100 kHz, this is acceptable. However, at frequencies above 10 MHz, several practical issues arise.

The primary limitation is that a resistor on a PCB exhibits parasitic capacitance to ground because of the component pads. This parasitic capcitance, together with the resistor, forms a low-pass filter that reduces the usable bandwidth of the circuit. As a reference, an 0402 resistor on a 100 μm thick FR-4 substrate exhibits around 200 fF of capacitance per pad. When combined with the op-amp output pad capacitance, the resulting low-pass cut-off frequency can fall within the measurement frequency range when using a high source resistance like 10 – 30 kΩ.

Additional parasitic elements such as trace capacitance and transformer winding capacitance create further leakage paths. To mitigate these effects, the transformer can be used to scale the impedance. By scaling the measured impedance down, the source and feedback resistors can also be reduced, lowering the impact of the parasitic capacitance's.

As an example, consider a 1-to-4 transformer. The reflected impedance is reduced by the square of the turns, resulting in the original measurement range of 1 kΩ – 1 MΩ being reduced to 62.5 Ω – 62.5 kΩ. The corresponding optimal resistor value becomes approximately 600 Ω. The 500 fF per resistor pad now has a cutoff frequency outside of the measurement range, extending the instrument bandwidth.

Transformer Construction

For this research, a multifilar-wound transformer using a toroidal core was selected. Toroidal cores are advantageous because their geometry supports winding techniques that

reduce leakage inductance and stray capacitance, extending the transformer's bandwidth.

The specific core used is a Fair-Rite toroid with an outer diameter of 13.45 mm. The core material is type 43, which has an inductance factor of 480 nH per turn squared. Using this value, a 10-turn winding is expected to yield roughly 48 µH of inductance, sufficient for operation near 1 MHz.

To implement multiple windings in a bifilar configuration, the wires for the higher-turn side of the transformer are first arranged in parallel. This set of parallel wires is then twisted around the primary winding, creating a twisted pair. This twisted pair is wrapped around the toroid, maximizing the distance between each winding to minimize the interwinding capacitance. Figure 5.9 shows the completed transformer with a 1-to-4 turns ratio.

Fig. 5.9: 4-to-1 transformer construction.

5.3.3 Sense Circuitry

Two voltages must be measured in order to determine the load impedance: the V_x and

V_r signals shown in 5.8. The sense circuitry measures these voltages, applies filtering, and delivers the signals to the analog-to-digital converter (ADC).

As described in section 2.2, the V_r voltage is generated using a trans-impedance amplifier, which produces a voltage proportional to the input current. A limitation of using a TIA as the controller is the reduced open-loop gain of the op-amp at frequencies above 100 kHz. To address this limitation, an uncompensated op-amp is selected to maximize open-loop gain. Because uncompensated op-amps are inherently unstable, a compensation network is included to ensure stability.

The TIA output is routed directly into a pre-amplifier stage with a gain of 19. After pre-amplification, the signal enters the ADC driver stage. This amplifier provides the current needed to drive the ADC input capacitors while maintaining stability. The ADC driver also functions as an anti-aliasing low-pass filter with a 40 MHz cutoff frequency, equal to half the sample clock. A Sallen-Key topology is used for the filter. Figure 5.10 shows the schematic of the V_r signal chain.

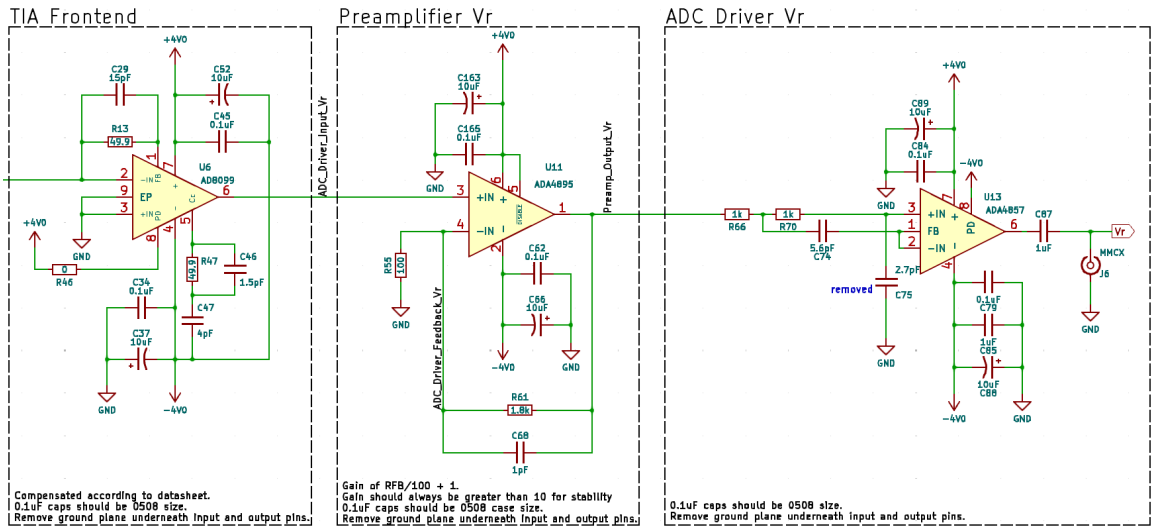

Fig. 5.10: V_r sense stage schematic.

The V_x signal chain has the same components as the V_r chain, but without the transimpedance amplifier because the voltage is sensed directly on the positive side of the transformer. The schematic for the V_x circuitry is shown in Figure 5.11.

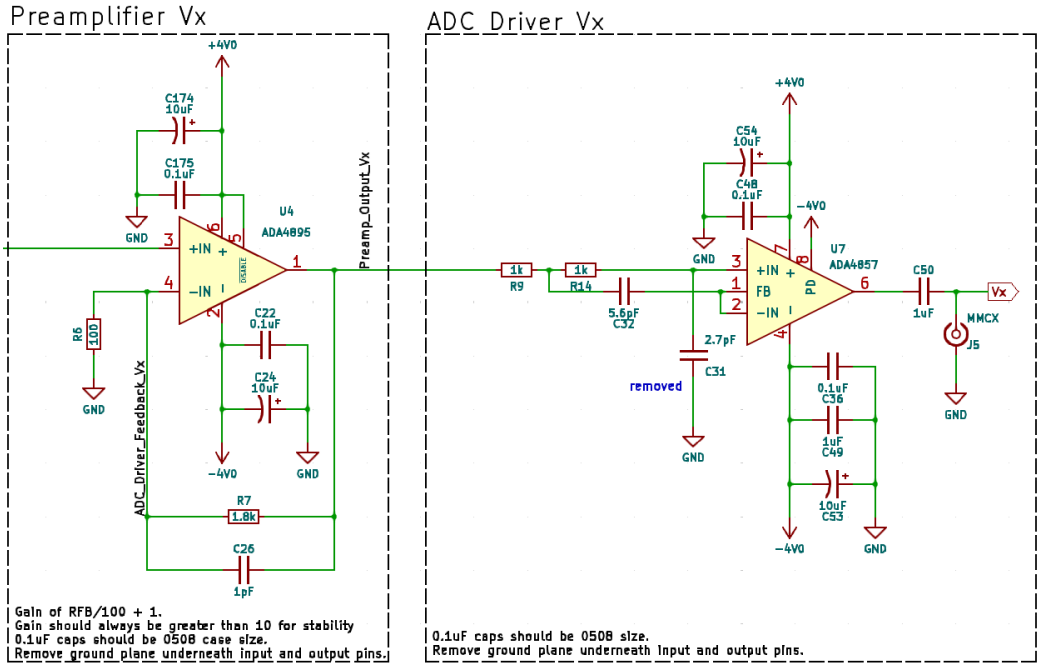

Fig. 5.11: V_x sense stage schematic.

The voltages V_x and V_r create a complementary pair. When the load impedance is a short circuit, the voltage V_x is a minimum and the voltage V_r is a maximum. When the load impedance is an open circuit, the voltage V_x is a maximum and the voltage V_r is a minimum. When the load impedance matches the source and gain resistor, then $V_x = V_r$. The maximum voltage expected from the circuit is the drive voltage, gained by the preamplifier.

The V_r generation and sense chain is simulated in LTSpice to confirm its expected performance. Figure 5.12 shows the simulation schematic. For this test, the load is short-circuited to ensure that the ADC driver output does not exceed 1 V. The simulation result is shown in Figure 5.13.

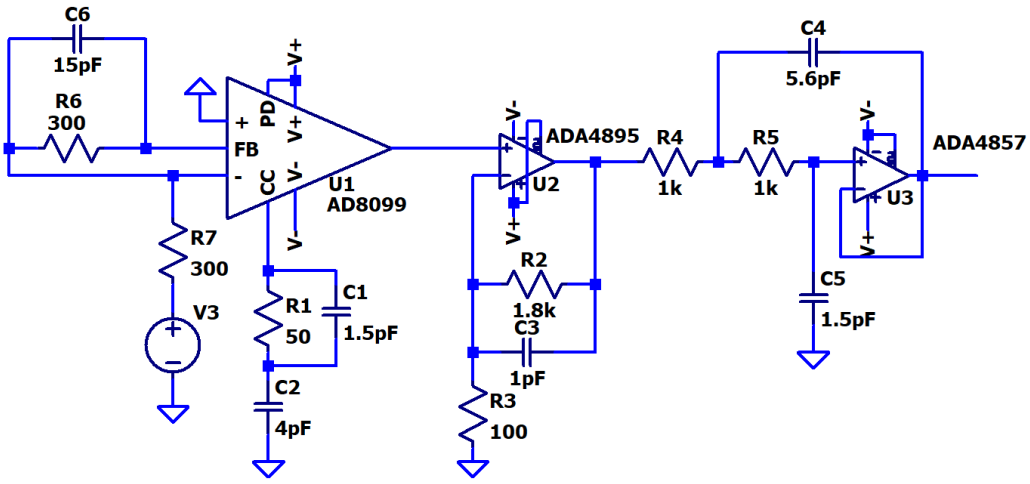

Fig. 5.12: Simulation schematic for V_r sense chain.

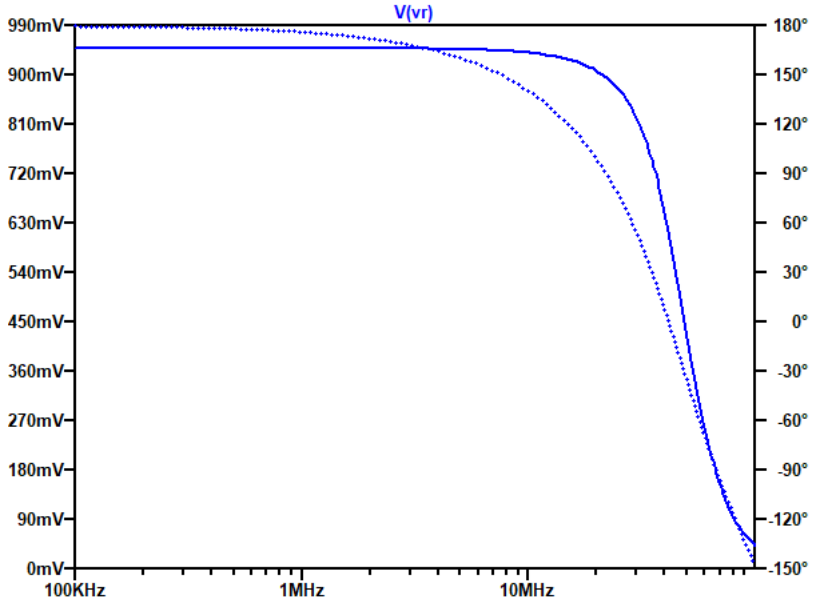

Fig. 5.13: Simulation result for V_r sense chain.

Following the ADC Driver, the V_x and V_r signals each go to an ADC, where they are digitized for processing by the FPGA. The ADC schematic is shown in Figure 5.14.

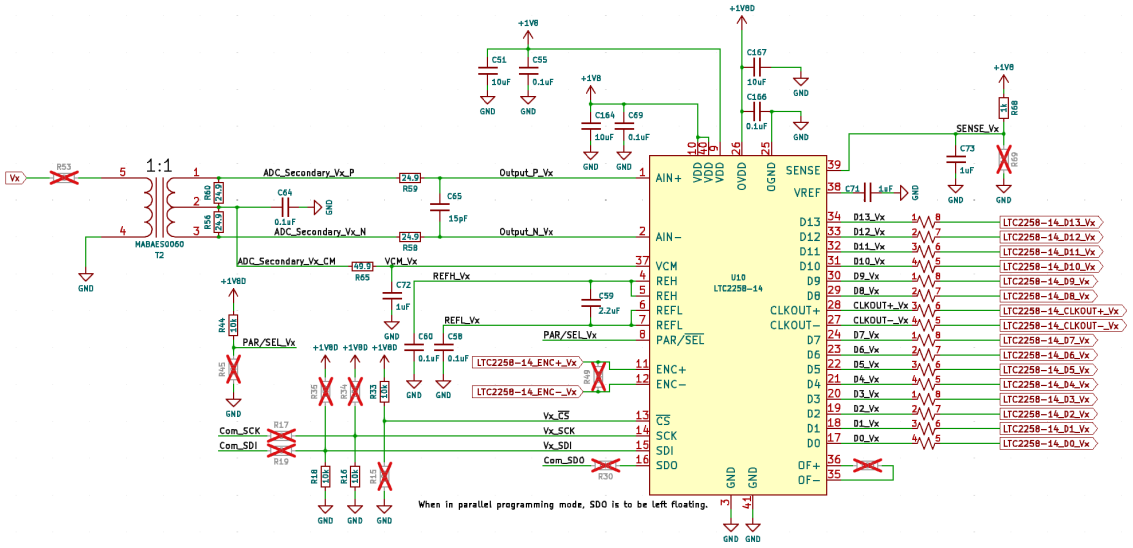

Fig. 5.14: LTC2259-14 ADC schematic.

5.3.4 FPGA

The FPGA used on the Impedance Probe Testboard is the IGLOO V2. To generate HDL code, the Simulink environment is used with HDL Coder. The two primary functions of the FPGA are the mixing and averaging stage and the data handling stage. Figure 5.15 shows a view of the full Simulink model.

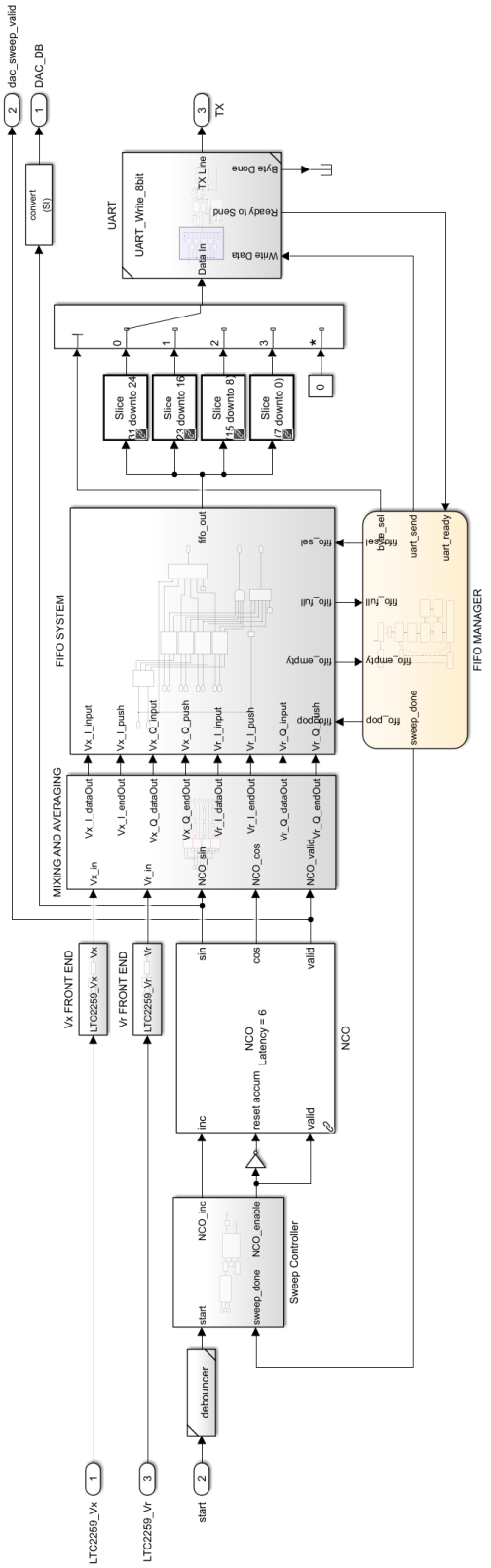

Fig. 5.15: Full simulink model for the Impedance Probe Testboard.

5.3.5 Mixing and Averaging

Both the amplitude and phase for voltages V_x and V_r must be measured to calculate Z_m. To do this, the method of I-Q Mixing is implemented. A sinusoid given by

$$x(t) = A\cos(\omega t + \phi) \tag{5.9}$$

can be recovered by mixing with a sinusoid of equal phase and $\pm 90^\circ$ phase.

$$Q(t) = A\cos(\omega t + \phi)\sin(\omega t) = \frac{A}{2}\big(\sin(2\omega t + \phi) - \sin(\phi)\big) \tag{5.10}$$

$$I(t) = A\cos(\omega t + \phi)\cos(\omega t) = \frac{A}{2}\big(\cos(2\omega t + \phi) + \cos(\omega t)\big) \tag{5.11}$$

After mixing, the signal now contains a DC component and frequency component that is twice the original frequency. Applying an averaging (low-pass) filter, the doubled frequency component can be mostly eliminated, with some error.

$$\langle Q[n]\rangle = \underbrace{\frac{A}{2N}\sum_{n=1}^{N}\sin(2\omega T_s n + \phi)}_{\text{error}} \underbrace{-\frac{A}{2}\sin(\phi)}_{\text{ideal}} \tag{5.12}$$

$$\langle I[n]\rangle = \underbrace{\frac{A}{2N}\sum_{n=1}^{N}\cos(2\omega T_s n + \phi)}_{\text{error}} + \underbrace{\frac{A}{2}\cos(\phi)}_{\text{ideal}} \tag{5.13}$$

Because the error term is a sinusoid, and divided by N samples taken, the error is small compared to the ideal value. The error term here is ignore, as it is assumed to be small. The unknown amplitude and phase are given by:

$$x(t) = 2\sqrt{I^2 + Q^2}\cos\left(\omega t - \arctan\left(\frac{Q}{I}\right)\right). \tag{5.14}$$

The mixing and averaging section on the FPGA performs the mathematics discussed

above. Figure 5.16 shows the Simulink model for the mixing and averaging section on the FPGA.

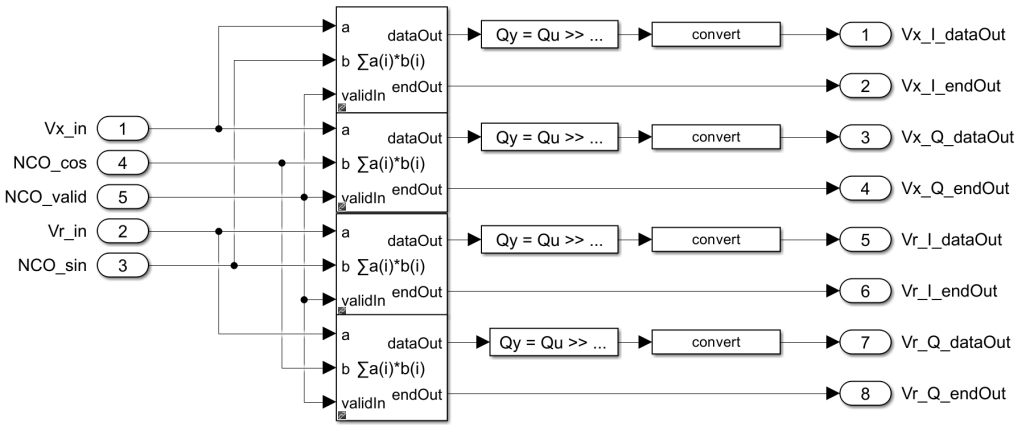

Fig. 5.16: Mixing and averaging simulink model.

The signals Vx_in and Vr_in are the sampled signals produced from each ADC. These samples go into the accumulate and multiply Simulink blocks, which compute the in-phase and quadrature components by multiplying each sample by either NCO_cos or NCO_sin, depending on whether the block corresponds to the I or Q channel. Each block accumulates N samples before producing an output, which is signaled by the endOut port on the multiply and accumulate block.

Once the accumulation is complete, the result is right bit-shifted by $\log_2(N)$. For this research, N is constrained to be a power of two, so $\log_2(N)$ is an integer. A right shift by $\log_2(N)$ performs a division by N, giving the averaged value.

The averaged signal is then converted to a 32-bit value by truncating the lower bits. These truncated bits correspond to accumulated noise and do not affect the final measurement.

5.3.6 Data Handling

The FPGA manages data storage using a set of first-in, first-out (FIFO) blocks that hold the I and Q components of both V_x and V_r, as shown in Figure 5.17.

The mixing and averaging block writes an I and Q pair into the FIFO blocks once N samples have been accumulated and averaged. This process is repeated for every frequency point in the sweep. When the final frequency step is complete, the fifo_full signal asserts, which triggers a state machine to pop values out of each FIFO and send them over a Universal Asynchronous Receiver/Transmitter (UART) bus to be processed in MATLAB.

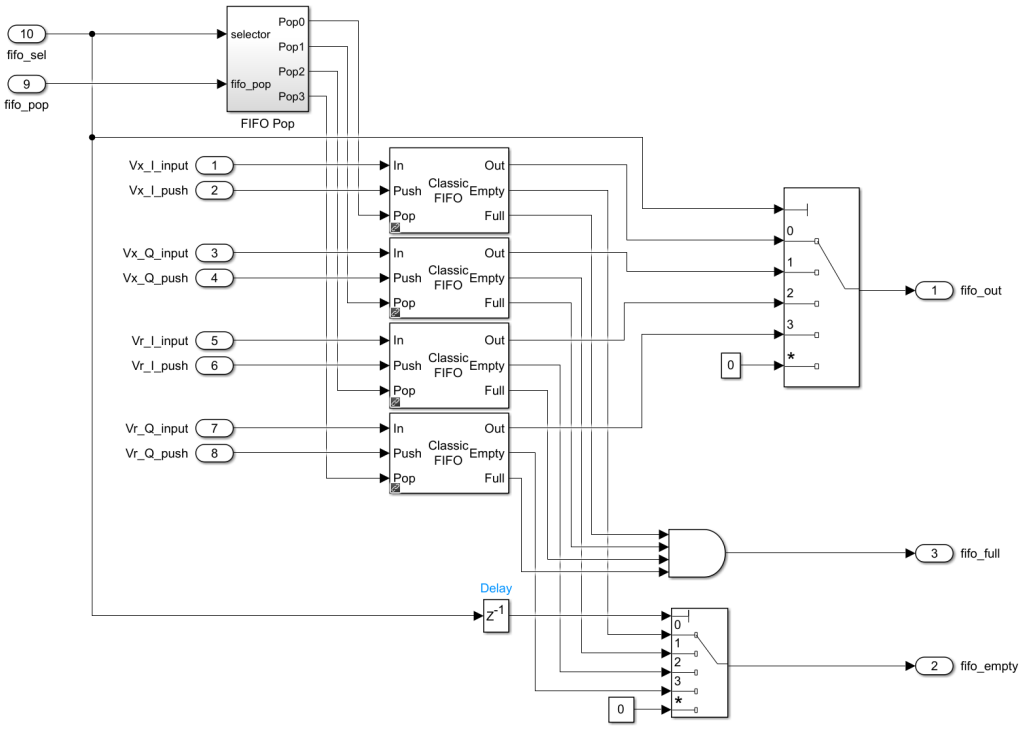

Fig. 5.17: Data handling simulink model.

5.4 Results

Figure 5.18 shows the completed Impedance Probe Testboard.

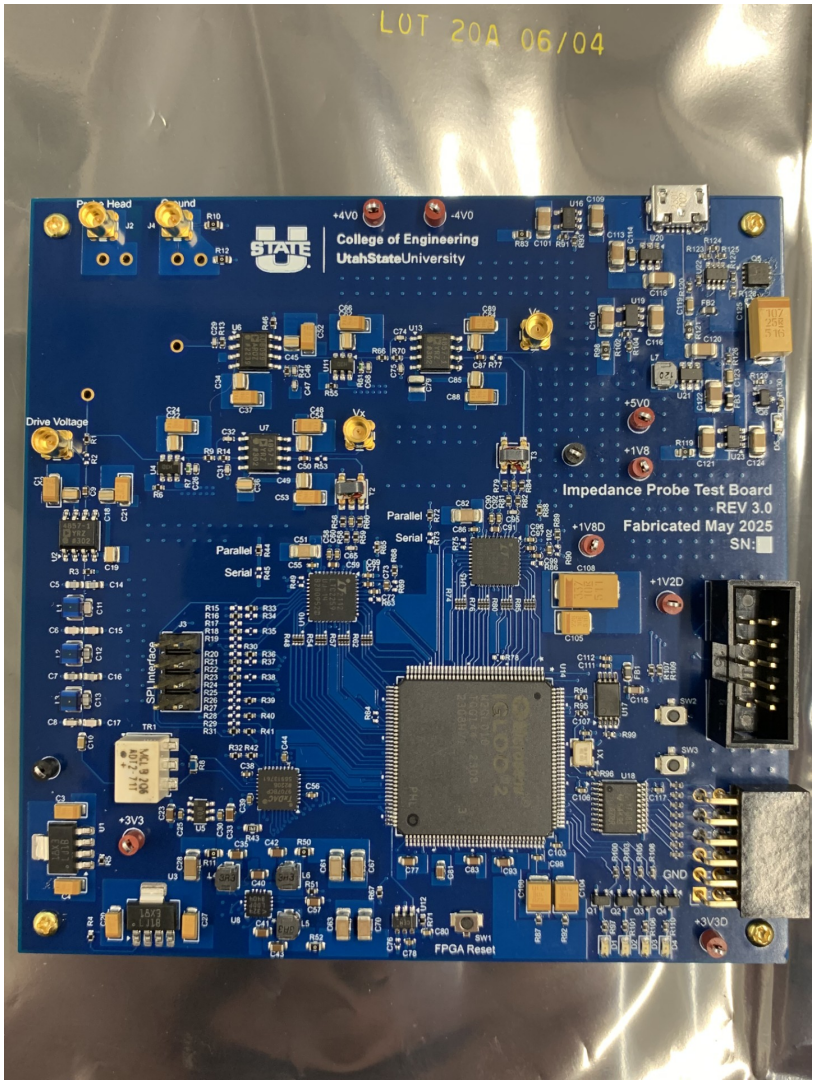

Fig. 5.18: Impedance Probe Testboard

The results below demonstrate a functional auto-balancing bridge circuit. In addition to the mixing and averaging detailed above, the individual samples from the ADC are delivered over UART for the purposed of verifying the circuit's functionality.

5.4.1 Auto-bridge Functionality

The auto-balancing bridge functionality is tested by measuring the V_x and V_r signal chains under three conditions. These are an open circuit, a short circuit, and a matched load to the drive resistance. Under these three conditions we would expect that the voltage

V_x to be at a maximum for an open circuit, a minimum for a short circuit and at half the maximum for a matched load. The V_r signal will be the complement of this, it will be a minimum for the open load, maximum for the short circuit, and half the maximum for the matched load. Figures 5.19 – 5.24 show this for frequencies of 5 and 20 MHz.

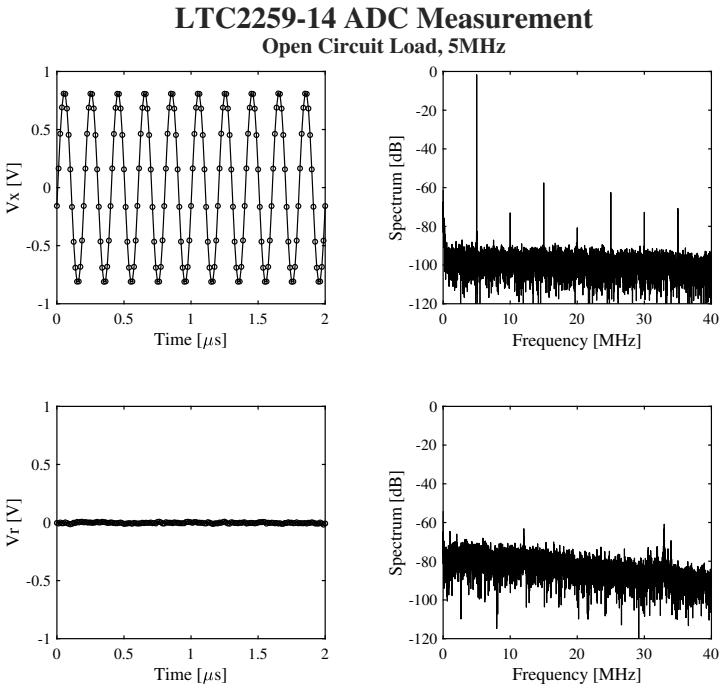

Fig. 5.19: Time domain measurement at 5 MHz with an open circuit.

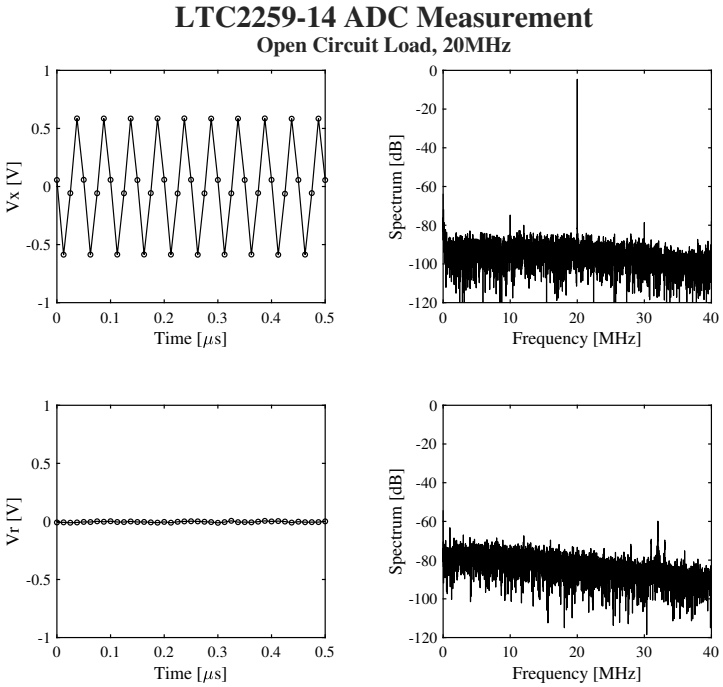

Fig. 5.20: Time domain measurement at 20 MHz with an open circuit.

From Figures 5.19 and 5.20, it is seen that while the load impedance is an open-circuit, the V_r signal is effectively 0. This is the expected behavior for the auto-balancing bridge. The quality of the V_x signal can also be seen in the spectrum plot. For the 5 MHz signal there are harmonic spurs about -60 dB down. These spurs will exist for the lower frequencies because they are within the pass band of the reconstruction filter. For 20 MHz, there are harmonic spurs that are almost -80 dB down. The harmonics that would exist and be aliased down are outside of the reconstruction filter pass-band and are eliminated.

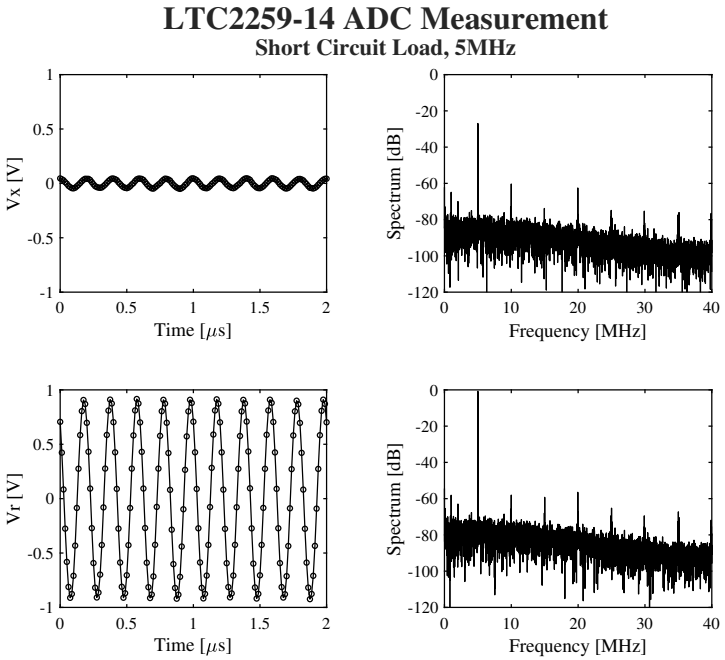

Fig. 5.21: Time domain measurement at 5 MHz with a short circuit.

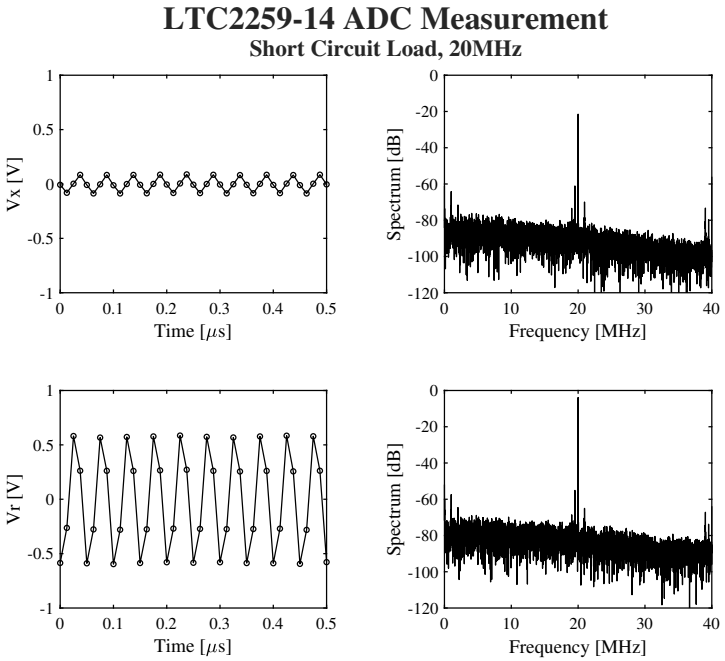

Fig. 5.22: Time domain measurement at 20 MHz with a short circuit.

From Figures 5.21 and 5.22, it is seen that while the load impedance is a short circuit, the V_x signal is close to 0, but not exactly. This is due to the open-loop gain of the op-amp. With a short-circuit load, the voltage $V_x = V_n$. So, the measured voltage here is the voltage produced by the op-amp not being able to drive it's input terminals to a virtual short.

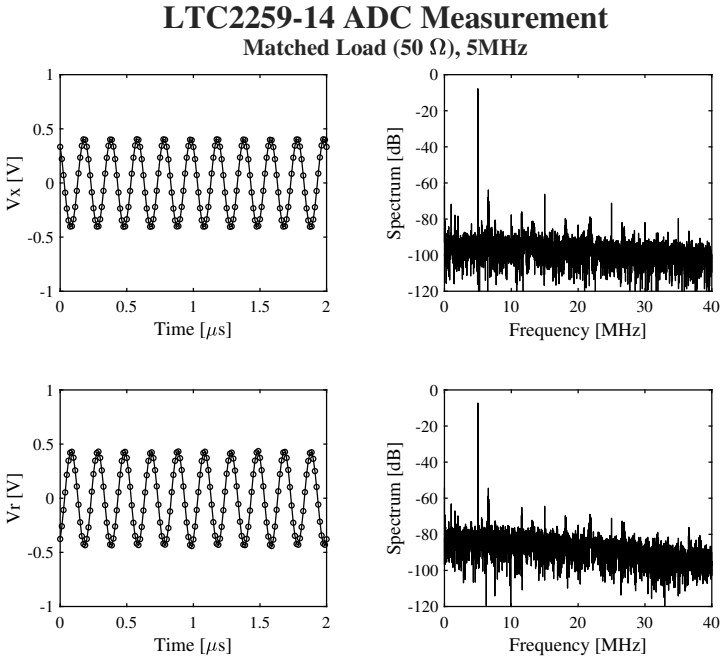

Fig. 5.23: Time domain measurement at 5 MHz with a matched load.

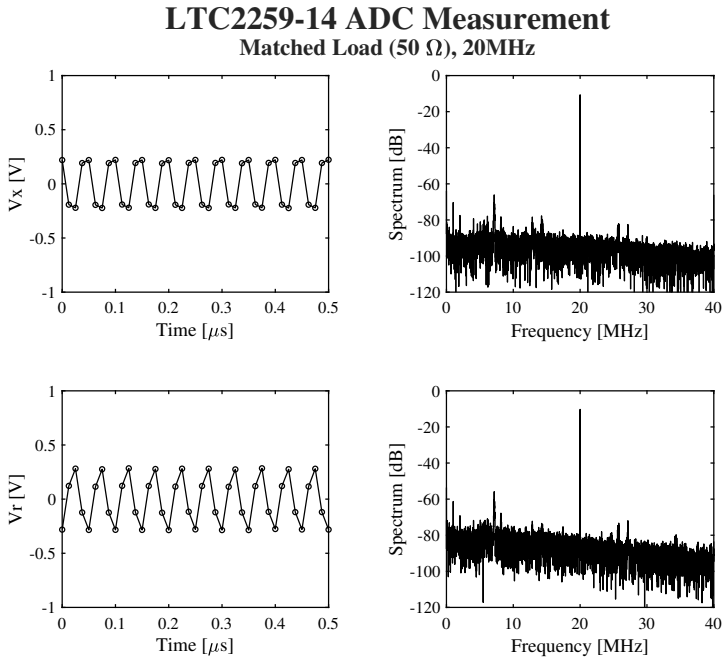

Fig. 5.24: Time domain measurement at 20 MHz with a matched load.

From Figures 5.23 and 5.24, it is seen that while the load impedance is a matched load (in this case the source and gain resistor were 50 Ω), the voltages V_x and V_r were roughly equal, which is expected for the auto-balancing bridge.

5.4.2 Calibration

To calibrate the auto-balancing bridge circuitry, it is assumed a linear mapping occurs from the actual values to the measured values in the system. In Figure 5.25, the voltage V_p and current I_p are the actual voltage and current that exists across and through the load. The voltage V_m and current I_m are the measured voltage and current across and through the load.

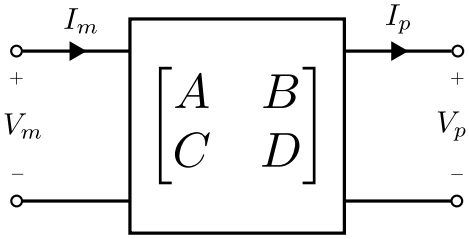

Fig. 5.25: Relationship of measured and actual voltages and currents

The relationship is then given by

$$\begin{bmatrix} V_m \\ I_m \end{bmatrix} = \begin{bmatrix} A & B \\ C & D \end{bmatrix} \begin{bmatrix} V_p \\ I_p \end{bmatrix} \tag{5.15}$$

where $A, B, C, D \in \mathbb{C}$. Using this relationship, the measured impedance is given by

$$Z_m = \frac{V_m}{I_m} = \frac{AV_p + BI_p}{CV_p + DI_p} \tag{5.16}$$

and the actual impedance

$$Z_p = \frac{V_p}{I_p} \tag{5.17}$$

By applying an open load ($I_p = 0$) short load ($V_p = 0$), quantities A/C and B/D are solved for. Then, a known load is applied to the circuit to fully solve for the actual impedance, given by

$$Z_p = \frac{(Z_{\text{load}} - Z_{\text{open}})(Z_{\text{short}} - Z_m)}{(Z_{\text{short}} - Z_{\text{load}})(Z_m - Z_{\text{open}})} Z_{\text{std}}. \tag{5.18}$$

Here, Z_{open} is the measured impedance with an open circuit, Z_{short} is the measured impedance with a short circuit, Z_{load} is the measured impedance with a calibration load, and Z_{std} is the actual impedance of the calibration load (typically measured with a high accuracy laboratory grade instrument) [19].

The calibration is performed with the calibration coupons shown in Figure 5.26 and 5.27.

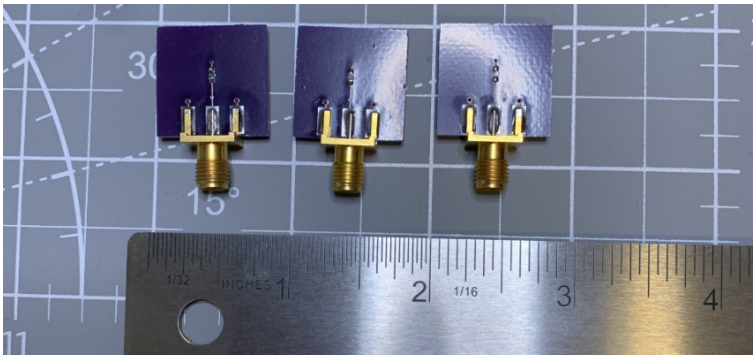

Fig. 5.26: Top side of calibration coupons.

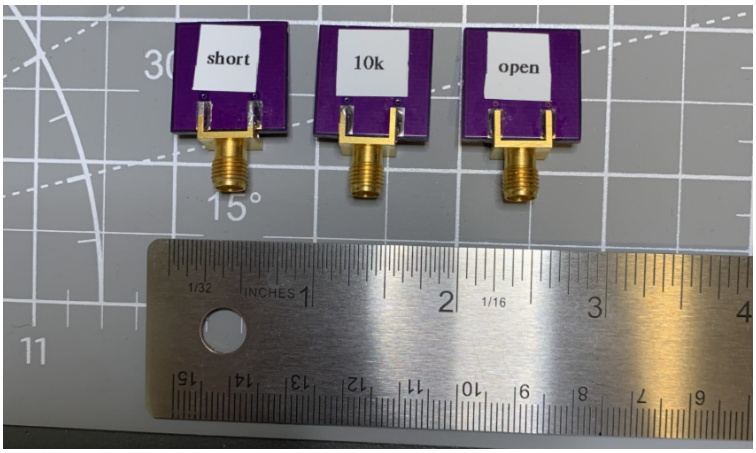

Fig. 5.27: Bottom side of calibration coupons.

Using the calibration coupons, measurements for Z_{open}, Z_{short}, and Z_{load} are taken. The last calibration coefficient needed is Z_{std}, which is the actual impedance of the 10 kΩ load resistor. For this research, the resistor was assumed to be a perfect 10 kΩ resistor with zero phase. The measured calibration coefficients are shown below in Figure 5.28.

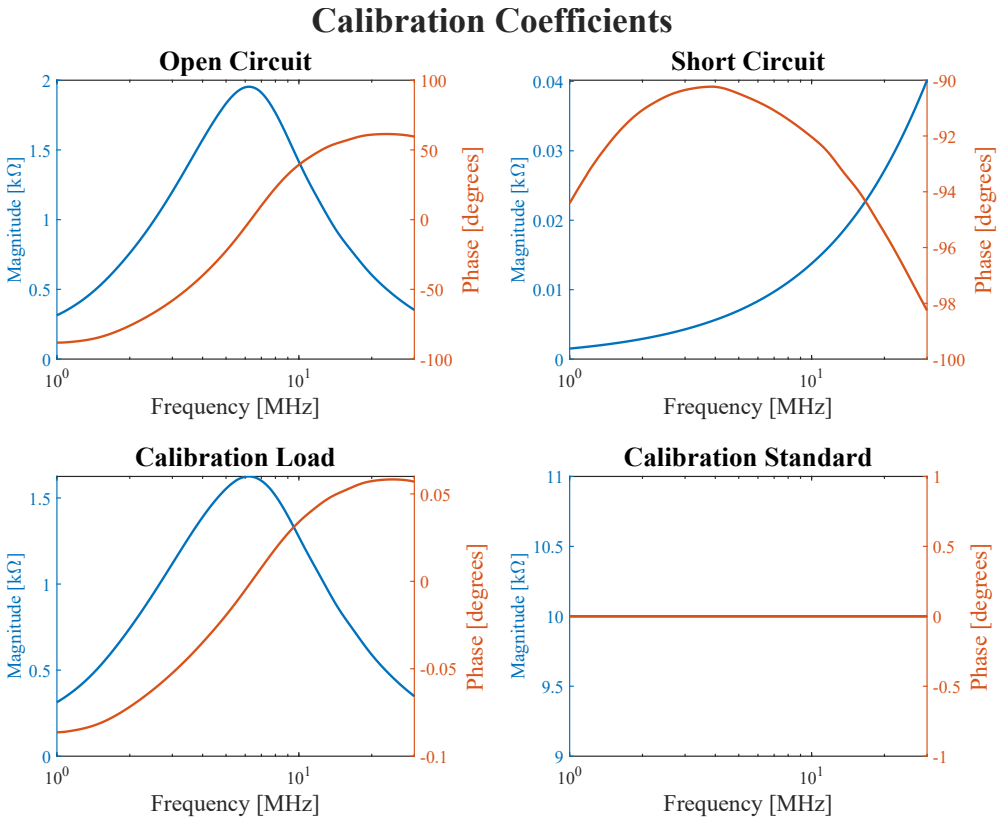

Fig. 5.28: Calibration coefficients plotted over frequency.

5.4.3 Test Loads

After calibration was performed, 100 Ω, 1 kΩ, 10 kΩ, and 100 kΩ resistors were used as test loads to measure the range of impedances that the circuit can measure. Figure 5.29 shows the result of these measured resistances.

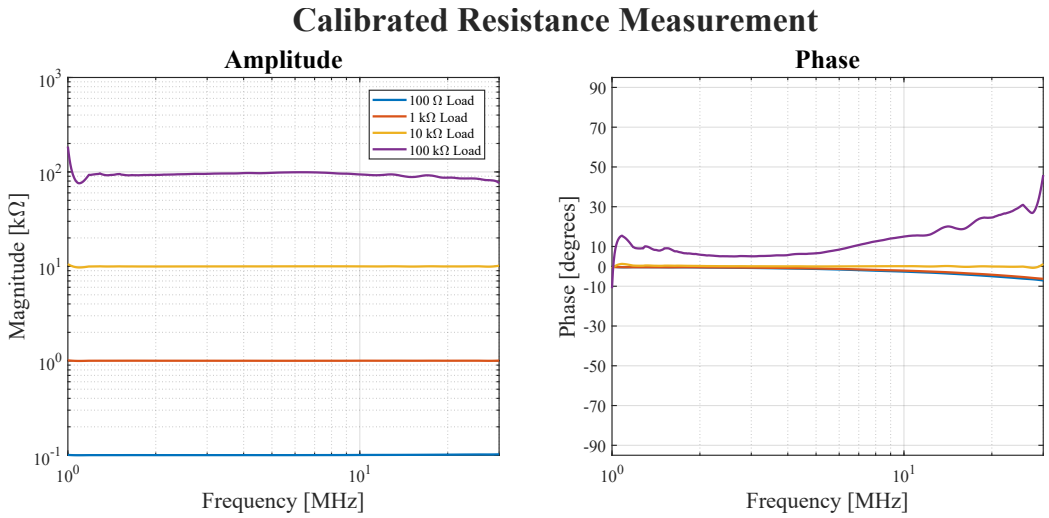

Fig. 5.29: Measured loads from 100 Ω to 100 kΩ.

As seen in Figure 5.29, the measurement for the smaller impedance is more accurate than the larger impedances. This is primarily due to the limitations with the transimpedance amplifier at these frequencies. Another contributing factor is parasitics due to the transformer that are not completely calibrated out. Another load is tested, which is a resonant load with 7.2 pF in parallel with 22 uH shown in Figure 5.30.

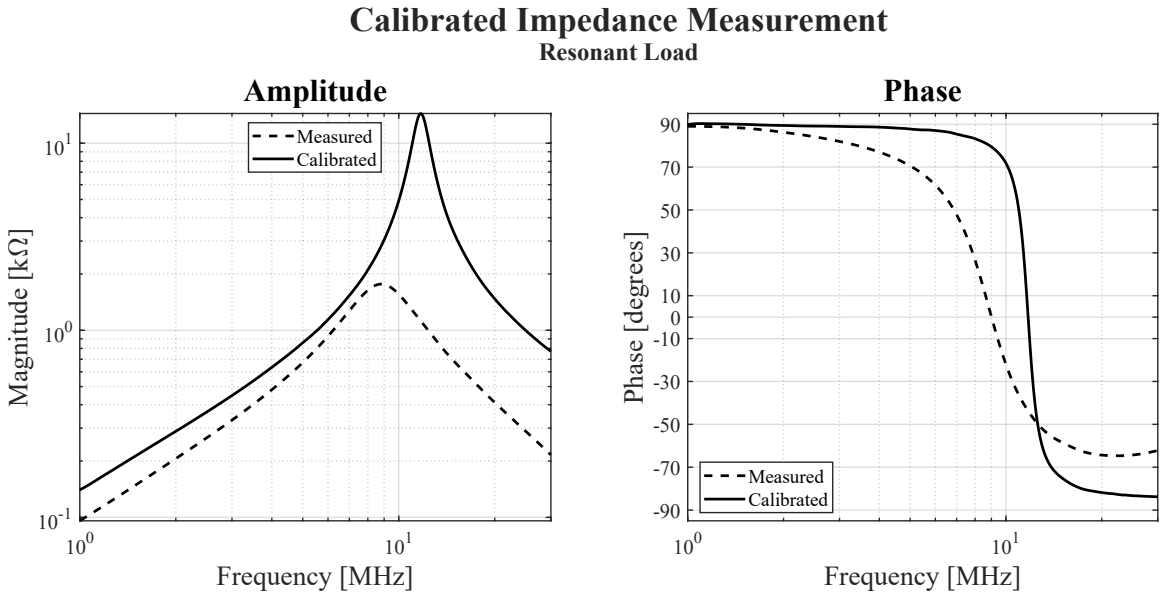

Fig. 5.30: LC resonant load measurement.

The chosen inductor has a 20% tolerance, making the resonant location anywhere from 11.5 MHz to 14.1 MHz. The circuit measured a resonant frequency of 11.7 MHz, putting it within the expected value when considering the tolerance of the inductor. The calibration applied to the circuit calibrated both the amplitude of the measured impedance as well as correctly shifted the resonance to the correct location.

5.4.4 Guarding Techniques

Figure 5.32 shows a cylindrical impedance probe suspended above a spacecraft chassis. The region directly around the spacecraft has the tightest coupling of electric field lines. These field lines are in a "disturbed" plasma environment. It is best to only take measurement from the currents that flow through the undisturbed plasma, which is located further away from the spacecraft. This process of eliminating the unwanted currents is accomplished through guarding. Guarding techniques were not implemented on the Impedance Probe Testboard, but the guarding technique implemented on the SPORT Impedance Probe will be analyzed and compared to another guarding technique.

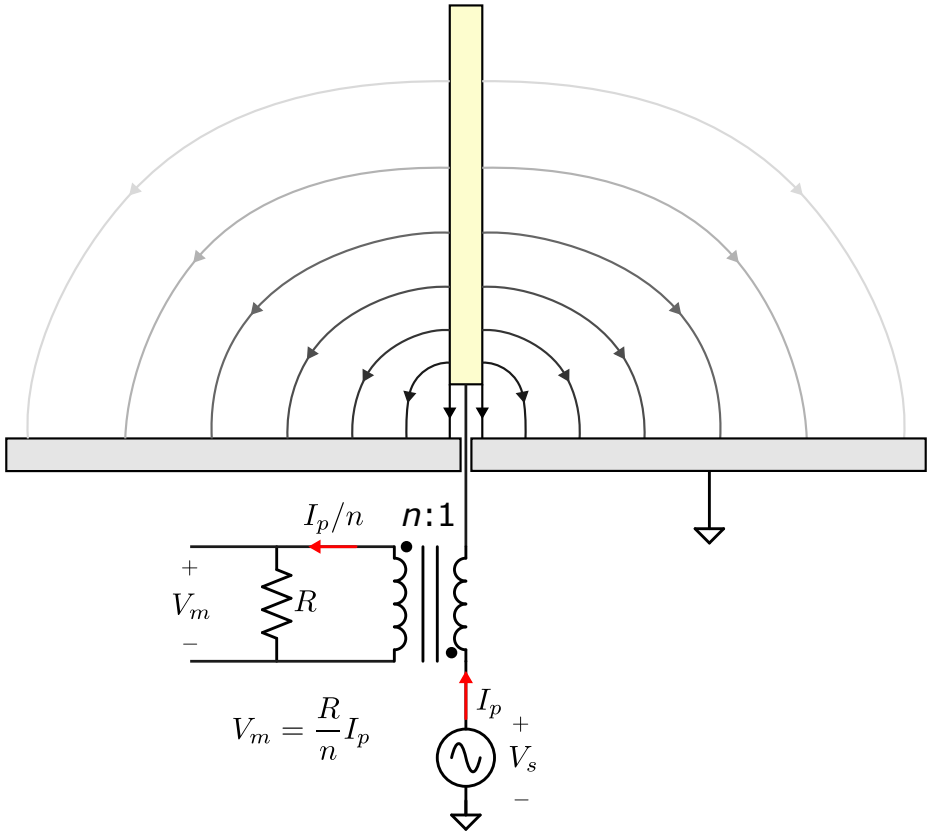

Fig. 5.31: Impedance probe above spacecraft chassis. No guarding implemented.

The currents through the undisturbed plasma and currents through the disturbed plasma can be thought of as two parallel currents between the probe head and the spacecraft chassis. These two currents are denoted as the desired current I_d and the undesired currents I_u. Ideally, if guarding is implemented perfectly, then the measured current I_m is equal to the desired current I_d meaning the undesired current is completely eliminated.

This research explores two different guarding techniques. First, is a grounded guard approach, which was used on the SPORT mission. Second is an equipotential guard, where the guard is driven to the same potential as the probe head.

5.4.5 Grounded Guard

The grounded guard setup is accomplish by connecting a conductive body beneath the probe head to ground. This additional path is wound around the current sense transformer.

This is shown in figure 5.32. The conductive body couples with the probe head, preventing the lower section of the probe from coupling to the spacecraft chassis.

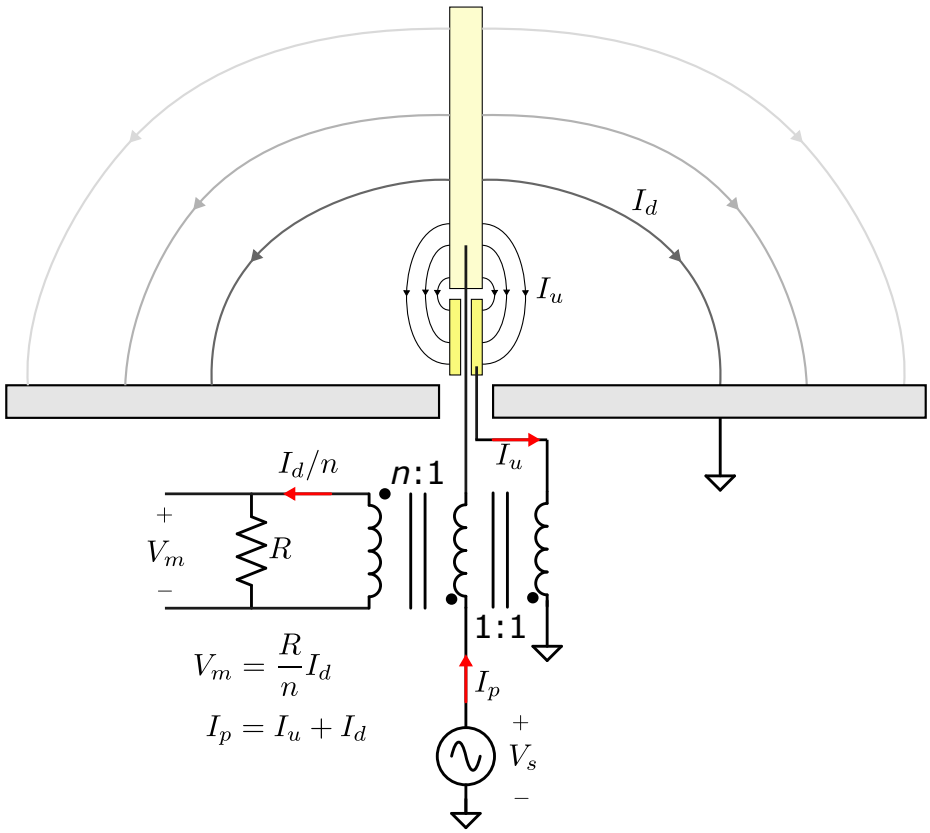

Fig. 5.32: Impedance probe above spacecraft chassis. Grounded guard implemented.

By sending the current I_u back through the transformer, the currents I_p and I_u subtract, leaving only the desired current I_d reflected to the secondary. This can be seen by looking at the general equation for the currents through an ideal transformer with j separate taps given by

$$\sum_{k=1}^{j} N_k I_k = 0. \tag{5.19}$$

Where I_k is positive or negative, depending on the direction of the current into the transformer. Given currents I_u, I_p, and I_m as the currents through the transformer windings,

the measured current is found to be

$$N_1 I_p - N_2 I_u - n I_m = 0 \quad \Longrightarrow \quad I_m = \frac{N_1 I_p - N_2 I_u}{n}, \tag{5.20}$$

with N_1, N_2, and n being the number of turns for that transformer tap. A coaxial cable is used with the inner conductor being the voltage stimulus and the outer conductor being the guard signal and a single turn around the transformer core is used, meaning $N_1 = N_2 = 1$. In addition to this, we see from figure 5.32 that $I_p = I_d + I_u$. Substituting this into 5.20, the measured current is given as

$$I_m = \frac{I_d}{n}. \tag{5.21}$$

The grounded guarding technique is simulated using capacitance values obtained from the ANSYS Maxwell simulation of the SPORT spacecraft geometries. For simplicity, $N_1 = N_2 = n = 1$ so that if guarding is implemented correctly, the expected value for I_m is equal to I_d as seen in equation 5.21.

The Maxwell capacitance matrix for the SPORT geometry was found to be (in pF)

$$Q = \begin{bmatrix} 4.75 & -1.33 & -3.42 \\ -1.33 & 2.57 & -1.24 \\ -3.42 & -1.24 & 4.66 \end{bmatrix} V \tag{5.22}$$

with $Q, V \in \mathbb{R}^3$ and Q_1, Q_2, and Q_3 are the probe, guard and spacecraft bodies respectively. Using these values, the free-space capacitance is simulated with the guard to verify the functionality of the grounded guard setup.

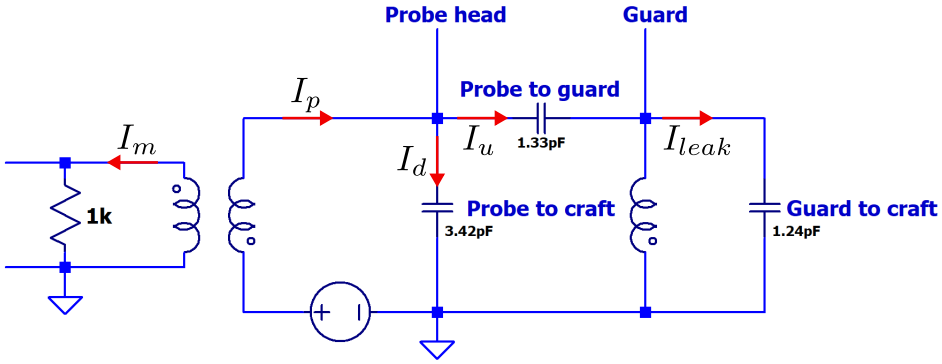

Fig. 5.33: Schematic for LTSpice simulation of the grounded guard configuration.

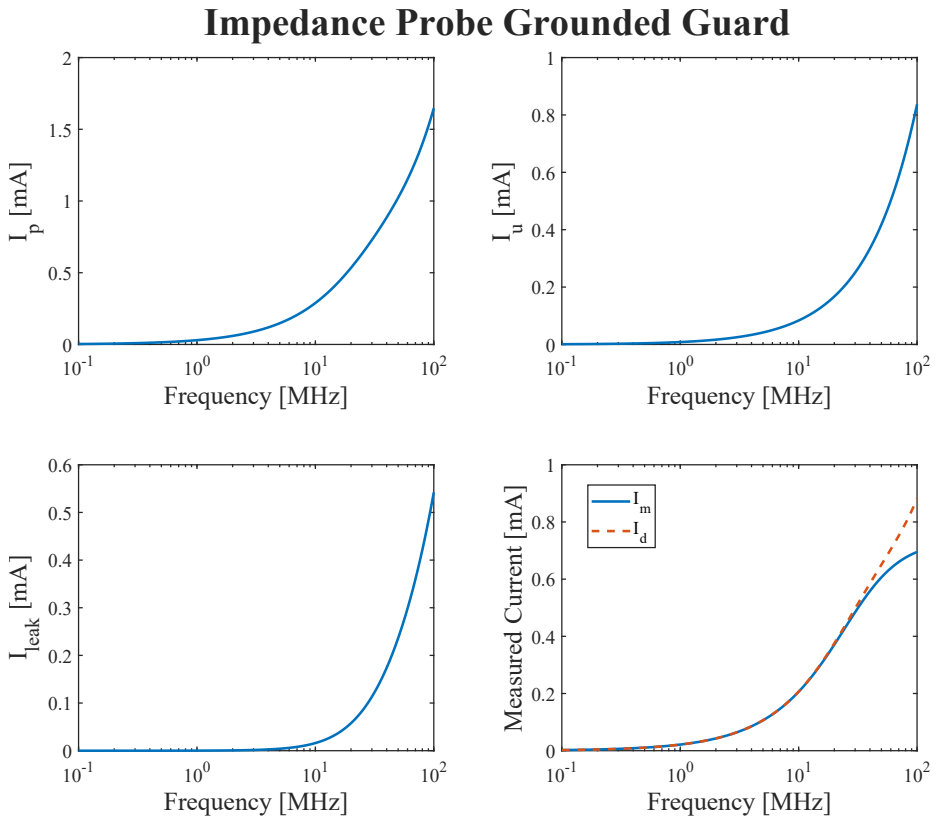

Fig. 5.34: Simulated probe currents for the grounded guard.

As seen in figure 5.34, the current I_m is not equal to I_d over all frequencies. The reason for this is that there is an AC potential developed over the transformer winding connecting the guard to ground. Because of this AC potential, there are leakage currents through the guard to craft capacitance. An impedance probe like the one on SPORT is driven to frequencies between 2-30 MHz. At these frequencies, the leakage current is minimal; however, there should be effort to reduce the capacitance between the guard conductor and the spacecraft chassis to minimize these leakage currents. In addition, this simulation was done with a turns ratio of 1:1:1 for simplicity. Using a higher turns ratio such as 10:1:1 would reduce the burden resistance of 1 kΩ to 10 Ω, further reducing the AC potential across the transformer winding and minimizing leakage currents.

5.4.6 Equipotential Guard

The equipotential guard setup is accomplish by driving a conductive body beneath the probe head to the same potential as the probe head as shown in figure 5.35. The conductive body effectively extends the field lines of the monopole, however the currents from the guard are not driven by the stimulus source. Instead, these currents are driven by a buffer circuit, thus the currents induced from the guard are not reflected to the transformer secondary.

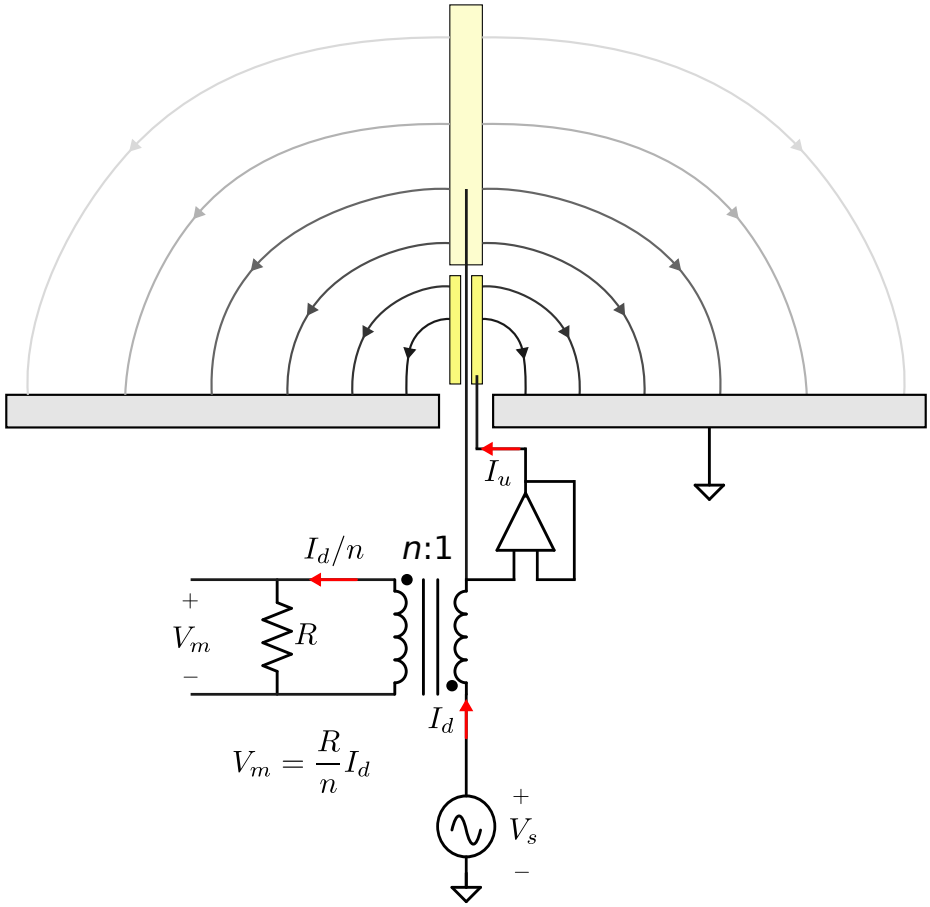

Fig. 5.35: Impedance probe above spacecraft chassis. Equipotential guard implemented.

The equipotential guarding technique is simulated using capacitance values obtained from the ANSYS Maxwell simulation of the SPORT spacecraft geometries. For simplicity, $N_1 = N_2 = n = 1$ so that if guarding is implemented correctly, the expected value for I_m is equal to I_d as seen in equation 5.21. For this simulation, a near ideal op-amp is used.

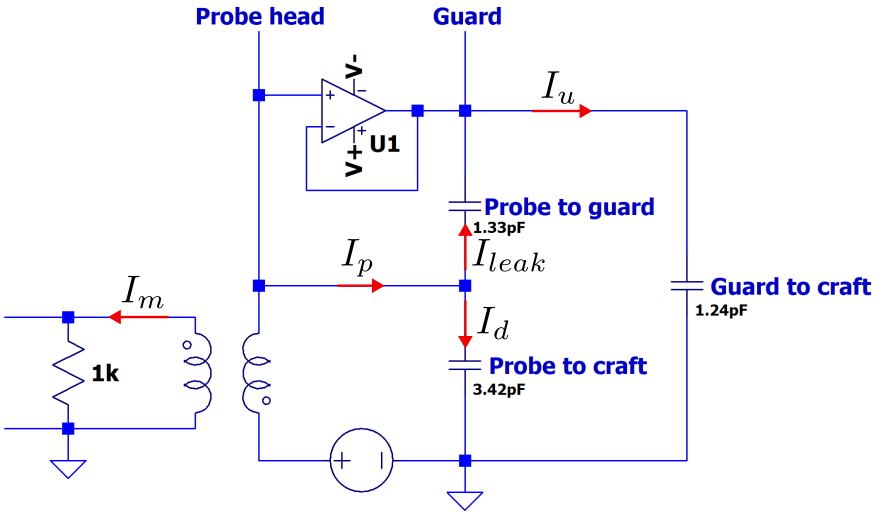

Fig. 5.36: Schematic for LTSpice simulation of the equipotential guard.

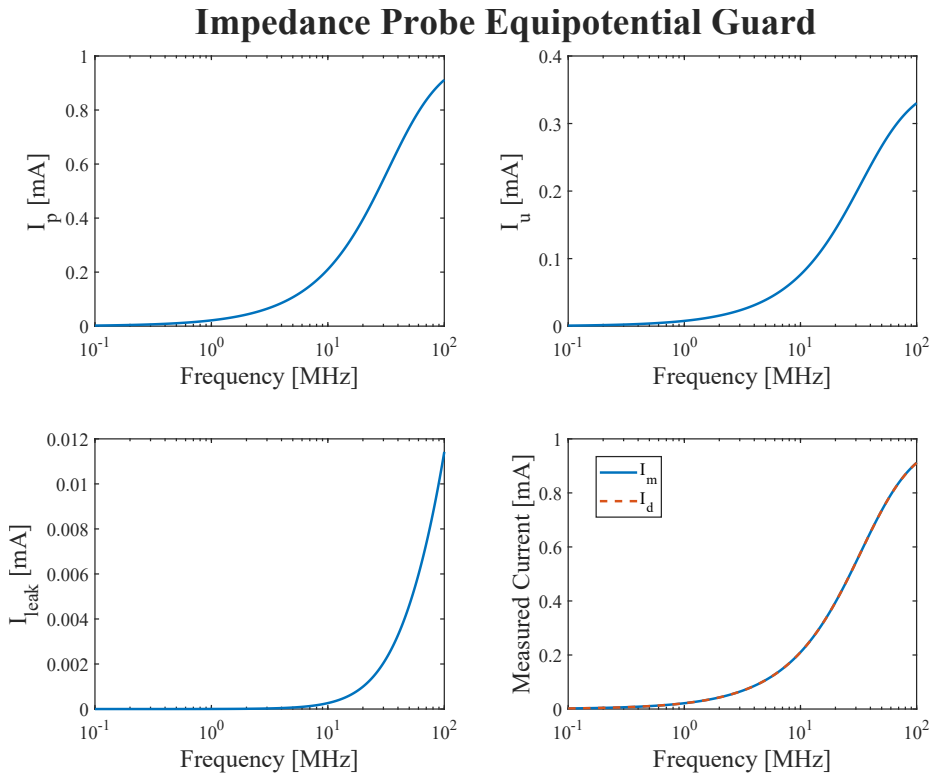

Fig. 5.37: Simulated probe currents for the equipotential guard.

Shown in Figure 5.37, the leakage currents are effectively zero and the measured current is equal to the desired currents for all frequencies. This is using a near-ideal op-amp. If there is a phase shift between the probe voltage and the guard voltage, an error in the measurement is created due to currents that leak from the probe to the guard through the capacitance. There are minor phase shifts induced by cable length mismatch between the probe head and guard, but these are minor. The time delay induced is given by

$$T_d = \frac{\Delta\ell}{v_p}. \tag{5.23}$$

Where $\Delta\ell$ is the mismatch in length between the probe head and the guard. For a coaxial cable where Perfluoroalkoxy (PFA) material is used (such as Alpha Wire), which has a dielectric constant $\epsilon_r = 2.2$, the phase mismatch is calculated as

$$\Delta\phi = 2\pi f \frac{\Delta\ell\sqrt{\epsilon_r}}{c}. \tag{5.24}$$

Then for a length mismatch of 100 mm, the phase error is less than 0.1° for frequencies less than 30 MHz, which means the phase error will be dominated by the choice of op-amp used as the buffer. Choosing an op-amp buffer with a large Gain Bandwidth Product (GBP) will minimize the error.

5.4.7 Guard Comparison

Both guarding techniques accomplish the goal of measuring only the currents through the undisturbed plasma. However both techniques have their advantages and disadvantages.

The equipotential guard has the advantage of electric field shaping. For a cylindrical probe, like the one on SPORT, a large portion of the probe surface is away from the spacecraft and in the relatively undisturbed plasma environment. However, some spacecraft would prefer to have a patch probe mounted to the spacecraft chassis. In the grounded probe approach, there would be minimal fields that leave the region near the spacecraft surface. With the equipoential guard technique, the guard acts as a way to force the electric fields

to extend up before closing on the spacecraft chassis.

The disadvantage of the equipotential guard is the phase induced by the op-amp used to buffer the signal as well as the extra power draw required from the op-amp. A poor choice of op-amp could induce phase shifts of up to tens of degrees, if not more, causing large leakage currents from the probe head to the guard conductor, creating large measurement error. The grounded guard technique has the advantage of consuming less power. However, there is additional complexity in the transformer design.

5.5 Summary

This chapter presented the design, implementation, and testing of a custom impedance probe circuit based on the auto-balancing bridge topology. The circuit was developed to improve the accuracy of impedance measurements across the wide range of plasma conditions expected during spacecraft operation.

The chapter began by reviewing the auto-balancing bridge and analyzing its sensitivity as a function of the source resistor and measurement impedance. This analysis a good initial choice for selecting the gain resistor to maximize average sensitivity across a specified impedance range.

A complete testboard was then designed to demonstrate the bridge operation from 1–30 MHz. The system includes a voltage stimulus source, a reconstruction filter, a hand-wound transformer for galvanic isolation and impedance scaling, sense circuitry for the voltage signals, and an FPGA for mixing, averaging, and data handling.

Simulation and measurement results verified operation of the auto-balancing bridge. Time-domain and spectral measurements confirmed the expected complementary behavior of the V_x and V_r voltages for open, short, and matched loads. Calibration using known standards enabled accurate measurement of impedances from 100 Ω to 100 kΩ, and the system measured a resonant LC load.

Finally, two guarding techniques were analyzed and compared. Simulations showed that the grounded guard reduces undesired currents but introduces leakage due to AC

potential on the transformer winding, while the equipotential guard eliminates leakage at the cost of power consumption.

CHAPTER 6

Conclusion

6.1 Contributions

6.1.1 Numerical Modeling of Capacitive Impedance Probe Theory

A major component of this thesis was the development of a numerical method based on the Maxwell capacitance matrix and finite-element electric-field solutions.

By rotating the cold-plasma permittivity tensor into arbitrary magnetic field directions and numerically integrating the resulting displacement field flux, the method allows computation of impedance for any probe or spacecraft geometry. Validation against analytical solutions for simple geometries such as plates, cylinders, and spheres demonstrated excellent agreement, confirming the accuracy of the approach.

Applying the method to the SPORT spacecraft geometry revealed how real probe configurations deviate from simple geometries. This capability is critical for the design of future missions, where probe geometry strongly influences the measured impedance.

6.1.2 Sheath Analysis and Resonance Behavior

By modeling the sheath as a vacuum layer in series with the plasma capacitance, the analysis showed that a distinct series resonances emerges in addition to the traditional parallel resonance. Deriving rational impedance expressions made it possible to identify how the resonance locations shift with plasma frequency, magnetic field angle, sheath thickness, and probe geometry. Comparison with SPORT sweep data revealed strong alignment between the sheath model and measurement.

6.1.3 Impedance Probe Circuit Development

This thesis utilized an auto-balancing bridge topology to design and build a new

impedance probe board. This board demonstrated the capability of measuring a wide range of impedances, even with the limitations of the trans-impedance amplifier. While the measurement of higher impedances had some measurement error, these errors are expected to be minimized after further development.

Guarding techniques were explored and shows the importance of minimizing the leakage paths that exist in the system. Both a guarded and equipotential guarding technique were analyzed. It was found that both techniques work to eliminate unwanted current paths. The grounded guard technique introduces complexity in the transformer design, while the equipotential guard technique introduces complexity in the op-amp selection to minimize phase induced error.

6.2 Future Work

6.2.1 Warm Plasma Dielectric

The cold-magnetized dielectric model used in this research has the limitation that it does not account for collisionless damping. An area of future work would be to take the numerical methods presented in this research and incorporate the warm plasma permittivity tensor. Doing so would require a spatial Fourier transform of the spacecraft model.

6.2.2 Gradient Sheath Model

For the sheath model presented in this research, a discrete boundary condition where the sheath was treated as a vacuum was used. In reality, the sheath is a complex, non-linear structure. Future work should incorporate a nonuniform sheath derived from solutions to the nonlinear equations, including wake effects and a lossy dielectric response.

6.2.3 Auto-balancing Bridge Improvements

The circuit demonstrated in this thesis was functional, but the performance can be improved by implementing a digital controller to generate the V_r voltage. The trans-impedance amplifiers open-loop gain limitations just limit the possibilities of sensing an

ultra-wide range of impedances. A limitation in the digital controller method is the power consumption required. The V_n signal needs to be sampled and mixed into I and Q parts and two controllers are run in parallel to generate the V_r signal. This V_r signal then needs to be driven back out of the FPGA through another DAC, requiring more power than the trans-impedance method shown in this research.

REFERENCES

[1] J. Wellington, C. Swenson, B. Lewis, and T. S. Team, "Analysis of the sport impedance probe data and theory," in *AGU Fall Meeting 2023*. San Francisco, CA, USA: American Geophysical Union, December 2023, poster Presentation, Utah State University, Center for Space Engineering. [Online]. Available: https://agu.confex.com/agu/fm23/meetingapp.cgi/Paper/1511027

[2] E. F. Pound, "Techniques to improve electron density measurements in the d region of the ionosphere," Ph.D. Dissertation, Utah State University, Logan, Utah, USA, 1995, print copy only; no digital version available in public archives as of 2025.

[3] W. Sanderson, "The history and dynamics of the plasma impedance probe," Master's thesis, Utah State University, Logan, Utah, USA, 2007, cited in later PIP literature; no public PDF located.

[4] J. Martin-Hidalgo, "Sequential quadrature measurements for plasma diagnostics," Master's thesis, Utah State University, Logan, Utah, USA, May 2014, all Graduate Theses and Dissertations, 2297. [Online]. Available: https://digitalcommons.usu.edu/etd/2297

[5] C. W. Young, "Design of a sweeping impedance probe for the SPORT mission," Master's thesis, Utah State University, Logan, Utah, USA, Aug. 2020, all Graduate Theses and Dissertations, 7884. [Online]. Available: https://digitalcommons.usu.edu/etd/7884

[6] N. P. Tipton, "Design of miniaturized sweeping langmuir probe and electric field probe for the sport mission," Master's thesis, Utah State University, Logan, Utah, USA, May 2021, uSU Space Weather Probes (SWP) instrument suite development. [Online]. Available: https://digitalcommons.usu.edu/etd/8072

[7] N. L. Wallace, "Developing firmware for space weather probes 2 using HDL coder," Master's thesis, Utah State University, Logan, Utah, USA, Aug. 2023, all Graduate Theses and Dissertations, 8800. [Online]. Available: https://digitalcommons.usu.edu/etd/8800

[8] B. J. Lewis, "Development of the digital signal processing for the space weather probes version 2 sensor using the MATLAB/Simulink environment," Master's thesis, Utah State University, Logan, Utah, USA, Aug. 2023, all Graduate Theses and Dissertations, 8872. [Online]. Available: https://digitalcommons.usu.edu/etd/8872

[9] K. G. Balmain, "The impedance of a short dipole antenna in a magnetoplasma," *IEEE Transactions on Antennas and Propagation*, vol. 12, no. 5, pp. 605–617, 1964, manuscript received November 26, 1963; revised March 30, 1964. Supported by the Geophysics Research Directorate, Air Force Cambridge Research Laboratories, under Contract No. AF 19(604)-5565, and by NASA under Contract No. NsG-395.

[10] R. H. Bishop and K. D. Baker, "Electron temperature and density determination from rf impedance probe measurements in the lower ionosphere," *Planetary and Space Science*, vol. 20, no. 6, pp. 997–1013, 1972, received in final form 17 January 1972. Printed in Northern Ireland.

[11] Y. S. Diant, "Deriving improved plasma fluid equations from collisional kinetic theory," *Frontiers in Physics*, 2024, arXiv preprint arXiv:2407.13860. [Online]. Available: https://arxiv.org/abs/2407.13860

[12] J. W. Brooks and M. C. Paliwoda, "Uncertainty analysis of the plasma impedance probe," *arXiv preprint arXiv:2402.10304*, 2024, u.S. Naval Research Laboratory, Washington, D.C., USA. Dated 19 February 2024. [Online]. Available: https://arxiv.org/abs/2402.10304

[13] T. E. S. Jr. and J. A. Goree, "Analytic expression for the electric potential in the plasma sheath," *IEEE Transactions on Plasma Science*, vol. 17, no. 6, pp. 884–889, December 1989.

[14] D. Hall, "Make accurate impedance measurements using a vna," *Microwave & RF Magazine*, pp. 1–3, March 2019, available online at Microwave & RF (mwrf.com). [Online]. Available: https://www.mwrf.com

[15] *Keysight E5061B-3L3/3L4/3L5 LF-RF Network Analyzer with Option 005 Impedance Analysis Function*, Keysight Technologies, Santa Rosa, CA, USA, 2020, keysight Technologies, Data Sheet. Unlocking Measurement Insights. [Online]. Available: https://www.keysight.com

[16] *Agilent PN 4294A: New Technologies for Accurate Impedance Measurement (40 Hz to 110 MHz)*, Agilent Technologies, Santa Clara, CA, USA, 2000, agilent Technologies Product Note PN 4294A. [Online]. Available: https://www.keysight.com

[17] *8 Hints for Successful Impedance Measurements*, Hewlett-Packard Company, Palo Alto, CA, USA, 1997, hewlett-Packard Application Note 346-4. [Online]. Available: https://www.keysight.com

[18] E. D. Lorenzo, "The maxwell capacitance matrix," FastFieldSolvers S.R.L., White Paper WP110301, June 2020, copyright 2020, FastFieldSolvers S.R.L. All Rights Reserved. [Online]. Available: https://www.fastfieldsolvers.com

[19] *Impedance Measurement Handbook: A Guide to Measurement Technology and Techniques*, 6th ed., Keysight Technologies, Santa Rosa, CA, USA, 2020, application Note, Keysight Technologies. [Online]. Available: https://www.keysight.com